POLITECNICO DI TORINO

Master of Science in Mechanical Engineering - Master Thesis

Mechanical effects of the plasma surface treatment on carbon fabrics used in composite materials

Politecnico di Torino

PLASMA NANO-TECH
EnviPark - Trattamenti con nanotecnologie al plasma

ENVIRONMENT PARK
Parco Scientifico Tecnologico per l'Ambiente

Academic Supervisors:

Prof. Davide Salvatore Paolino
Ing. Raffaele Ciardiello

Company Supervisor:

Ph.D. Domenico D'Angelo

Candidate:

Samuele Sampino

October 2022

Table of Contents

Abstract

The benefit obtained from plasma treatment of carbon fiber fabrics in terms of increasing the adhesive properties with a 30% bio-based epoxy resin is investigated in this study. The fabric samples were treated using the *Atmospheric Pressure Plasma Jet* by adopting two different sources of gas, nitrogen and *N2H2* hydrogen-nitrogen mixture, varying the primary and secondary process parameters in order to find the optimal configuration. An initial confirmation regarding the efficiency of the treatment and the correct choice of parameters was obtained primarily by surface chemical-optical characterization with *Micro-Raman* spectroscopy and *Attenuated Total Reflection* (*ATR*) analysis. The effective ablative and/or chemical mixing action of the species on the surface were identified through the use of the latter methods considering the presence of new grafted functional groups - amino, hydroxyl and carboxylic based - on a naturally non-polar surface of carbon fiber fabrics. After chemical characterization, pre-cracked samples were made with untreated and treated fabrics by using vacuum infusion as manufacturing method. Finally, to evaluate the effectiveness of the treatment in terms of mechanical resistance and delamination characteristics, the *Double Cantilever Beam* test and the *End Notched Flexural* test were carried out. In particular, both procedures were performed according to the *ASTM D5528* and *ASTM D7905* standards for the evaluation of the fracture toughness G_C on Mode I and Mode II with the adoption of *Digital Image Correlation* (*DIC*) instrumentation and equipment to facilitate the analysis of crack propagation.

List of figures

List of tables

1. Introduction

In recent years, composite materials have been adopted in the automotive industry to achieve promising results in terms of fuel consumption and environmental pollution's reduction. The research is moving towards the use of lightweight materials that could have comparable or greater mechanical properties with respect seasoned adopted materials.

Carbon fiber reinforcement composite plastic (*CFRP*) exhibits the aforementioned characteristics showing a lower density (1.75~2.2 g/cm^2) nearly a factor of four than steel, and much higher strength.

The first commercial appearance of carbon fiber dates back to 1958 by R. Bacon et al. [1] using rayon as cellulosic precursor which has no more commercial importance today. It was surprising considering the unusually high tensile strength and conductivity of the graphite filaments. The mechanical properties are mainly governed by origin from which it is derived, strictly related to the precursor chosen, in particular polyacrylonitrile (*PAN*) based carbon fibers have good tensile strength (2~7 GPa) and modulus (200~900 GPa) properties, whereas pitch-based carbon fibers show higher modulus, albeit a lower strength [2].

To obtain required performance of the composites, precursors of carbon fiber should contain high amount of carbon (at least 92 wt%), molecular chain with good extension characteristics to make high molecular weight and high degree of orientation of crystal plane along the fiber axis, with parallel arrangement of crystals that makes fibers amazingly stronger with respect the other synthetic fibers. The crystal plane structure, formed by cross-linking of conjugated aromatic rings, is essential in describing how different planes of atoms will interact with each other and affect their chemical and mechanical properties.

The two main sectors of carbon fiber applications are nuclear and aerospace engineering, and the general engineering-transportation sector, in which the majority of the engineering components production is related to bearings, gears, cams, fan blades and further automobile items.

For the automotive field, CFRP composites usage covers not only the sphere of the exteriors but also of the chassis and the interiors. For example, Koninklijke DSM N.V. (usually named *DMS*) has developed and used Sheet Moulding Compound (*SMC*) carbon fiber components for

low weight structural and semi structural components which have reached a lower weight of 55% compared to those in traditional SMC. [2]

Although carbon fibers reveal the aforementioned properties, when adopted as reinforcement in composite structures without any prior surface treatment, they can present low interlaminar shear strength (*ILSS*).

This has been ascribed to weak adhesion and poor bonding between fiber and matrix, that are the two components which usually present different physical and chemical characteristics. In high performance composites, the lack in proper interfacial interactions may result in a final catastrophic failure. Especially in carbon fiber reinforced plastics, where the carbon fiber surface is inert resulting in a difficulty adhesion.

The inertness of the surface is due to the fabrication process of carbon fiber from its precursor: the high temperature graphitization process causes a change in the surface morphology with a resulting lack of functional groups on the surface as well as the excessive smoothness and less adsorption characteristics of carbon fibers [3].

Fiber/matrix adhesion efficacy depends upon simultaneous action of different parameters that lead to increase in physical adsorption, chemical interaction (i.e.: covalent bonding) but also mechanical interlocking that is the resin capacity of penetrate any pores and irregularities of fibers.

In consideration of these characteristics combined with the problem of low polarity, different solutions are used to increase its surface free energy and adhesion to the matrix, including wet chemical methods and dry surface treatments. Surface free energy is the solid surface tension, peculiar property of solid-fluid interface interaction.

The “wet” methods concern surface activation by means of polymer sizing, application of substance to act as protective coating or filler, and chemical and electrochemical modification through component immersion in acid solution as nitric acid or hydrochloric acid. This allows to trigger a proper oxidation process that enhances surface properties and their effectiveness depending on the process calibration in terms of concentration of oxidative medium, temperature and treatment time [4].

Wu et al. [5] used nitric acid bath at 115°C for 20-90 minutes immersion of carbon fibers to achieve a suitable oxidation. The tensile strengths initially increased and after a time between 20 minutes and 1.5 hours, it reaches a plateau, then decreased with an increase in oxidation time revealing pitting and excessive fragmentation of fiber surface. Barbier et al. [6] successfully improved the toughness of carbon fiber/epoxy composites through grafting of ethylene diamine, alternative to electrochemical oxidation in aqueous solution of the fibers surface; continuous succession of covalent bonds from the carbon fibers to the epoxy resin was established and used as key point process for the further electrochemical oxidation of ethylene diamine.

Contrariwise, the "dry" methods include thermal treatments, plasma treatments, high-energy or UV irradiation. These methods are the answer to the need for more clean and environmentally friendly alternatives to chemical pre-treatments.

Plasma treatment has been reported as one of the most effective surface treatment techniques ascribed to its ability in treating the surface retaining the bulk properties of the material, and due to its long-term durability. [7]

Among various types of plasma treatment, the Atmospheric Pressure Plasma Jet (*APPJ*) is commonly used in industrial applications for plastic, polymeric and fiber reinforced composite surface treatment. This technique fits better the requests of high amount of components to be treated in-line and the optimal work programming is obtained by calibrating the process parameters, primary and secondary, which are best suited to the type of material to be treated.

Plasma, the so called fourth state of the matter, is an ionized gas and electrically conducting medium consisting of negatively, positively and neutral chemical species.

In the cold plasma state several reactions can occur such as ionization, excitation, dissociation and recombination, because of the collision of electrons and other species in the plasma medium. As consequence, the solid material that is under the plasma jet action, takes part of a highly efficient energy exchange. [8]

The choice of the process gas is fundamental for the outcome of the treatment and the effect to be obtained on the treated component since the gas influences the creation of the ions mixture, functional groups and radicals. Their influence differs depending on the component treated, offering improvements in adhesion or an increase in hydrophilic characteristics.

Plasma treatments can increase the molecular ratio between oxygen and carbon content as a consequence of the oxidation process. Choosing nitrogen or nitrogen based mixture, the treated fibers successfully count for the presence of polar functional groups: ether, carboxyl, carbonyl, hydroxyl groups.

Tiwari et al. [9], used cold remote plasma treatment on twill weave 2x2 carbon fiber fabric samples, with a N_2 and N_2-O_2 gas mixture. As result, polar functional groups were found, responsible for improvement in adhesion between matrix and fabric. The composite made by treated fabric and *PEI/PEEK/PES* polymeric matrices, showed relative gain in elastic modulus, flexural strength and ILSS at the cost of tensile strength, of a minimum extent.

High-energy particles in plasma gas, such as O+ and O•, react with the groups on the carbon fiber surfaces, such as -C-O- and -C=O. N_2 plasma could effectively introduce nitrogen-containing groups (i.e., -NH_x) onto carbon fiber surfaces through the breaking of C=C bonds creating N groups bonded to the carbon fiber benzene rings, positive and wanted effect when the final composite counts of epoxy resin as matrix. Oxygen molecules can dissociate thanks to the impact of vibrationally excited N2 molecules thus helping to generate more reactive oxygen radicals. The reaction that takes place is $N_2 + O_2 \rightarrow 2O + e$, and the same happens with the impact of electrons (reaction $e + O_2 \rightarrow 2O + e$). [10] [11]

Treatment time and working distance between the nozzle of the APPJ and the sample to be treated, are the two main important secondary parameters. Both the effects of the primary (i.e.: treatment gas, excitation frequency etc.) and secondary parameters are evaluable by means of suitable chemical characterizations:

- contact angle measurement is used as indication of the changing in surface wettability;
- optical emission spectroscopy (*OES*) gives information about atomic and molecular species prevailing in the glow space of chosen plasma's gas;
- X-ray photoelectron spectroscopy (*XPS*) is used for the functional groups on the surface analysis, as well as the application of the Attenuated Total Reflection (*ATR*) and Raman spectroscopy;
- emission scanning electron microscopy (*SEM*) permits to examine the change in samples' morphology.

Ceregatti et al. [10] used all the methods listed before to asses the effectiveness of the treatment. In particular, the untreated carbon fiber fabric exhibited a high contact angle with deionized water (132°), which is characteristic of hydrophobic surfaces. After the N_2-H_2 plasma functionalization, the wettability dramatically increased and the most significant changes were related to the longer radio frequency (*RF*) plasma treatment. As lastly explained, a longer treatment and plasma exposure yields a large number of radical species on the fiber surface, which can promote the C-C bonds scission and the introduction of the functional groups that were present in the plasma phase. The contact angle dropped to nearly 60° and then rapidly increased but with a progression that slowed down after 1 week, stabilizing at approximately 120°. This underlines the importance of making rapidly the correct composite fabrication process once the surface treatment is done in order to avoid any loss in treatment effectiveness.

OES of the plasma showed an abundance of N_2* and NH reactive species but a longer carbon fiber exposure to the plasma reduced the N content, causing the desorption of nitrogen functional groups. Carbon fibers are highly sensitive to the higher temperatures of longer treatment.

XPS results indicated that the correct treatment, with the chosen electric and power parameters, would not exceed the 10 min, limited time to have good ratio between O/C and N/C ratios, results obtained thanks to the deconvolution of C(1s), O(1s) and N(1s) high resolution spectra.

In confirmation of what has been declared above, the order and disorder bands, respectively G-band and D-band, of carbonaceous structures and of vibrational modes present in all C=C bonds, are defined before and after the treatment. Their changes and shift are the main proof of the treatment. Lastly, SEM gave morphological evidence of the treatment.

These types of characterization are not the only evidences of the success of the treatment and the benefit obtained. Typical methodologies to assert the pros of the technique adopted and to have an indication of the type of failure of the material, contemplate mechanical tensile tests such as Double Cantilever Beam (*DBC*) and End Notched Flexure (*ENF*). They return indications about the maximum values of tension at failure or energy release rate of the components reinforced in carbon fiber with a crack of a known length.

DCB and ENF requires a pre-cracked specimen to be tested. They permits to identify two elementary crack opening modes, mode I and mode II. Mode I is an opening mode, with

displacement normal both to the crack front and the crack surfaces, and symmetrical with respect to the crack surface. Mode II (and also mode III) is a shear mode, with typical separation antisymmetric with respect to the original crack surface. In this case, the displacements are parallel to the crack surface and perpendicular to the crack front. When energy release rate is an energetic indicator, the rate at which energy is transformed as a material undergoes fracture. The resistance of a material to the failure, in particular to delamination, is quantified by interlaminar fracture toughness G_c that is the other way to define the energy release rate, a well known linear elastic fracture mechanics.

The crack propagates when the energy release rate exceeds its critical value. According to the test standard chosen, there are two different value to be determined, G_{IC} and G_{IIc} respectively the energetic term for mode I and mode II. Standards propose modified theories in order to avoid overestimation of these parameters. [12]

Mode I fracture behaviour could be examined over a wide range of rates starting from a low crosshead speed to the high rate test. Load displacement curves were recorded to identify the various types of crack growth: type I-ductile stable, type II-brittle unstable, and type III-brittle stable. [13]

Smiley et al. [13] measured the fracture toughness values at the onset of crack growth, for carbon fiber/*PEEK* (thermoplastic resin) and for carbon fiber/epoxy samples pre cracked.

The former reached an average value of 1.5 to 1.7 kJ/m^2 as mode I fracture toughness, up to an opening rate of 7 x 10^{-7} m/s. The latter showed a value of G_{IC} around 0.17 kJ/m^2 up to an opening rate of 2 x 10^{-8} m/s, then began to decrease with increasing rate, and it continued to decrease with rate to a value of 0.04 kJ/m^2. The sudden decrease could be qualitatively related to the effect of rate on the interaction of the plastic zone and the graphite fibers.

Zabala et al. [14] tested unidirectional and woven carbon fiber composites with bi-components epoxy resin as matrix, in DCB test. The G_{IC} values obtained fluctuate between 0.4 – 0.8 kJ/m^2, testing the samples according to the ASTM D5528 and Modified Beam Theory to avoid end rotation and deflection of the crack tip issues, having used hinges for the load application and not loading blocks.

Murray et al. [15] conducted static test with several theories for the evaluation of G_{IC}: simple beam, modified beam, modified compliance calibration and compliance calibration method G_{IC}. The components were unidirectional carbon fibers/epoxy thermosetting matrix $[0]_{18}$.

The results differs for tens of J/m^2 according to the different theory adopted: initially, for crack length near to 65 mm, the G_{IC} measured was 140-160 J/m^2 while, at the end of the test the value rose until 200-230 J/m^2 with crack length of 110 mm.

The application of plasma treatment on the surfaces of CFRPs as well as virgin fibers or carbon fabrics adopted for the manufacture of the final composites, remains a coveted subject of study that aims to increase mechanical resistance and delamination.

Sarikaya et al. [16] treated CFRP surface with APPJ surface treatment to remove contaminants and increase the adhesion in bonding performance. The increase in toughness was investigated through DCB test by evaluating the increase in G_{IC} between plasma treated specimens and wiped specimens with isopropyl alcohol wipes. The plasma-treated specimens showed up to 85% increase of G_{IC} compared to the other method.

One aspect that remains challenging is the automatic crack tip monitoring during propagation when the test is in progress.

The position of the crack was defined manually by the operator according to the methods described by the appropriate standards, making it necessary to have a certain type of technical staff and longer times than those foreseen by the most recent monitoring through image acquisition with high resolution cameras.

The Digital Image Correlation (*DIC*) allows to automate the analysis of the crack growth for mode I and II delamination tests, and consequently makes it possible to have a more immediate evaluation of the fracture toughness vs crack length (a) value.

A graduated paper scale is applied to the components to be tested with a resolution such as to allow a post-test measurement from the acquired images, and a speckled pattern is also applied to the lateral surface of the piece to allow the software to calibrate and analyse image correlation (2D and 3D) to evaluate the range of displacements and deformations within the results of the DCB and ENF test, as detailed by Murray et al. [15]

1.1. Purpose of the study

In the present work, two different gas source (N_2 and N_2-H_2) are chosen for the plasma treatment of 2x2 twill carbon fiber woven fabric samples, commonly used in the automotive industry as reinforcement of composite materials. The epoxy chosen as matrix is a bio epoxy with a 31% of bio content (glycerol in place of petroleum-based propylene).

The aim of this work is to asses the possibility to increase the mechanical properties of *CF*/epoxy composites thanks to the plasma pre-treatment, in terms of increased wettability of carbon fibers and adhesion with the epoxy matrix. As previously stated, those composites are not able to show their full potential in terms of exploiting the maximum adhesion, without any surface treatment, so it is necessary to perform the aforementioned treatment in order to make it possible. In this study, the effect of the atmospheric pressure plasma treatments and its optimal calibration are studied and critically analysed from a chemical and mechanical point of view, searching for the difference between the untreated composites and treated ones.

The surface of untreated and treated carbon fiber fabric samples are preliminary studied through chemically and optically characterization before the vacuum infusion fabrication process by means of ATR spectroscopy and Raman spectroscopy in order to understand the surface chemical composition of the surface analysed. This allows to identify the best treatment to be used for the carbon fiber fabric treatment considering the polymeric matrix chosen for the final composites.

In conclusion, the analysis of the mechanical results as well as the evaluation by means of DIC application and post-processing of fracture toughness G_C, give further and final confirmations about the effectiveness of plasma treatment.

1.2. Carbon fiber fabric composites

Carbon fiber/polymer matrix composites are commonly used in the automotive and industrial sectors. Starting from the manufacture of the fibers through heating, oxidation and carbonization processes of the chosen precursor, the final composite is obtained by means of various technologies including vacuum infusion of carbon fiber fabrics hand lay up, with the adoption of thermoplastic or thermosetting matrix. The final result is a component with high mechanical characteristics which depend on the degree of adhesion between fiber and matrix. The method of manufacturing carbon fibers is illustrated below, with particular attention to the use of Polyacrylonitrile as a precursor. Next, the different composite fabrication technologies are presented together with their structural characteristics.

1.2.1. From precursor to carbon fiber

Carbon fibers can be prepared from polymeric precursor materials such as polyacrylonitrile (*PAN*), cellulose, pitch and polyvinylchloride.

Pitch-based carbon fibers have higher graphitic nature with respect the PAN-based ones, with poorer compression and transverse final properties.

PAN is obtained from the polymerization of the monomer Acrylonitrile, an organic compound with the formula CH_2CHCN with a vinyl group linked to a nitrile.

Acrylonitrile and its comonomers polymerization is done by one of following methods:

- *Solution polymerization*, with preparation of the dope made directly during the process of polymerization;
- *Bulk polymerization*, as auto-catalytic process not so much commercially applied;
- *Emulsion polymerization*, restricted to precursors with acrylonitrile content less than 85% (modacrylics) and so not relevant for a carbon fiber precursor;
- *Aqueous dispersion (slurry) polymerization*, which is the most common method used for textile fibers.

The attraction of PAN precursor is due to its chemical composition: this polymer has a continuous carbon backbone and the nitrile groups are ideally placed for the occurring of cyclization reaction, producing a ladder polymer.

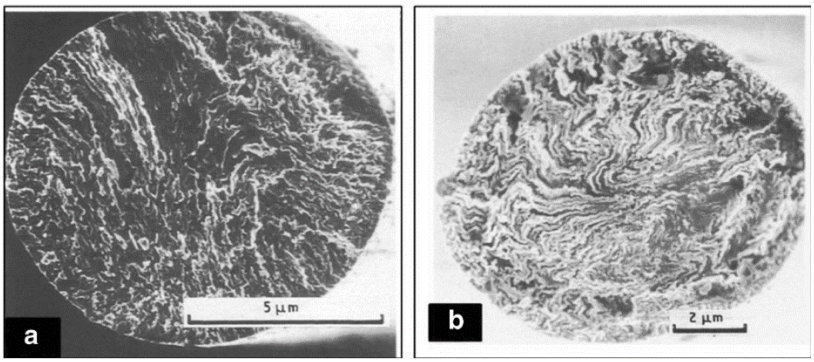

Figure 1: SEM images of cross section of (a) PAN-based and (b) pitch-based carbon fibers - [17]

A plausible mechanism of formation of carbon fiber from PAN is shown in *Figure 2*.

Starting from this material, the main steps that leads to the CF formation are:

- Heating;
- Oxidation;
- Carbonization.

PAN has to fulfill determined requirements to achieve proper manufacturing of carbon fibers. Some of the more important requirements to produce an acceptable precursor are [2]:

- A polymer with an acrylonitrile content less than 85%, or a homopolymer, will not make a satisfactory PAN precursor. Carbon content of acrylonitrile is 67.9% that assure a PAN carbon yield of some 50-55%, enough to guarantee the production of high modulus fibers. The choice of comonomer(s) of acrylonitrile does have a most important role in the peroxidation stage of the carbon fiber manufacturing process;
- The molecular weight and molecular weight distribution of the polymer have to be carefully controlled. These values are controlled by means of specified quantities as number average molecular weight (M_n), the weight average molecular weight (M_w) and the ratio M_w/M_n called polydispersity index. These quantities are direct expression of the rheological properties of the polymeric material: high molecular weight is related to the high degree of orientation of crystal plane along the resultant fiber axis.

Once the PAN is obtained, it is heated at 300 °C in air, with consequent rupture of triple bonds C≡N existed along polymeric chains and consequent cyclization to form ring structure, tetrahydropyridine, typical of chemical composition of graphitic components. Consequently,

oxidation treatment at 700 °C results in the breakdown between carbon and hydrogen bonds and the rings previously formed become aromatic, releasing hydrogen in gaseous form.

Further heating steps at 400-600 °C and then up to 1300 °C, respectively low temperature carbonization and high temperature carbonization process in presence of inert gas (i.e.: argon), lead to a conversion of ring structure to aromatic pyridine groups by dehydrogenation and nitrogen removal. Firstly, heating causes the loss of hydrogen atoms obtaining a ribbon like structure constituted by three aromatic rings chains with nitrogen atoms at the ends.

After that, heat is again gradually applied and increased in order to form extended ribbon-like structure through progressive lateral fusion of ribbon polymers, and nitrogen atoms are ejected in gas form.

The homogeneous increase of temperature leads to increase the fiber modulus of the final product with almost pure and regular graphitic structure of polymers. [17]

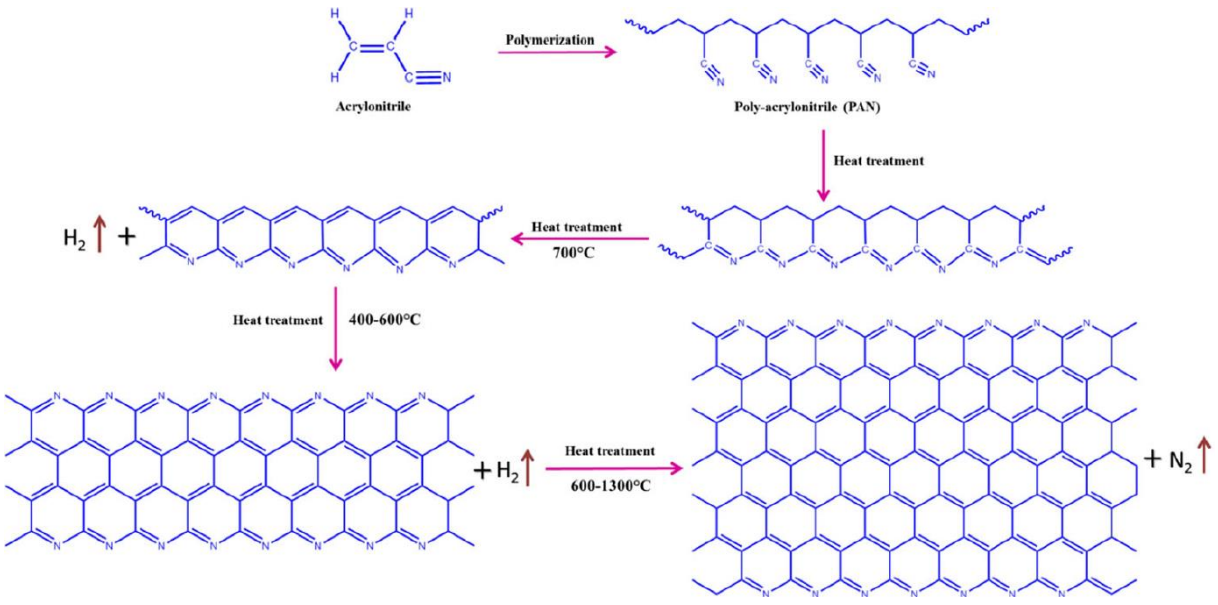

Figure 2: Carbon fiber fabrication from precursor PAN - [17]

During forming of CF, internal core structure of fiber is created by high binding symmetrical carbon elements, whereas outer structure is generated by low binding energy carbon elements (lack of active carbon atoms) but with compact arrangement.

In particular, the inner core layer is composed of small-scale graphite microcrystalline disorder layers while skin layer counts for increased crystal size of graphite microcrystalline. From the core layer to the skin layer, the arrangement is gradually orderly.

The unbalanced low binding energy outer skin carbon elements explains the reason why it is necessary to carry out a surface treatment while maintaining the characteristics of the bulk material, which are essential to preserve the high mechanical characteristics of the material.

Final products are usually collected in tows using online winders: large tows are generally plaited into cardboard boxes, these latter positioned on a plaiter table while smaller tows (50k) can be collected in tubs.

PAN-based CF appears with almost circular shape and notches are observable on its surface depending upon the tension applied during formation. Notches and groves create interaction via mechanical interlocking with polymeric matrixes.

Low processing temperature CF exhibits small pores but higher in quantity, vice versa high processing temperature makes large pores onto CF surface but small in numbers. Another important dimension except the pores one (1-10 nm) is the CF diameter: it has a dramatic effect upon crystallite thickness, amount of carbon content and degree of graphitization.

Crystal lattice structures are essential in describing how interactions among different planes of atoms work and how different planes of atoms will interact. The arrangement of carbon atoms is understandable analysing graphitic and amorphous carbon structures.

Graphitic carbon has a crystal lattice that resembles a hexagonal close-packed structure with alternating layers of carbon planes of ABA type as shown in *Figure 3* . High atomic packing factor is achieved with consequent high degree of order within the structure.

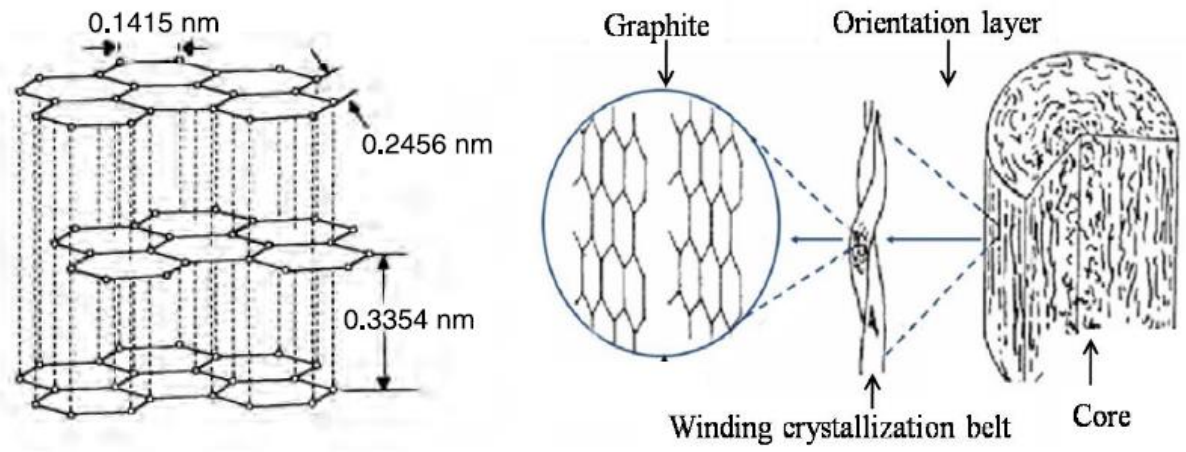

Figure 3: Scheme of an ideal graphite crystal lattice structure (right) and carbon fiber structure (left) - [2]

Conversely, amorphous carbon crystal lattice has a diamond like structure showing a low atomic packing factor, and it is hardly dependent on the type of precursor utilized for the manufacturing process.

Hybridization theory describes better the interaction and bonding state onto CF surfaces. Atomic orbital conformations are affected by the different hybrid types: sp, sp^2 and sp^3. The last two are important for carbon materials because they reflect order and disorder (graphitic and amorphous) structures, essentials for Raman spectroscopy characterization that is sensitive to hybridization changes and so surface changes in carbon materials.

1.2.2. Carbon fiber composite

Composites are made by two or more separate materials (metals, polymers or ceramics) combined in a structural unit. In a composite the constituents remain physically separable and distinct from each other, making an heterogeneous structure.

A composite is made by a soft and weaker matrix in which a strong and stiff reinforcement is distributed within the matrix. The most common example of reinforcement is the fiber: fibers are embedded in a binder o matrix material. Particle or flake reinforcement are also adopted but they are generally not as effective as fibers. [18]

Fibrous reinforcement is very effective thanks to the polymer chains alignment, preferable to the randomly orientation.

The alignment assure good resistance properties in one direction with respect to the others: in longitudinal reinforcement the elastic lamina module E_1 is mainly dominated by the elasticity of the fibers while in transverse direction, E_2 is dominated by the matrix elasticity.

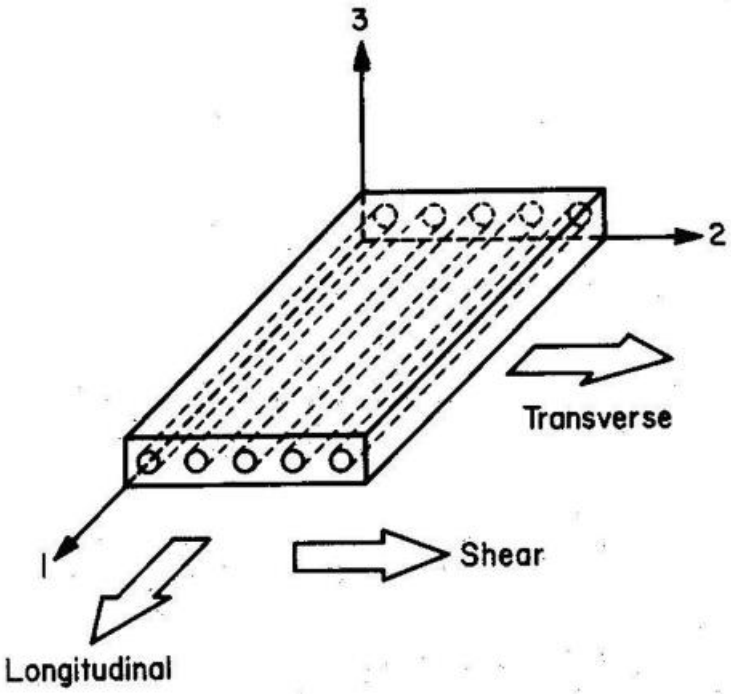

Figure 4: Layer/lamina with unidirectional reinforcement - [18]

Fibers alone are not used due to the impossibility to support long compressive loads and for the poor transverse mechanical properties. They need to be held together in a structural unit with a binder or matrix material that could also protect fibers from damages or environmental attack.

The matrix has structural, protective task but also distributes the applied load to the fibers. It contributes through properties such as ductility, toughness and electrical insulation according to the final component requests.

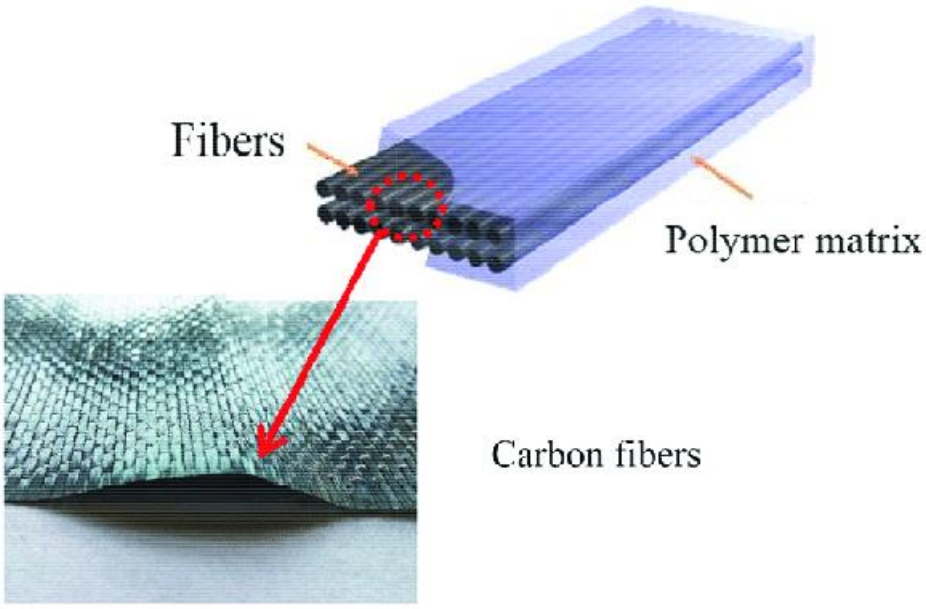

Figure 5: Carbon fiber composite - [17]

Matrix and fiber materials should be chemically compatible in order to avoid some undesirable reactions especially at high exercise temperature of composites. Polymers are the most used matrix materials [19] :

- Thermoset matrixes such as epoxy, polyester and phenolic; they form cross links, 3D molecular net that does not melt at high temperatures, during curing cycle. Epoxy resins give an excellent link fibre-matrix and consequently a big resistance to fracture (70-90 MPa as tensile strength when heat cured), but its high value of viscosity makes not easy the complete wetting of the fibers by matrix, contrary to polyester resins which boast of a low viscosity;
- Thermoplastic matrixes such as polymide, polysulfone, polyprophilene; they are based on polymer chains that do not cross-link hence at high temperatures, they soft and melt to return at hardened state after cooling cycle.

Carbon fiber is a synthetic fiber and it is usually preferred among all the other synthetic fibers due to its high strength (around 2.1 – 2.5 GPa of stress at rupture) but especially for:

- high strength to weight ratio;
- high value of elastic modulus, E (240 – 390 GPa, around three times the one of glass type);
- low density, ρ and high E/ρ ;
- high thermal and electrical conductivity as well as good corrosion resistance.

To fully exploit the potential of this reinforcement, the fiber/polymer matrix interaction must be able to rely on strong physicochemical interactions at the interface, such as covalent bonds, van der Walls and hydrogen bonding forces: van der Waals forces are weaker than covalent bonds that are chemical bonds in which two atoms put in common electrons couple for a stable link. The former instead depend on the attractive and repulsive forces between atoms at a certain known distance. [17]

Carbon fiber reinforcement plastic (*CFRP*) counts for continuous fiber or short fiber with the former that gives high improvement to the composites with not easy fabrication process.

CFRP are made by several fabrication processes: compression moulding, extrusion, injection moulding, resin transfer moulding (to obtain intricated shapes), vacuum infusion. These methods are chosen according to viscosity property and density level of matrix.

C.Soutis [20] highlights the usage of CFRP in aeronautic field made by hand layup technique in which either unidirectional fiber tapes or woven fabric are impregnated into the resin, placed into the mold (*bag mold*), and forced to individual plies together by introducing high pressure or vacuum. Once the resin has terminated the impregnation, thermal and pressure cycle has to be driven through the curing cycle: gel formation (initial polymerisation), curing with heating under pressure to achieve high compactness with good link fibre-matrix and low residual stresses produced during the previous thermal cycle, and finally the post-curing phase with heating of the polymer at high temperature in order to obtain a further hardening of the matrix, particularly suitable when the matrix adopted is a thermoset resin.

Compared to unidirectional composites and nonwovens, composites with fabrics as reinforcement system are more impact resistant and have uniform properties in all directions.

A.Buhu et al. [21] analyses all the textile fabric type used as reinforcement in industrial filed from technical clothes to transport field. They are used as insertions in composites and are obtained by different methods of binding/joining of textile materials such as fibers or yarns: weaving, knitting etc. .

Textile structures used as reinforcement differs from fabrics to braids and knitted ones and their aesthetics are shown in *Figure 6*.

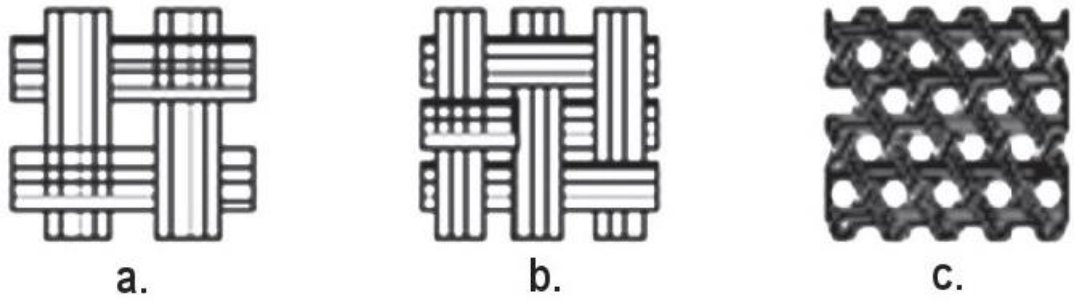

Figure 6: Different types of carbon fiber textile structures: (a) plain woven fabric; (b) twill fabric; and (c) braid - [21]

The choice among these types of textile fabric depends on how composites has to be processed and on their requirements, capacity of multiaxial reinforcement and between the layers.

To enhance the adhesion between the fiber and the matrix interface, the inert fiber surfaces have to be modified by chemical or physical means.

What is missing on CF surface is a proper oxygen content on surface, result of last step of CF manufacturing process, as well as nitrogen concentration, polar dispersive components and active site concentrations. Stating that, its surface come out as chemically inert and hydrophobic with inadequate active groups leading to poor interfacial strength.

Low reactivity is driven by the functional groups presence onto the surface. They represents part of the molecule structure characterized by specific elements and by a well defined and precise structure, that confers to the chemical compound its typical reactivity. Basically a functional group constitutes the centre of the chemical reactivity of the molecule.

Surface treatments allow to solve adhesion issues. Plasma treatments is particularly suitable for these kind of components.

1.3. Surface treatments

Surface modification, chemical or physical, affects surface properties avoiding any bulk properties alteration. In the case of carbon fiber materials, the preferable method is the chemical one: the presence of functional groups determines the strength of the fiber-matrix interactions and in order to increase the number, different methodologies are adopted such as oxidation, reduction, deposition, grafting or more simply cleaning and ablation or etching.

Z.Xu et al. [22] increased wettability of CF/epoxy matrix with oxidation-reduction and pre-irradiation induced methods through modification in acrylic acid. Compared with the as-received carbon fiber, the surface of the modified one became rougher with high number of tiny fragments stuck on it. With proper characterization methods, it was observed an increase of oxygen content of fiber surface, of the surface free energy and of the number of functional groups that enhance the wetting and adsorption between CF and epoxy resin, such as carbonyl, carboxyl or ester groups.

Hung et al. [23] showed the benefits of the volumetric scanning electro-polymerization coating techniques to the CF/epoxy interface. The active functional groups introduced onto fiber surface were -OH, NH2, and -COOH.

Plasma treatments are more environmental friendly methods, quite different from the aforementioned processes and it is nowadays diffused as carbon fiber surface treatment method.

1.3.1. Plasma treatments

Plasma is an ionized gas made by electrons in excited state and atomic or molecular radical species. It is obtained when gases are subjected to a strong energy source of various type (electric, thermal, irradiation etc.) however it is convenient and highly industrially adopted the ionization through electrical and electromagnetic fields. The exposure of the components to the plasma, as well as the wet methods, can modify the surface chemical composition in different ways. Among the various results of the process there is the production of highly reactive sites by means of radicals deposition, cleaning of contaminants and etching.

In the initial part of the process, the interaction of ions, electrons and radicals with the substrate cause a rapid removal of contaminants (release agents, sizing traces, adsorbed species etc.) on

the amorphous region of the surface and this step of the process is denominated “plasma cleaning” effect, typical of processes whose aim is the increase in hydrophily of the surface, opposite to the wetting increase of a-polar components. [24]

If a longer treatment time is chosen, not only a cleaning effect is observed: deeper ablation process of the more regular part of the sample, crystalline fraction, is possible with a strongly increase in the surface roughness as a result. These two effects are the “etching effects”.

When electric discharge is used to generate plasma, if the electric field is high enough, an electron obtains more energy from it than it loses through collision with neutral particles, so it can accelerate under the electric field and result in breakdown of gas particles when they collide.

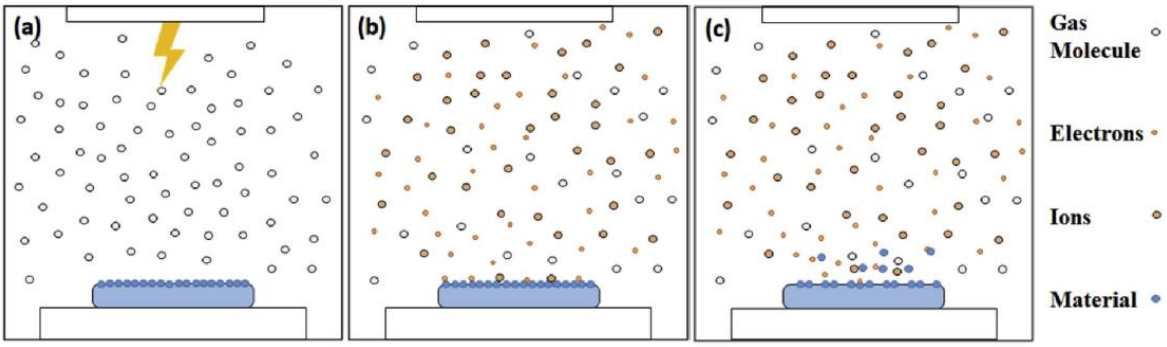

Figure 7: Plasma etching process steps: (a) plasma generation, (b) collision of plasma species on the sample surface, and (c) removal of material due to the plasma - [25]

The approach used for the basic understanding of the evolution of gases in plasma it is through the use of kinetic theory, with some basic assumptions about the nature of molecules (i.e.: gas is made by identical molecules, molecules are relatively uncompressible, they are in constant and random movement determined by their temperature, etc.).

If the neutral particle temperature after the collision is significantly increased and close to the electron temperature, the plasma is classified as *equilibrium plasma*. A typical equilibrium plasma made in laboratory is the arc discharge driven by DC power but they are preferred for welding, cutting and waster material treatment due to the high exercise temperature reached (several thousand of Kelvin degrees). For thermal sensitive component, the treatment requires a plasma with gas temperature that stays close to the room temperature. Such plasma with a gas temperature much lower than the electron temperature, is classified as *nonequilibrium plasma*.

Nonequilibrium plasma treatment differs from thermal plasma due to the fact that electrons, escaped from atoms or molecules due to the high energy electric field, are in non thermodynamic equilibrium state with the other chemical species: their temperature and kinetic energy is higher than the one of the other heavier ions and neutral entities.

The higher is the temperature, the higher is the average motion of the molecules. Energy acquired or lost through collisions (E_k) is correlated with particle mass (M) and their speed (v) by the expression:

$$E_k = \frac{1}{2} M v^2 \tag{1}$$

In a large population, molecules reaches a wide range of energies and the energy of a single molecule is constantly changing.

The energy distribution of this population of molecules is statistical and is described by the function known as the Maxwell-Boltzmann distribution.

Energy distribution can be defined by a single quantity that is the temperature (T) while the average speed of the molecules ($\bar{c}$) in the gas is given by:

$$\bar{c} = \sqrt{\frac{8\ kT}{\pi M}} \tag{2}$$

where k is the Boltzmann constant and its value is equal to $1{,}38*10^{-23}$ $J*K^{-1}$, T is in Kelvin and M is the molecules mass in kg.

To evaluate the average kinetic energy of molecules in a gas, the squared average speed is requested and, for the Maxwell-Boltzmann distribution is given by:

$$\overline{c^2} = \frac{3kT}{M} \tag{3}$$

Hence the average kinetic energy of molecules is linked to the gas temperature by the equation:

$$\langle E_k \rangle = \frac{1}{2} M \overline{c^2} = \frac{3}{2} kT \tag{4}$$

Another important parameter that influences the outcome of the treatment is the density of the species composing the plasma (electrons, ions and neutral species) by which the degree of

ionization can be defined as the ratio between the charged species compared to that of the neutral gas [26]:

$$\alpha = \frac{n_i}{(n_i + n_o)} \tag{5}$$

where n_i is the ions amount while n_o the neutral species amount. α increases as temperature increases because n_i is proportional to the temperature, whereas it diminishes when n_o decreases. According to the α value a plasma could be *fully ionized* $(\alpha = 1)$ or *partially ionized*. Typical value of industrial plasma or laboratory plasma is $\alpha = 10^{-6}$ with a range of 10^7-10^{20} $\frac{species}{cm^3}$ as plasma density.

One of the most commonly used temporal-controlling methods is the dielectric barrier discharge (*DBD*) but highly limited due to the low frequency pulsed discharge that restricted the total energy delivered, and due to the drastic decrease in effectiveness with the plasma-component distance. This limit in the short discharge gaps significantly reduce the size of the objects that could be treated if direct treatment is desired.

To solve this kind of problem, atmospheric pressure plasma jet (*APPJ*) open space technology is preferred. Unlike vacuum or low pressure plasma, APPJ technology does not require the use of a separate chamber system or an extremely short jet-component working distance. This particular technology is widely adopted for the pre-treatment of steels, aluminum, plastic and polymeric materials thanks to the ease of operation in industrial production and due to this wide range of substrates that can be processed (thermosensitive and not).

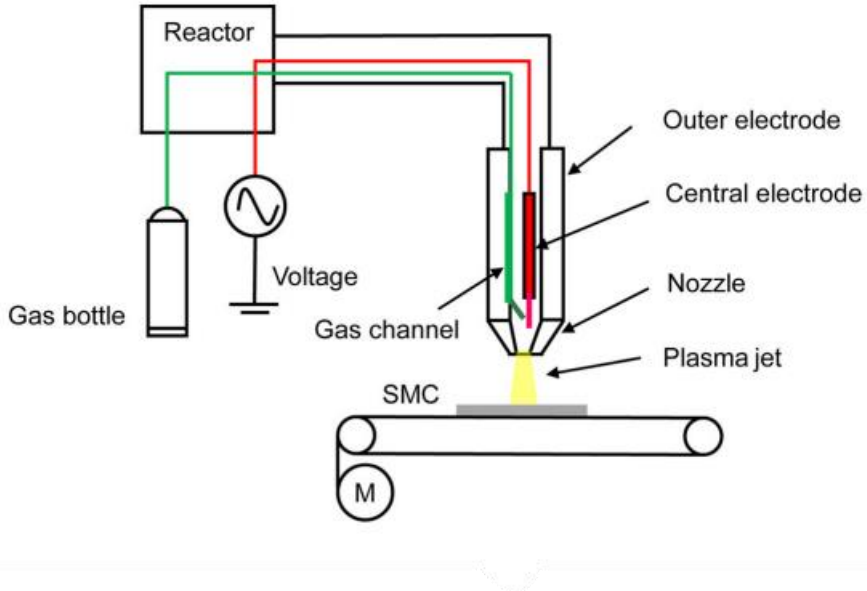

Figure 8: APPJ scheme - [27]

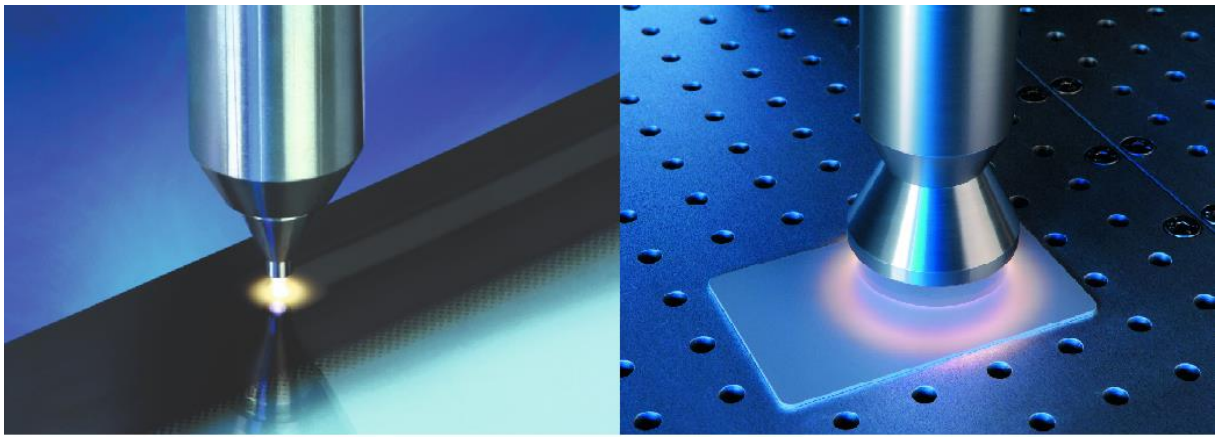

Figure 9: APPJ removal action (left) and activation action (right) – [28]

Wang et al. [29], used APPJ treatment to clean the surface and activate Sheet Moulding Compound substrates before testing them in a quasi-static lap-shear tests to prove the increase in adhesion with a two-component room temperature-cured epoxy adhesive used as adhesive bonding. Trough a channel made by a central electrode and an outer coaxial electrode, gas is ionized with a resultant jet of plasma gas. If the plasma is designed to be at fluctuant potential, the substrate must not be grounded, vice versa it is necessary to design a proper insulant component (i.e.: glass plate) or the substrate itself could act as insulating material.

Plasma is ejected through a nozzle. Different kind of nozzles are commercially available: rotating nozzle, potential free nozzle, linear band nozzle etc. . Wang used a circular nozzle with

a plasma jet width of 4 mm with a gas flow pressure of 0.25 MPa and 25 to 10 mm as distances, operating discharge voltage of 8kV and a discharge frequency of 12 kHz. Speed of the plasma jet and distance plasma jet-substrates are crucial for the effectiveness of the treatment according to the exposure time plasma-samples.

Similar experiment was driven by Ceregatti et al. [10]. Carbon fiber fabric was treated with radiofrequency plasma with a N2H2 gas mixture to create functional groups with -NHx or -N, thus promoting conditions for polyaniline (PAni) grafting allowing a better adhesion with thermosetting matrix, especially epoxy.

1.3.2. Process parameters of plasma treatments

The desired chemical modification can be obtained by choosing a suitable gas and gas flow rate as well as the other treatment parameters: excitation power, treatment time, distance jet-substrate and nozzle speed path.

Gas flow rate may affect the wetting properties, but the results is still strongly influenced by the gas mixture chosen. As previously seen, the treatment conducted by Ceregatti et al. [10] with N_2H_2 gas and subsequent PAni grafting, made it possible to obtain an excellent response between the carbon fiber substrate and PAni with a significant reduction in the contact angle.

Tiwari et al. [9] used N_2 and N_2/O_2 as gas for cold remote plasma treatment at high power. Discharge was produced in a quartz tube with a distance between the discharge and the treatment zone of 900 mm. Despite the setup is different from a typical APPJ treatment, the effects on carbon fiber fabrics are chemically comparable. The CF/PEI and CF/PEEK composites manufactured were tested by means of tensile, flexural and ILSS tests and the treatment showed excellent results in terms of increase in ILSS and limited in tensile strength and toughness, albeit better than untreated components. In particular, they stated an increase in terms of tensile strength of 17% for CF/PEI with N_2/O_2(1%) treatment and an increase in toughness for the same composite of 26%.

For what concern the power requires to asses a proper plasma treatment, the field chosen of power supply is the radio frequency (RF) power or microwave power while the average processing power of the plasma of a APPJ process stays in a range 200-800 W according to the type of nozzle and gas chosen. The increase in power is correlated to the increase in plasma

density (hence ionized flux) and, with a proper gas flow rate usually from 5 $\frac{l}{min}$ to 60 $\frac{l}{min}$, is possible to define a correct ionization degree compatible with the treatment.

Kim et al. [30] treated CF/epoxy bisphenol-based resin composite with atmospheric pressure plasma surface treatment to improve adhesion properties. The gas chosen was an inert gas, helium, and a He/O2 mixture with a flow rate of 5 $\frac{l}{min}$ and power from 50 to 200 W. The CFRP surface originally hydrophobic was easily turned hydrophilic and increasing power and treatment time as well, load at break was enhanced reaching a better adhesion. In particular at 200 W and 50 s condition, with a jet-component distance of 1 mm, the load at break was 3 times higher than the non-treated joints.

However long plasma treatment times had to be avoided, leading to the selective ablation of the epoxy resin and to uncovering of the carbon fibers, weakly attached fibers to the surface as result.

Lastly, another important parameter that is classified as secondary parameter, is the working distance nozzle jet-substrate. It is necessary that the correct distance is found out so that the substrate is correctly invested by the primary beam whose species density is higher therefore with a degree of ionization effective for the treatment to be carried out. It is commonly used in the prototype phase, to trace a suitable experimental curve of points that investigates the correct distance or at least that can minimize the working window for the given substrate, compatibly with the physico-chemical characterizations of the components treated at various distances.

As previously anticipated, the work of Wang et al. [29] allowed to obtain increases in the mechanical properties of joints between SMC components by APPJ plasma treatment, for different jet-component distances: the as-received component recorded a lap-shear strength of 5.1 MPa reaching values of 10.2 MPa after a treatment whose distance has been set at 25 mm until reaching the maximum value of 23.1 MPa with a distance of 20 mm. Further decreases in the relative distance between the two components did not give benefits, indeed a reversal of the trend was recorded.

1.3.3. Surface characterization methods

In order to assert the correct functioning of the treatment or to analyse the surface state of the as-received component to be treated in such a way as to make an adequate choice of the process parameters according to the goal to be achieved, surface characterizations remain a weapon more than valid to achieve the purpose.

Among the chemical and optical characterization methods there are:

- Scanning Electron Microscopy (*SEM*) coupled with Energy Dispersive X-Ray (*EDX*) probe;
- Attenuated Total Reflection (*ATR*) spectroscopy and Fourier Transform Infrared (FTIR) spectroscopy;
- X-ray Photoelectron Spectroscopy (*XPS*);
- Raman Spectroscopy;
- Contact angle and surface free energy (*SFE*) measurement.

The methods listed above allow for a chemical and physical analysis of the surface. In particular, SEM allows you to observe the morphology of the components at higher magnifications than optical microscopes and at the same time offers a surface chemical analysis when the EDX probe is used.

In the case of analysis of carbon fabrics or even better carbon fibers, the SEM offers indications about the level of smoothness detected following the fiber manufacturing process (wet spinning of PAN precursor production) or the roughness achieved after plasma treatment. The oxidative effect due to the treatment and observed through this type of characterization increases the total acidic functions and simultaneously increases the surface area as defined by the work of L. Nohara et al. [31].

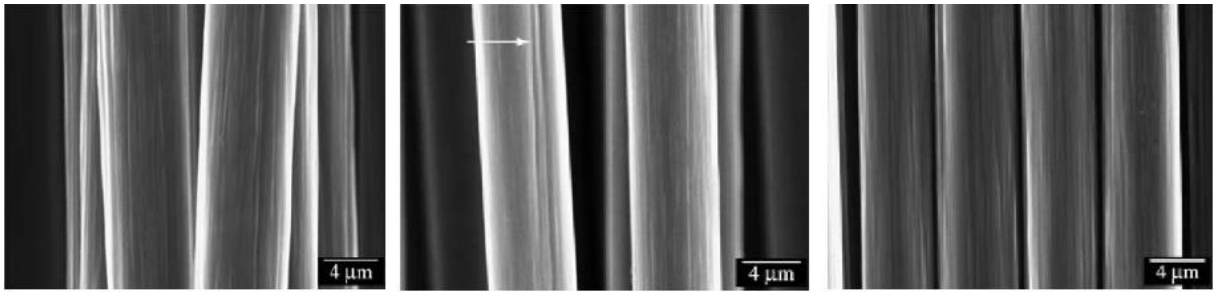

Figure 10: SEM image of carbon fiber: untreated sized (left), 10 minutes in nitric acid bath (middle), and 2 minutes of oxygen plasma (right) – [31]

As shown in *Figure 10*, the treated fibers showed some micrograph after nitric acid treatment, with increased roughness and etching more transversely oriented along the fiber's axis. With oxygen plasma treatment was also noticed striated pattern along the fiber's axis.

When SEM is properly equipped with EDX probe, the atoms on the surface are excited by the electron beam emitting specific wavelengths of X-rays that are characteristic of the atomic structure of the elements. An energy dispersive detector is mounted to analyse these emissions assigning the corresponding elements.

FTIR and ATR are another commonly used techniques to investigate the presence of chemical structures on the surface of a sample. FTIR is based on the total internal reflection phenomenon and it is schematically described in *Figure 11*.

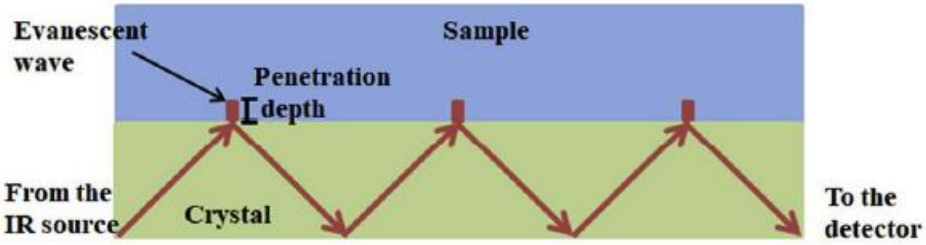

Figure 11: Scheme of ATR-FTIR phenomenon – [32]

As described by Sundriyal et al. [25], these methods works thanks to an infrared beam that enters the ATR crystal, and it undergoes several reflections between the crystal and the investigated surface. The internal reflections produce an evanescent wave which penetrates the sample. Several parameters determines the penetration depth: type of crystal used, incidence angle, and wavelength. It is generally in the range of microns. Type of bonds that are present over the investigated surface influences the absorbance frequency of the incident light. With

this method is so possible to collect information about the chemical composition of the sample surface using bonds energy and in particular variation of dipole momentum of molecules.

Tiwari et al. [9] treated carbon fibers with cold remote nitrogen-oxygen plasma (CRNOP) and FTIR-ATR spectra revealed the presence of oxygenated polar functional groups: ether, carboxyl and carbonyl groups were observed on spectra corresponding to wave number range 950-1200, 1650-1710 cm^{-1}, as showed in *Figure 12*.

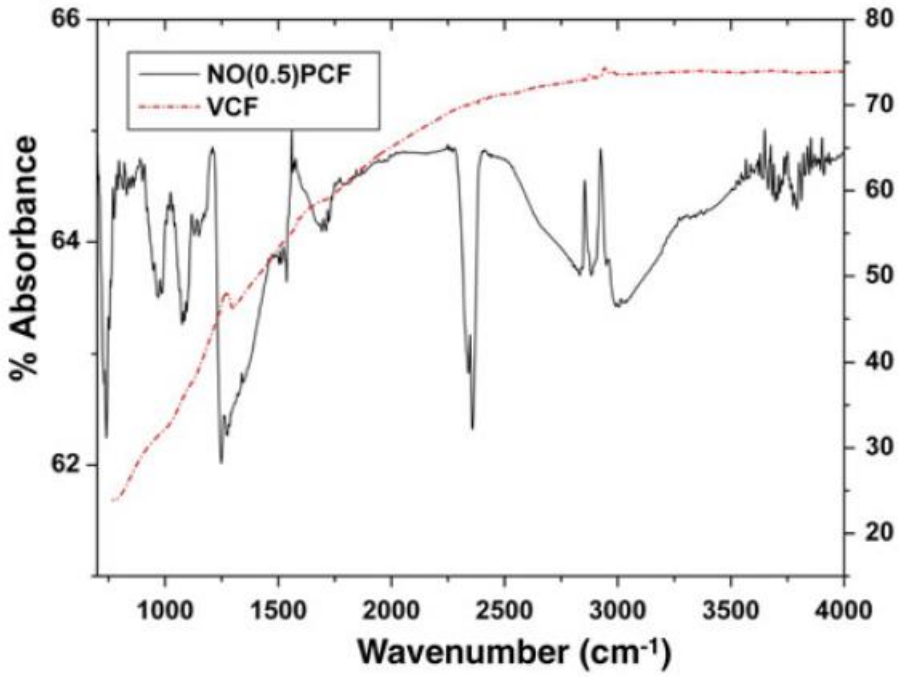

Figure 12: FTIR-ATR spectra for as-received fibers and treated fibers with mixed plasma N_2/O_2 - [9]

Another important characterization method used to know the activation and mixing effect of the surface chemical species of the treated sample, is Raman spectroscopy which returns information about the possible surface organic and inorganic compounds and the structural changes of the material by exploiting the polarization variations of the bonds molecular.

The principle is the same as for ATR-FTIR spectroscopy but part of the light hitting the sample is scattered at a different wavelength compared to the incident one: it is called Raman scattering and the difference between the incident and scattered Raman light is called Raman shift. The energy difference represents the amount of energy needed to vibrate or rotate the molecule.

What is observed are the changes in the order and disorder bands of the graphitic structure of the fibers, and their I_D/I_G ratio. The order band or G band settles around 1590 cm^{-1} and is

attributed to the planar configuration sp^2 of the carbon-carbon bonds as well as referring to the degree of graphitization of the fibers. The disorder band, around 1360 cm^{-1}, is due to the vibration of the bonds of the sp^3 hybridized carbon and is induced by the disorder.

Tiwari et al. [9] in addition to analysing the results of the FTIR spectrum, it evaluated the I_D/I_G ratio for the untreated and treated samples: the value increased from 0.86 to 0.94 which confirms the distortion in the graphitic structure of the fibers.

A similar increase in the ratio was recorded by Nohara et al. [31], from 2.26 to 2.82, with O_2 cold plasma treatment of carbon fibers, similar to further treatments with a different gas or other chemical source as shown in *Figure 13*.

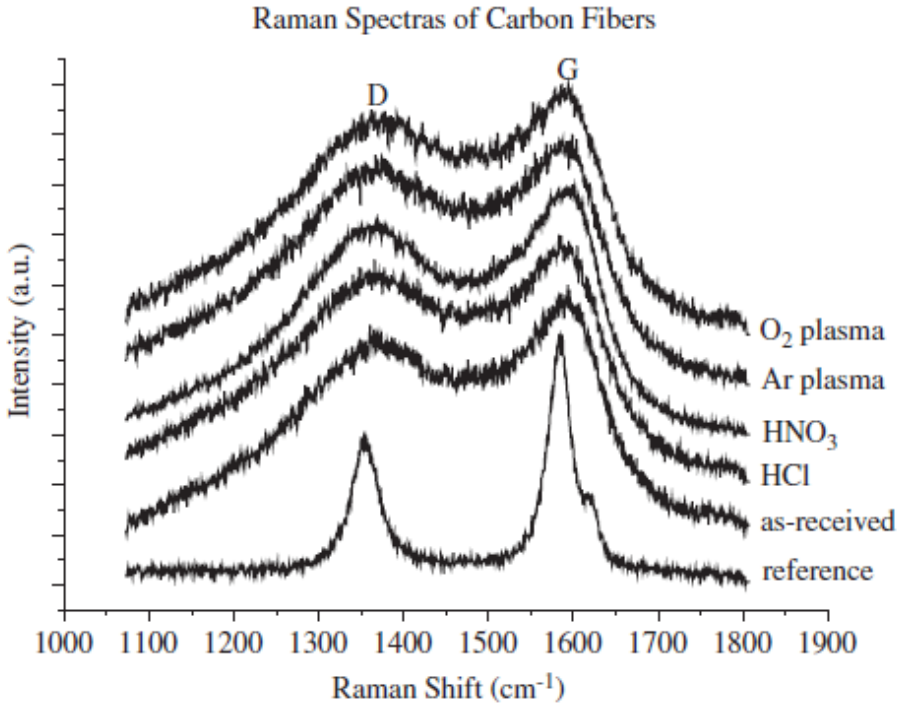

Figure 13: Raman spectra of as-received carbon fibers, treated with acids, by plasma process, and heat-treated at 2100 °C (reference) – [31]

In the same research, XPS was done on the virgin samples and treated ones. XPS is based on photoelectron effect: when a sample is hit by electromagnetic radiation with energy E=h*v , in the X-ray region, it is registered electron emission of internal energetic levels. Electrons in material's atoms stays on energetic levels called orbitals, with a proper binding energy. Measuring the kinetic energy of photoemitted electrons, binding energy is derived. This link basically depends on the chemical element to which the atom belong and on their energy level.

Looking at the spectra it is possible to determine which elements are present in the sample.

Nohara analyses thanks to this characterization method, the relative content of oxygen to carbon changes according to the conditions of the surface treatment. The as-received carbon fiber presented the lowest O/C ratio with number of functional groups attributed to the residual of the polymeric precursor, PAN, and was probably due to the carbonization temperature and sizing of the fibers. After the oxygen plasma treatment, the ratio O/C slightly increased from 0.88 to 0.91, result of introduced functional groups and favouring the ablation of the CF removing carbon atoms in form CO and CO_2.

Lastly, wettability may also be determined by measuring the contact angle, with proper OCA goniometer, between the sample surface and the drop of a reference liquid such as distilled water. It is also a measure of surface energy level. [7]

A small contact angle indicates that the liquid is wetting the polymer effectively, while large contact angles show that the wetting is poor.

Every surface has a critical surface tension, γc, of wetting. Liquid with surface-free energies below γc will have zero contact angles and will wet the surface completely, as result of perfect hydrophily. In contrast, liquids with surface-free energies above γc will have finite contact angles. The critical surface tension is in units of dynes/cm at 20 °C where dyne is a unit measure of force in Centimetre-Gram-Second unit system.

1.4. Fracture mechanics and delamination

Composite materials usually exhibit the best qualities of their constituents and qualities that neither of the constituents possesses. Modern composite materials use high-strength fibers in a resin matrix, combined with them to form a single ply. Composites laminates are formed by stacking plies of different orientations according to the usage and loading of the final component. To obtain an orthotropic material, unidirectional (0 degree) ply can be modeled otherwise with different angle orientation, layered anisotropic composite is obtained. Then it is cured under high temperature and pressure to asses the proper link between fibers and resin. [33]

The damage mechanism may involve one of the material's components or more than one, or the interface between the two. Macroscopic damage mechanism are: fibre breakage, fibre buckling (instability of fibred due to compressive load), debonding (at matrix-fibre interface), intralaminar fracture or matrix cracking, and interlaminar fracture or delamination.

One of the most common failure modes of composite structures is delamination between plies. It is a crack in between adjacent plies. A delamination can be viewed as an interface crack between two anisotropic materials and it causes a loss of stiffness as well as a reduction in mechanical strength with a final catastrophic failure that could occur.

Stress field and strain energy release rate are applicable to these delaminations and used as indicator for the resistance of the composite.

The most common sources of delamination are the material and structural discontinuities that give rise to interlaminar stresses. Delamination can occur: at the stress-free edges due to mismatch in properties of the layers, at ply drops where thicknesses must be reduced, at regions subjected to out-of-plane bending, etc. . When delaminations occur, failure modes *Mode I*, *II* and *III* are usually present.

Mode I is an opening mode, with displacement normal both to the crack front and the crack surfaces, and symmetrical with respect to it. *Mode II* and *mode III* are shear modes and they are characterised by separation antisymmetric with respect to the original crack surface. The distinction between the two are in relative motion of displacements with respect to the crack

surface and crack front: for *mode II* they are parallel to the crack surface and normal to the crack front while in *mode III* they are parallel to both the crack surface and to the crack front.

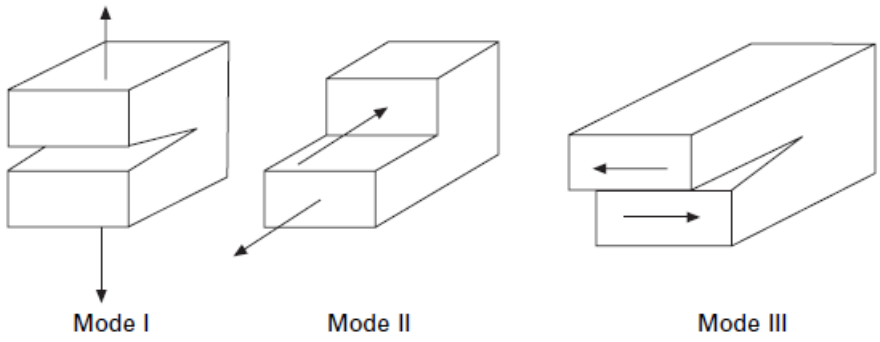

Figure 14: Delamination fracture modes – [33]

In linear fracture mechanics, a cracked body is regarded as linear elastic in the whole region and possible inelastic processes within or outside the process zone around the crack tip, could be present and must be restricted to a small region. Of fundamental importance is the crack-tip field and the stresses and strains close to it. [34]

To asses and quantify the material resistance, stress analysis as well as energetic analysis could be conducted. In particular, resistance of the material to the delamination is determined by interlaminar fracture toughness G_c computation. For each of the fracture modes, the interlaminar fracture toughness and the corresponding energy release rate (G_I, G_{II} and G_{III}) must be characterized.

The strain energy release rate, G, associated with crack onset and growth is a measure of the delamination driving force. This value must be determined and compared to the measure fracture toughness G_c, to predict delamination growth. Typically, G_c vs crack length a is studied.

Let consider our component as an elastic body containing a crack with a defined boundary, subjected to external tractions and where along the boundary, certain displacements are prescribed. The external tractions are assumed to have a potential energy Π_{ext}.

Due to this external action, the system shows an energy balance as:

$$U_{tot} = U^* + \Pi \tag{6}$$

in which the sum of potential energy stored in the system, U^*, and energy absorbed to form the crack surface, Π, gives as result the total energy of the system.

If we differentiate U_{tot} with respect the crack area A we could define the strain energy release rate as a contribution of $\frac{\partial U_{tot}}{\partial A}$, in particular:

$$G = -\frac{\partial U^*}{\partial A} \tag{7}$$

When the potential energy released reaches the energy required for crack growth, critical condition for the crack is achieved, i.e. $\frac{\partial U_{tot}}{\partial A} = 0$. This means:

$$G_c = -\frac{\partial U^*}{\partial A} = \frac{\partial \Pi}{\partial A} \tag{8}$$

with G_C identified as critical value of strain energy release rate.

When G is higher than this critical value, the crack propagates given a defined criterion for crack growth.

Looking again at the energy amount, the potential energy U^* is equal to the strain energy U less than external forces W:

$$U^* = U - W \tag{9}$$

But the work, in a load-controlled system is equivalent to the product between the external load P and the crack opening displacement increment, $d\delta$.

The change in strain energy is:

$$U = \frac{P\delta}{2} \tag{10}$$

Considering, under these conditions the potential energy as $U^* = -U$ and for a planar case, with width of the plate, b, constant, it is possible to define G through differentiation with crack length a and not the full crack area A, as:

$$G = -\frac{\partial U^*}{\partial A} = \frac{1}{b}\frac{\partial U}{\partial a} = \frac{P}{2b}\frac{\partial \delta}{\partial a} \tag{11}$$

Griffith and then Irwin and Kies, who laid the foundations for many of the fracture mechanics developments, demonstrated that for a material exhibiting linear elastic behaviour, the strain

energy release rate could be related to the load applied, in a cracked plate through compliance parameter, $C = \frac{\delta}{P}$, via:

$$G = \frac{P^2}{2b}\frac{\partial C}{\partial a} \tag{12}$$

This equation stands as the theoretical basis of all delamination tests in quasi-static conditions, from 0.5 to 5 mm/min of opening rate, depending on the geometry and material characteristics.

If linear elastic theory is not enough, it is possible pass from elementary beam theory or direct beam theory to compliance based beam method (*CBBM*) corrected with some parameters that could take into account out of plane deformation, root rotation at the crack tip and proper stresses concentration. Different test equipment are used according to the delamination Mode studied.

1.5. Mode I and Mode II delamination testing

Mode I and *mode II* delamination testing are studied according to specific standards related to the type of composite material that is used as test specimen.

The aim is the determination of interlaminar fracture toughness G_C both in *mode I* and *mode II*, with two different standards.

Composites made by carbon fiber fabrics and epoxy resin, with a precrack obtained during the fabrication process, could be tested with double cantilever beam (*DCB*) test as well as End Notched Flexure (*ENF*) test respectively for *mode I* and *mode II* test.

The *ASTM* standards used to define the geometry, the experimental setup and procedure are *ASTM D5528/D5528M* and *D7905/D7905M*.

1.5.1. The double cantilever beam test

A prismatic, constant width and thickness composite beam, called double cantilever beam is used according to the *ASTM D5528/D5528M* to evaluate the fracture toughness in *mode I* for CFRP samples. [35]

The crack is introduced starting from the manufacturing process, in this case by means of hand layup infusion in vacuum of layers of carbon fabrics, in a middle plane position with respect to the number of even layers that must be stacked, and on only one of the ends of the component. This is obtained using a non-adhesive insert, usually Polytetrafluoroethylene (*PTFE*) such as *Teflon*^{TM} or aluminized paper with a wax applied on both surfaces, that can avoid the adhesion of the layer with the fiber reinforced material. The load will be introduced by an appropriate traction machine on the end where the crack is present, through the use of *piano hinges* or *loading blocks*. The load will be applied orthogonally to the plane of the crack and to the longitudinal median axis of the component itself in such a way as to cause the opening of the ends and the longitudinal propagation of the crack.

The crack will propagate when the critical strain energy release rate is reached, in accordance with the theory of fracture mechanics previously presented.

To facilitate crack cracking, a graded scale is placed on one side of the specimen and the specimen side is coated with a layer of white to increase contrast. The most recent applications involve the use of high-resolution cameras that can automatically detect, with high-frequency images acquisitions, the progress of the crack during the test. This involves the application of a particular pattern that can facilitate the recognition of areas subject to deformation, especially close to the crack tip. The pattern is usually a speckle in order to make easy the recognition of the crack by modern software that exploit DIC, during the application of the load.

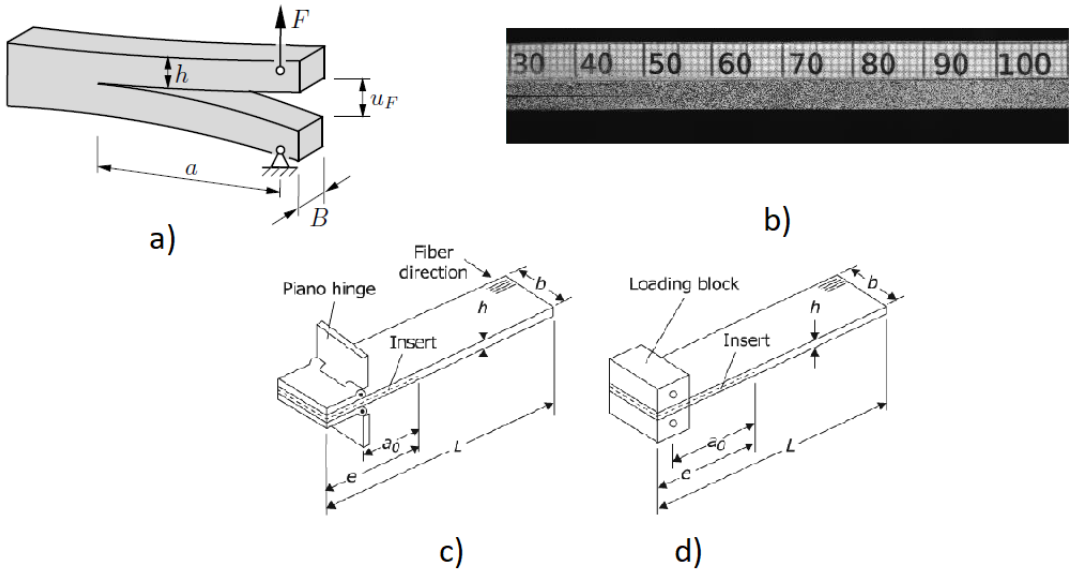

Figure 15: a) DCB specimen, b) speckle pattern on the DCB specimen side, c) piano hinge and d) loading block – [33] [35]

As previously mentioned, the types of fixtures are hinges or loading blocks, as shown in *Figure 15*.

It is common to prefer loading blocks to avoid unexpected results due to the bending effect with the foresight to proper design them for the components to be tested, according to the geometric specifications, in such a way as not to produce any excessive stiffness effect on the specimen which would compromise the results obtained. In this case, a corrective factor is still expected to correct any results that would inevitably be overestimated, according to the specific standards. The choice of one type of fixture with respect to the other is left to the researcher.

Specimen shall be at least 140 mm long and nominally from 20 to 25 mm wide. They are cut from the manufactured panels (i.e., water cut), and the total insert length has to be 76 mm for loading blocks used as fixtures. This distance counts for the initial delamination length plus the

extra length required to bond the loading blocks. The laminate thickness shall typically be between 3 and 5 mm with initial delamination length, a_0, measured from the load-application point to the end of the insert, typically of 50 mm. However, very low values of a_0/h are not recommended and for very low values (<10), data reduction procedures given in the standard, may not be accurate.

The material recommended for loading blocks bonding to the specimens, is a room temperature cure adhesive.

The test consists of two loading-unloading cycles with loading crosshead rate constant and between 1 and 5 mm/min while the unloading rate is upwardly limited to 25 mm/min. The initial loading allows to generate a clean precrack and it is continued until the crack propagates from 3 to 5 mm away from the insert. The reloading takes place at the same opening rate of the first step and continues until the crack reaches at least 30 mm away from the precrack.

After the test, the quantities that has to be recorder are: load P, thanks to the load cell action, the corresponding load line displacement δ and crack length a. This latter is monitored looking at the propagation of crack tip, optically using a traveling microscope with a proper resolution (at least 0.5 mm) or with a DIC equipment to asses the correlation of consequent images taken by high resolution camera while the specimen undergoes deformation.

The value of toughness given by initial *a0* measurement, corresponds to the delamination growth from the insert and is obtained from the initial force-displacement plot. The second value of toughness corresponds to delamination growth from a precracked delamination front and is obtained from the force displacement plot after subsequent reloading. These values, with propagation results of G_{IC} may be used to generate the Resistance curve, *R-curve*.

The first two values of G_{IC} shall be calculated by determining the intersection of the force-displacement curve, once it has become nonlinear, with a line drawn from the origin and offset by a 5% increase in compliance from the original linear region of the force-displacement curve. This is defined as that ranging between 25% and 75% of peak force: the first limit of the range is chosen to exclude any data affected by initial nonlinearity in the load-displacement response.

Compliance is determined using a linear least squares regression analysis of the displacement versus force data over the previously defined load range.

The intersection found could occur after the maximum force (P_{max}) and in this case P_C used for G_{IC} calculation is $P_C = P_{max}$ or it is found before P_{max} and in this case $P_C = P_{5\%}$, as shown in *Figure 16*.

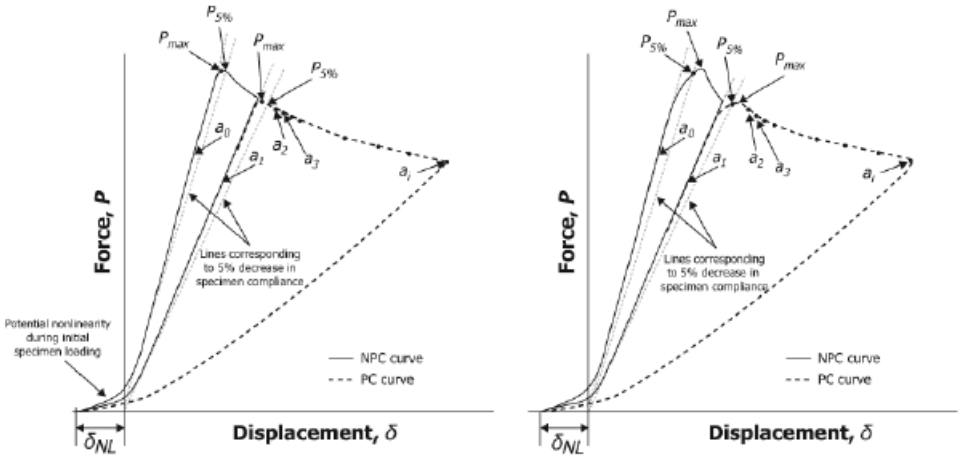

Figure 16: Example Force-Displacement curves from DCB test, values calculation based on Pmax (left) and on P5% (right) [35]

For the effective calculation of G_{IC}, compliance calibration method (*CC*) is needed, at least for the first two values computation.

For each delamination length, a_i, recorded during fracture testing, let determine the corresponding specimen compliance, C_i. The compliance is the ratio of the load-point displacement and the applied force, or δ/P while, as reported previously, the first two compliance values have to be determined from the critical forces and corresponding critical displacements values. For the other points, force and displacement values are related to the visually observed delamination growth.

Mode I interlaminar fracture toughness is computed as:

$$G_{IC} = \frac{mP_C\delta_C}{2ba} * \frac{F}{N} \tag{13}$$

with *F*, parameter that corrects the effects of large displacement at fracture while *N*, parameter that accounts for large displacements and fracture and for stiffening of the specimen by the load blocks or piano hinges. Their computation are explained in the *ASTM D5528* annex sections as well as any further explanation about other parameter like *m* that is obtained using a linear least squares regression analysis of the log of normalized specimen compliance, *log(C/N)*, versus log(a) data.

Other two methods are appliable for the G_{IC} computation:

- *Modified beam theory*: according to what is offered in the *ASTM D5528* appendix *A2* [35], this other method is presented for completeness even if the *CC* data reduction method is recommended. The beam theory expression for the strain energy release rate of a perfect built-in (clamped at the delamination front) double cantilever beam is as follows:

$$G_{IC} = \frac{3P_C\delta_C}{2ba} \tag{14}$$

In practice, this expression will overestimate G_{IC} because the beam will be not perfectly built-in (rotation may occur at the delamination front). As proposed by several authors, one way of correcting this issue is to treat the DCB as if it contained a slightly longer delamination, $a' = a + |\Delta|$, where Δ may be determined experimentally by generating a least squares plot of the cube root of normalized compliance ($C/N^{\frac{1}{3}}$) as a function of delamination length *a*, based on the observed delamination onset values and all the propagation values.

The Δ graphical evaluation as well as the expression for G_{IC} are shown following.

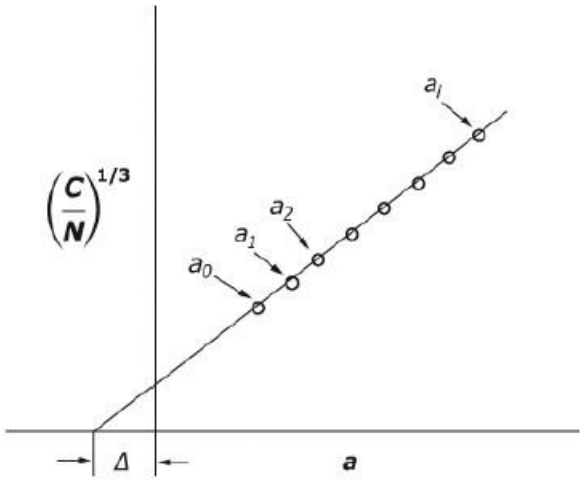

Figure 17: Modified Beam Theory: Δ evaluation in $C/N^{\frac{1}{3}}$ vs a graph – [35]

$$G_{IC} = \frac{3P_C\delta_C}{2b(a+|\Delta|)} * \frac{F}{N} \tag{15}$$

- *Modified compliance calibration method*: it is an evolution of the empirical compliance-based method and according to the standard, the expression of G_{IC} is:

$$G_{IC} = \frac{3P_C^2(C/N^{\frac{2}{3}})}{2A_1bh} * F \tag{16}$$

Where A_1 is the slope of the line shown in the *Figure 18*.

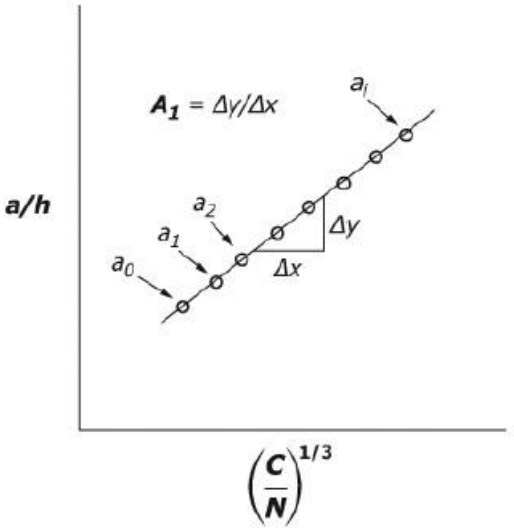

Figure 18: Modified compliance based method calibration – [35]

1.5.2. The end notched flexure test

This other test method covers the determination of the mode II interlaminar fracture toughness, G_{IIC}, of fiber reinforced polymer matrix composite laminates under mode II shear loading using the end-notched flexure test with 3 point bending fixture. The load is applied parallel to the propagation plane of the crack, in the middle point equidistant with respect to the lateral supports. Also in this case the crack grows in between the two middle halves along the plane where the precrack is made by the non adhesive insert. An universal testing machine in compression mode is used, with constant crosshead speed. During the application of the load, the specimen undergoes bending and the crack starts propagates.

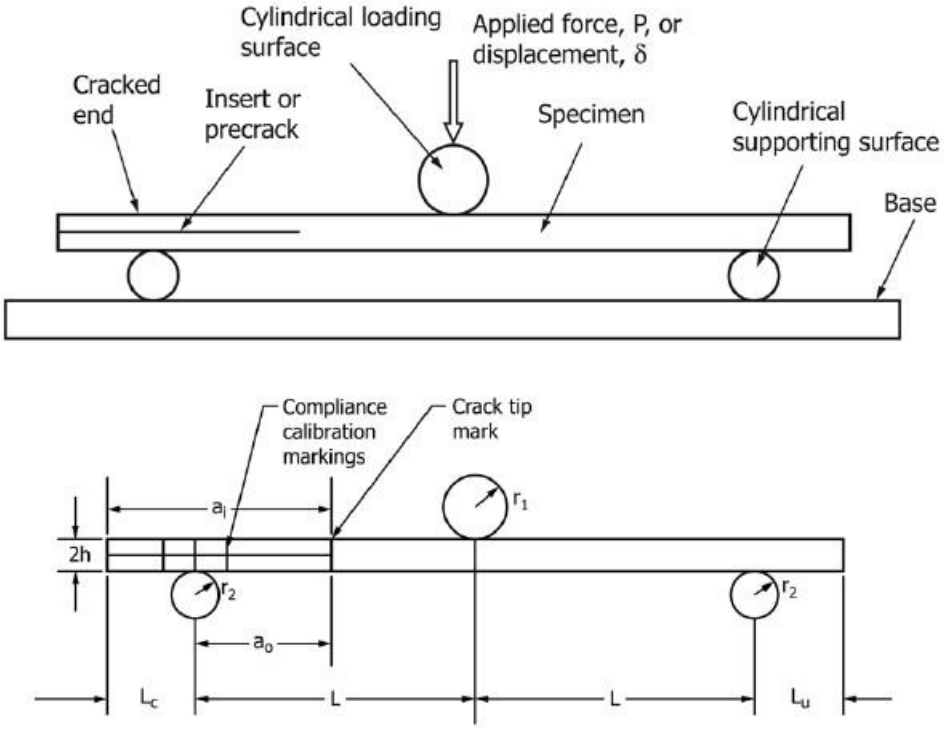

Figure 19: ENF specimen, fixture and compliance calibration set up – [36]

The ENF specimen also in this case, consists of a rectangular, uniform thickness laminated composite specimen containing a non-adhesive insert in the mid plane. Forces are applied to the specimen through an ENF fixture under displacement controlled loading.

Applied force versus center roller displacement is recorded using an *x-y* recorder or equivalent real-time plotting device while the propagation of the crack has to be monitored visually, with the help of video recording of the test or through DIC equipment.

G_{IIC} that is the energy per unit of area required for the crack growth in mode II, is obtained using the three point compliance calibration (*CC*) method. In that case, this method remains the only acceptable method of data reduction test. [36]

Constant displacement rate in the range of 0.025 to 1.6 mm/min is adopted. In *Figure 19* is shown the fixture geometry that counts for a nominal specimen span length (*2L*) of 100 mm and so a nominal half-span length (*L*) of 50 mm. The loading surface shall be centered between the two supporting surfaces and all the possible movement (i.e. rotations) of them shall be restrained.

Three point bending ENF test consists on two parts: one with sample opened in the mid plane on one end, made just by the insert during fabrication process (Non Precracked, *NPC*, step); the

other counts for a precracked sample at the beginning of the second part test with the additional precrack on the top of the insert crack tip, obtained as a result of the first step (Precracked, *PC*, step).

For both parts, the compliance was determined by a least squares linear regression analysis of the digital data to obtain the displacement versus load (δ vs P) data.

For what concern the specimens, they has to fulfill the geometrical requirements descripted in the standards so that it has to have a precrack length higher than 45 mm as well as free length next to the crack tip, of at least 115 mm. Thickness must be included between 3.4 and 4.7 mm but in bibliography slightly thinner samples were experienced.

Firstly, it is requested to compute three different compliance for the NPC sample tested: three markings are signed at 20, 30 and 40 mm from the insert ending and three different tests are conducted positioning the sample aligned with the supporting roller matching its center with the markings firstly at 20 and then at 40 mm; it is requested to load the sample until the reaching of the so called peak force CC: it is approximated using classical beam theory (*CBT*) using flexural elastic composite module E_{1f} and estimated G_{IIC} as explained in *Annex A1* in the standard. The peak force differs for each crack length that are different for the three measurement, and it is 50% of the expected value of the critical force (P_C) at that particular crack length (these are chosen to correspond to approximately 25% of G_{IIC}). After each loading phase ending, unloading is performed with a unloading speed of 0.5 mm/min, sampling rate of 5 Hz or greater and a recommended target minimum of 500 data points per test. For the NPC calibration with a = 30 mm, specimen is loaded until the delamination occurs and crack advance is detected (i.e.: drop in force curve in force vs displacement plot). Values obtained from this calibration curve unloading are used for the a_{calc} according to the procedure in the standard and the expression is:

$$a_{calc} = \left(\frac{C_u - A}{m}\right)^{\frac{1}{3}} \tag{17}$$

where C_u is the compliance of the NPC test unloading line and *A, m* are the other CC coefficients from the NPC test obtained thanks to linear least squares regression analysis (i.e.: A is the intercept and m is the slope) as explained in *Annex A3* of the standard.

This expression is the result of a rearrangement of the following expression:

$$C = A + ma^3 \tag{18}$$

If the new crack tip is clearly visible, a_{vis} is possible to use instead of a_{calc}. The former length has to be averaged between the lengths seen in both arms and it is considered acceptable if it is higher than a_{calc} and next to the left supporter taking as reference the a_0=30 mm position. Once the new crack tip is defined, it has to be marked starting from the central signal at 30 mm and this is used as new crack tip PC calibration.

New three markings are traced at 20, 30 and 40 mm from the new crack tip, as shown in *Figure 20*. The test conducted with alignment of support with marks at 20 and 40 mm signal serves for PC CC computation while the one with a = 30 mm, is used for fracture test with the same methodology seen before.

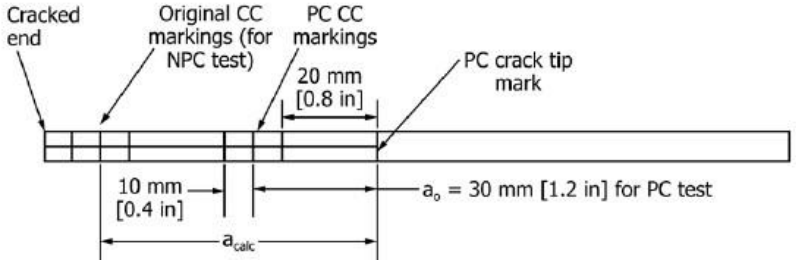

Figure 20: Configuration of specimen for precracked test with same specimen used for NPC and PC estimation – [36]

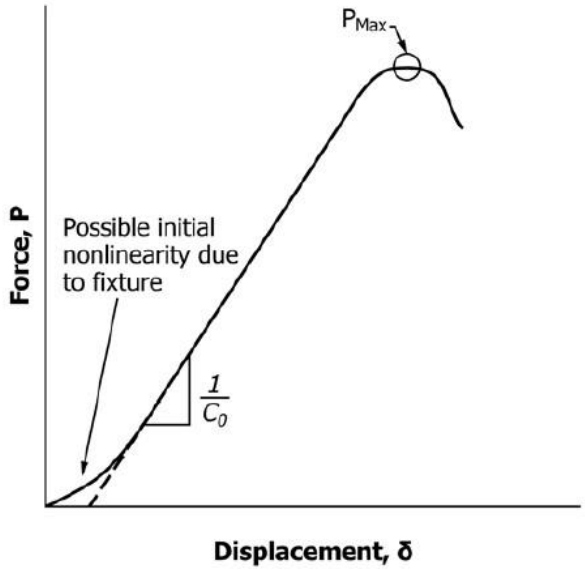

Figure 21: Compliance plot in force vs displacement graph and maximum load point determination – [36]

Possible initial non linearity (due to the fixture) is avoided excluding all the regression analysis values that are found with load lower or at least equal to 90 N, as shown in the *Figure 21* above.

O'Brien et al. [37] shown a typical fracture test load displacement plot for a ENF test computed on a graphite epoxy composite material sample and it is shown in *Figure 22*, as well as an example of a fit of compliance vs crack length *a* for NPC fracture test.

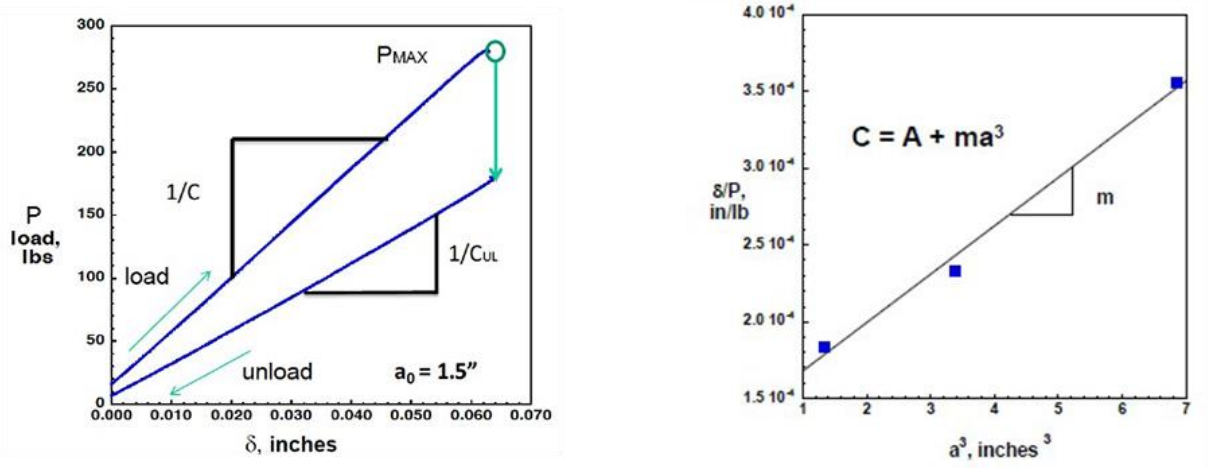

Figure 22: (left) Typical fracture test load-displacement loading and unloading plot, and (right) fit of compliance vs a^3 for NPC fracture test – [37]

The energy release rate is determined using the compliance calibration relation specified in the ASTM standard and presented as following:

$$G_{II} = \frac{P_{max}^2}{2B} * \frac{\partial C}{\partial a} \tag{19}$$

$$G_{II} = \frac{3mP_{max}^2}{2B} * a^2 \tag{20}$$

The CC data and equation 20 are used to calculate G_{IIC} by comparing the so called candidate toughness G_Q : if the difference between G_Q for NPC CC and PC CC is $15\% \leq \%GQ \leq 35\%$ they are acceptable and $G_Q = G_{IIC}$. If not, the obtained values are used to reiterate the hypothesis about the guessed G_{IIC} and Pmax.

1.6. Digital Image Correlation (DIC) system

Digital Image Correlation (*DIC*) is a no contact optical technique that allows to obtain information about deformation and displacement fields within a region of interest (*ROI*). This method based its functioning on the analysis, elaboration of subsequent images acquired during the mechanical tests. It works on all types of materials even in severe experimental configurations, as long as the ROI on the sample surface has a natural or synthetic pattern. [38]

During deformation process, a high resolution camera (or more than one) acquires images at high acquisition frequency rate. It is so possible to obtain a one-to-one correspondence between material points in the reference (initial undeformed picture) and current (subsequent deformed pictures) configurations.

DIC takes small subsections of the reference image, called *subsets*, and determining their respective locations in the current configuration. For each subset, we obtain displacement and strain information through the transformation used to match the subset location in the current configuration. This is achievable if the pattern applied to the specimen is in such a way as to follow the deformations itself.

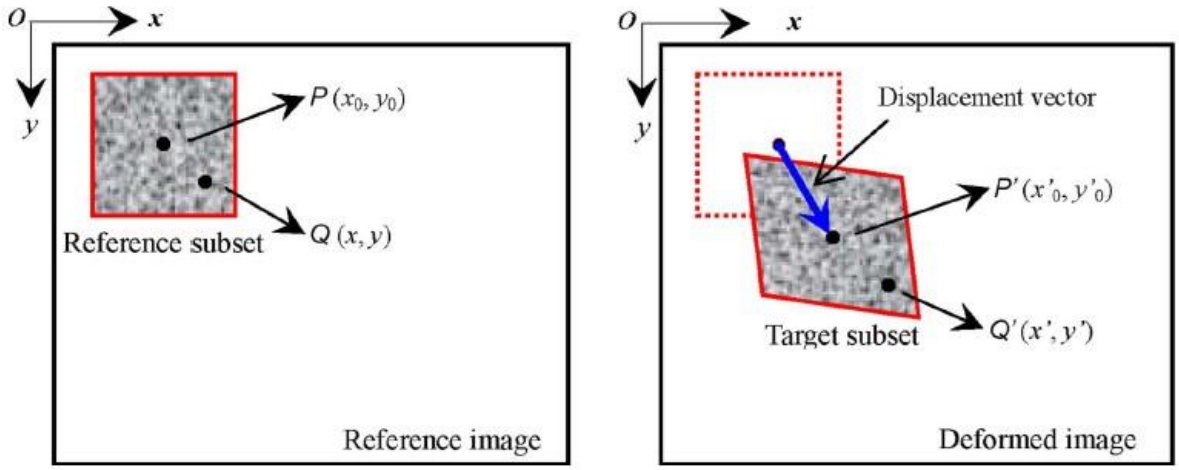

Figure 23: Basic principles of the Digital Image Correlation method – [38]

The coordinates 2D of the single surface that faces the camera are measured with a single HR camera and in this case we refers to the *2D-DIC*. Measurement in 3D requires instead a minimum number of two cameras oriented according to a stereo angle to execute the

photogrammetry in addition to image correlation. This latter method is called stereo-DIC or *3D-DIC*.

For the 2D-DIC, it is assumed that the sample is plane, that it remains planar during the test and perpendicular to the optical axis of the camera. Furthermore, the stand-off distance that is the constant distance between camera and sample tested, has to be maintained fixed. Any movement out of the analysis plane, caused by instability or rotations, will cause errors in 2D-DIC; 3D-DIC is highly recommended to overcome the aforementioned problems but it requires more precise initial setup with proper calibration and focus of sample according to the camera used.

The equipment also counts for: a data acquisition board that allows to import recorded images from camera/cameras and to link, while it acquires images, other measure instruments with output of digital signal; light source (LED or halogen) to properly enlighten the sample with appropriate focus; a computer for the correlation and processing of images.

1.6.1. Displacement and deformation computation algorithm

In order to identify univocally every point on the sample surface it is necessary to apply a proper stochastic highly contrast *pattern* with a white and black rate of 50%.

It is up to the operator to choice, according to the material adopted, whether to spray a layer of white opaque background and black opaque speckle pattern or vice versa; it is possible to invert the two coloration or working with different chromatic choices that still guarantee a high contrast.

Speckle that compose the pattern must be correctly dimensioned because it affects the measurement accuracy: undersized speckle, less than the pixel, leads to the loss of movements minors to the pixel and so the speckle is free to move inside the pixel area without influencing the light intensity; too big speckle, higher than the *facet* dimension (a facet is a pixel subdomain of *NxN* dimension), causes de-correlations.

Since the desired output is not in pixel as unit measure but in millimetres, it is necessary establish a physical scale for the measurements through a suitable calibration: a first calibration

image is taken and by using the DIC software, two points corresponding to known locations on the scale applied to the specimen are selected, inside the ROI. The operator then inputs the linear distance between the points to allow the software to generate a pixel-to-millimetres conversion factor.

Every facet is constituted by a defined set of pixels hence it is characterized by a certain light intensity *I* and its distribution. Pixels move on photographic sensor plane, because of rigid displacement or imposed deformation. DIC acts tracking various speckles on the frames to be processed returning displacement definition and, by derivation, a proper deformation field that is defined with respect to the reference configuration (or the immediately previous image), also referred to Lagrangian displacements/strains.

A group of coordinate points produce the *subset*, that comprise a finite number of pixels.

The *speckle pattern* has the characteristic aspect shown in *Figure 24* and it appears as typically composed as briefly explained before, by dark speckles of uniform shape on a higher contrast background.

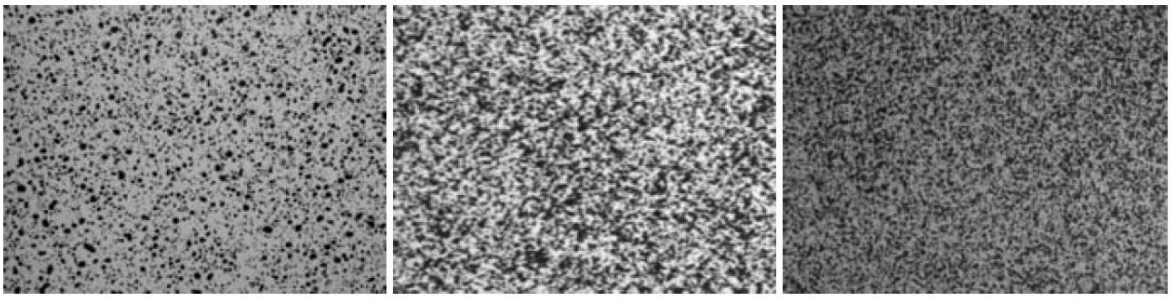

Figure 24: Examples of typical speckle pattern – [39]

Subset size and *step size* are two significant parameters to be set:

- The *subset size* controls the area of the image that is used to track the displacement between images; it has to be large enough to ensure that there is a sufficiently distinctive pattern contained in the area used for correlation.
- The step size controls the spacing of the points that are analysed during correlation; if a step size of 1 is chosen, a correlation analysis is performed at every pixel inside the *ROI*, for example.

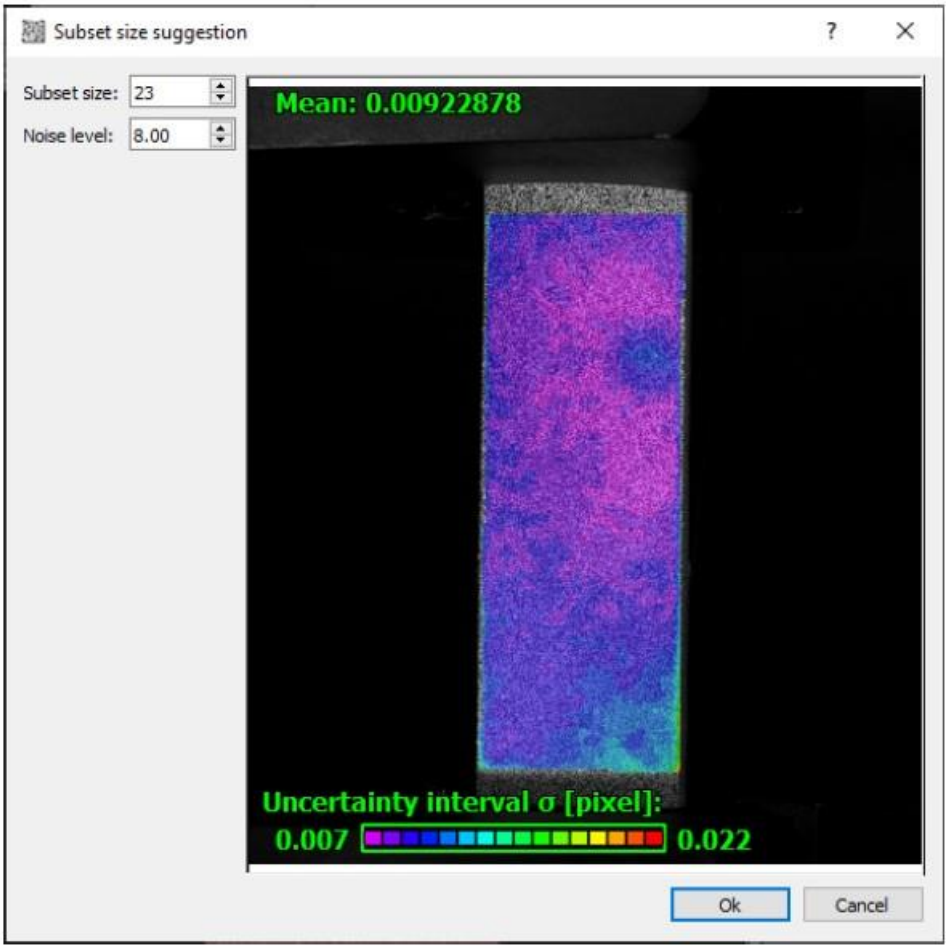

Figure 25: Subset size dialog window with recommended default values – [40]

As previously shown in *Figure 23*, let consider two points on the reference image, $P(x_0,y_0)$ and $Q(x_i,y_i)$ and points after deformation, $P'(x'_0,y'_0)$ and $Q'(x'_i,y'_i)$. These points could be correlated each others through the so called "displacement mapping function" that is a correlation function.

Being u the displacement along x and v the displacement along y, coordinates of points in instant subsequent to the imposed motion are found by means of the first order displacement function, with good approximation if the subset is small enough.

$$x_i' = x_0 + \Delta x_i + u + u_x \Delta x_i + u_y \Delta y_i \tag{21}$$

$$y_i' = y_0 + \Delta y_i + v + v_x \Delta x_i + v_y \Delta y_i \tag{22}$$

In *Figure 26*, the dependencies of the deformations on the derivatives of the displacements can be noted. This particular notation is valid in small displacement and deformation case. If this condition is not observed, second order derivatives must be introduced.

$$dx' = dx + \frac{\partial u}{\partial x}dx + \frac{\partial u}{\partial y}dy + \frac{1}{2}\frac{\partial^2 u}{\partial x^2}dx^2 + \frac{1}{2}\frac{\partial^2 u}{\partial y^2}dy^2 + \frac{1}{2}\frac{\partial^2 u}{\partial x \partial y}dxdy \quad (23)$$

$$dy' = dy + \frac{\partial v}{\partial x}dx + \frac{\partial v}{\partial y}dy + \frac{1}{2}\frac{\partial^2 v}{\partial x^2}dx^2 + \frac{1}{2}\frac{\partial^2 v}{\partial y^2}dy^2 + \frac{1}{2}\frac{\partial^2 v}{\partial x \partial y}dxdy \quad (24)$$

Higher degree of accuracy could be achieved exploiting higher order shape functions but it holds a higher number of parameters and so higher computational time as drawbacks.

Introducing conventional notation we obtain:

$$\epsilon_x = \frac{\partial u}{\partial x} \quad (25)$$

$$\epsilon_y = \frac{\partial v}{\partial y} \quad (26)$$

$$\gamma_{xy} = \frac{\partial v}{\partial x} + \frac{\partial u}{\partial y} \quad (27)$$

Applying these considerations on the continuum mechanics not only to the punctual domain but on one entire area, *subset*, the speckle will no longer be recognized but directly its light intensity.

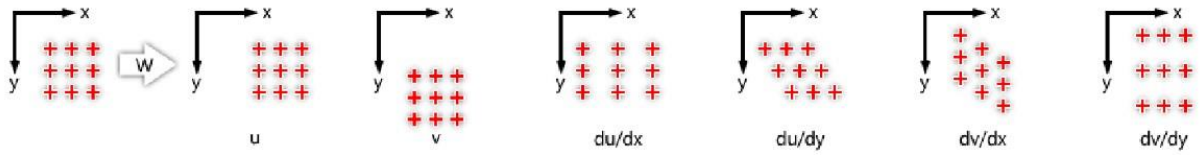

Figure 26: Linear transformations for subset coordinates – [40]

The next step is to establish a metric for similarity between the final reference subset and final current subset. This is carried out by comparing grayscale values at the final reference subset points with grayscales values at the final current subset points. This method is common among the different types of software used for DIC: *VIC-2D/3D* [39] , *Ncorr* [40], *GOM* [41], and others commonly found in literature. A square subset is chosen, rather than an individual pixel, because it comprises a wider variation in grey levels that make it distinguishable from other subsets and can therefore be more uniquely identified in the deformed image.

In this thesis work, VIC 2D/3D equipment is adopted and so all the following description is related to the its functioning and setup.

To achieve sub-pixel accuracy, the correlation algorithms that uses grayscale value interpolation, represent a field of discrete grey levels as a continuous spline: either 4-, 6-, or 8-tap splines may be selected. Generally, more accurate displacement information can be obtained with higher-order splines (highly recommended by Schreier et al. [42]) while a faster correlation analysis is achieved with lower-order splines at the expense of some accuracy.

In order to define the deformation of a subset and so to evaluate the similarity degree between consecutive subsets, three correlation criteria can be used to find the initial guess and its subsequent refinement, as investigated by Pan et al. [43] :

- *Sum of squared differences (SSD)*: affected by any lighting changes and so it is not generally recommended;
- *Normalized sum of squared differences (NSSD)*: unaffected by any scale in lighting (i.e., deformed subset is 50% brighter than reference). This is the default and usually offers the best combination of flexibility and results.
- *Zero-normalized sum of squared differences* (*ZNSSD*): unaffected by both offset and scale in lighting (i.e., deformed subset is 10% brighter plus 10 grey levels). This may be necessary in special situations but it may also fail to converge in more cases than the *NSSD* option.

The *NSSD* is presented as:

$$C_{NSSD} = \sum_{i}^{N}\sum_{j}^{N}\left[\frac{f(x_i, y_i)}{\bar{f}} - \frac{g\left(x'_i, y'_i\right)}{\bar{g}}\right]^2 \tag{28}$$

with $\bar{f} = \sqrt{\sum_i^N \sum_j^N \left[f\left(x_i, y_j\right)\right]^2}$ and $\bar{g} = \sqrt{\sum_i^N \sum_j^N \left[g\left(x'_i, y_{,j}\right)\right]^2}$ being N the dimension of the subset in pixel while f and g are the grey values of the reference subset and current/target subset respectively.

The matching procedure is basically completed through searching the peak position of the distribution of correlation coefficient, σ. Once the correlation coefficient extremum is detected, the position of the deformed subset is determined. The differences in positions of the reference subset center and the target subset center yield the planar displacement vector at point P.

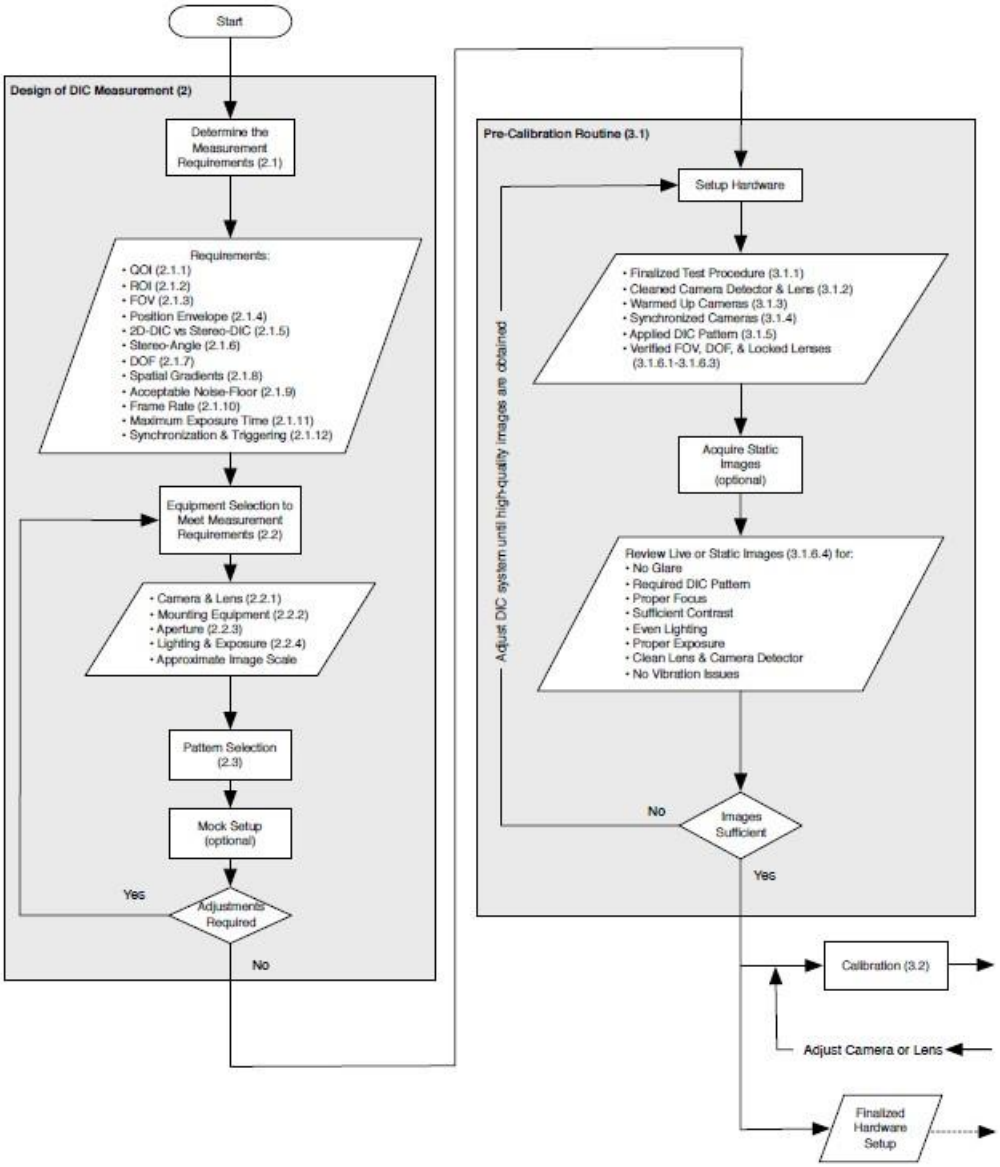
Start
Design of DIC Measurement (2)
Determine the Measurement Requirements (2.1)
Requirements:
• QOI (2.1.1)
• ROI (2.1.2)
• FOV (2.1.3)
• Position Envelope (2.1.4)
• 2D-DIC vs Stereo-DIC (2.1.5)
• Stereo-Angle (2.1.6)
• DOF (2.1.7)
• Spatial Gradients (2.1.8)
• Acceptable Noise-Floor (2.1.9)
• Frame Rate (2.1.10)
• Maximum Exposure Time (2.1.11)
• Synchronization & Triggering (2.1.12)
Equipment Selection to Meet Measurement Requirements (2.2)
• Camera & Lens (2.2.1)
• Mounting Equipment (2.2.2)
• Aperture (2.2.3)
• Lighting & Exposure (2.2.4)
• Approximate Image Scale
Pattern Selection (2.3)
Mock Setup (optional)
Yes
Adjustments Required
No
Pre-Calibration Routine (3.1)
Setup Hardware
• Finalized Test Procedure (3.1.1)
• Cleaned Camera Detector & Lens (3.1.2)
• Warmed Up Cameras (3.1.3)
• Synchronized Cameras (3.1.4)
• Applied DIC Pattern (3.1.5)
• Verified FOV, DOF, & Locked Lenses (3.1.6.1-3.1.6.3)
Acquire Static Images (optional)
Review Live or Static Images (3.1.6.4) for:
• No Glare
• Required DIC Pattern
• Proper Focus
• Sufficient Contrast
• Even Lighting
• Proper Exposure
• Clean Lens & Camera Detector
• No Vibration Issues
Adjust DIC system until high-quality images are obtained
No
Images Sufficient
Yes
Calibration (3.2)
Adjust Camera or Lens
Finalized Hardware Setup

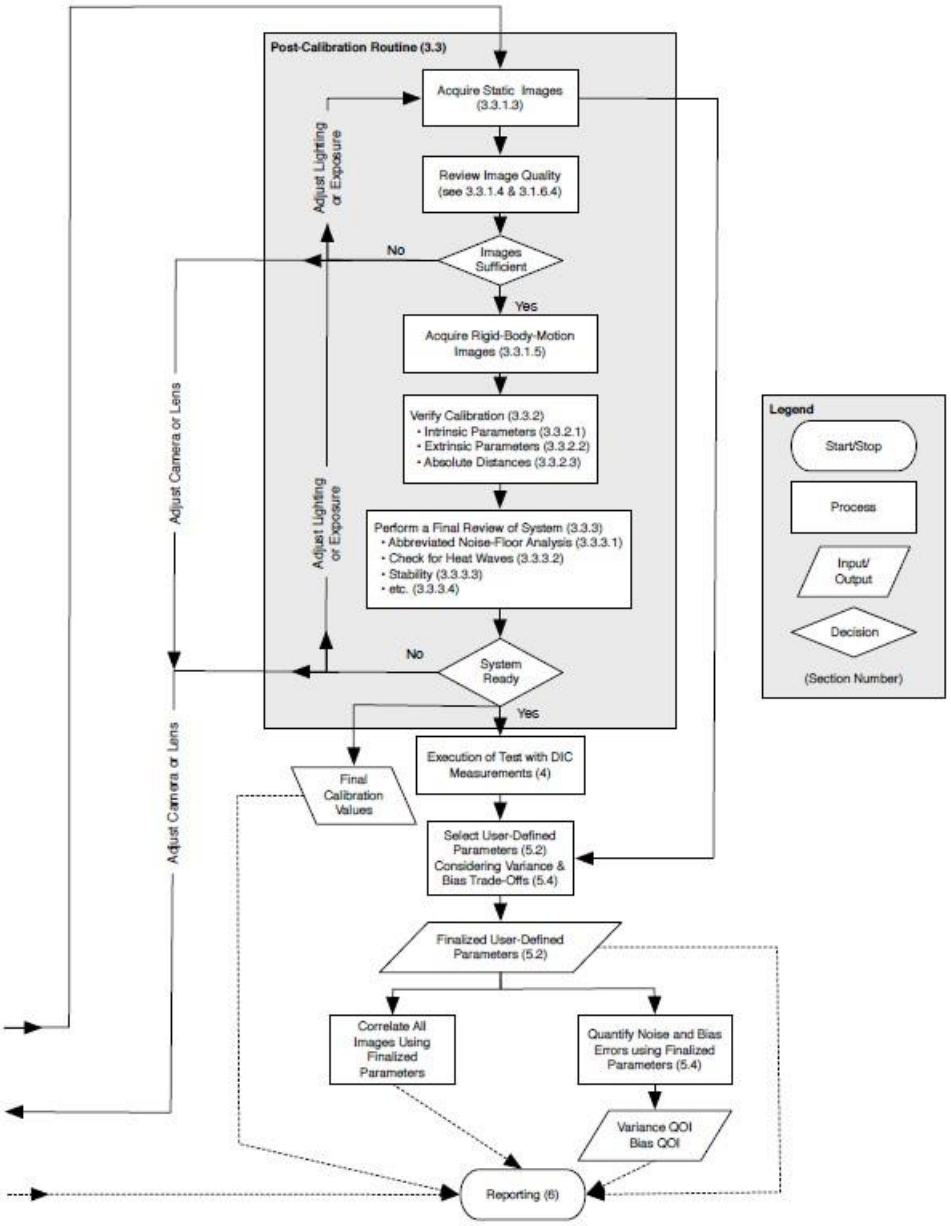

Figure 27: Flow chart of DIC measurements in conjunction with mechanical testing of a planar test sample (part 1 and part 2) – [39]

2D DIC method normally requires an accurate initial guess of the deformation before achieving sub-pixel accuracy; sub-pixel registration algorithm should be used and the most common choice is based on iterative spatial cross-correlation algorithm (e.g. the Newton-Rapson method, genetic algorithm etc.) that only converges when an accurate initial guess is provided and it stops when the stopping criterion is reached, difference between two iterations lower than the imposed tolerance. A proper subsection in VIC 2D during the pre-processing is aimed at this set up.

A net transition between subsequent dark and bright elements has to be avoided, it is preferable instead a gradual transition with multiple grey values involved, like a "blurring" effect, to improve the matching mechanism among subsets. For this reason, a pre-processing solution is proposed and usually adopted through *low-pass filter*, obtainable by imperfect focus during acquisition photographic or better by means of digital filtering of the acquired images. This choice allows us to remove some high-frequency information from the input images and reduce aliasing effects in images where the speckle pattern is overly fine and cannot be well represented in the image.

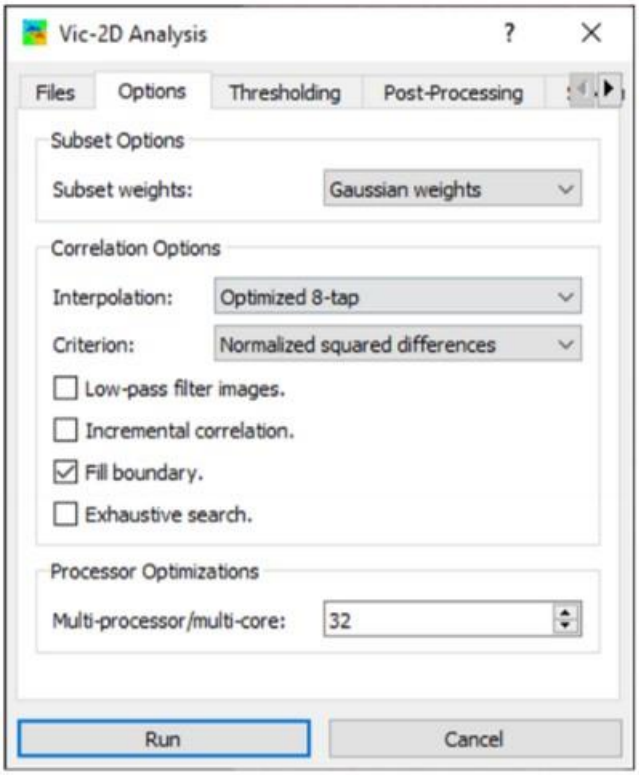

Figure 28: Analysis dialog options window – [39]

When high deformation is foreseen, an *incremental correlation* analysis is preferable: each image is compared to the previous image rather than the reference image, as in the case of DCB and ENF tests.

Once the full-field displacement is analysed, the strain computation is the subsequent step. The more practical technique for strain estimation is the pointwise local least-squares fitting

technique, experienced by Pan et al. [44] to solve the problem related to the calculation of the strains for the points located at the image boundary, hole, cracks and other discontinuity area.

The strain calculation window is chosen small enough to approximate the displacement distribution as linear plane and through polynomial functions of first order with coefficients to be determined by the least-squares method. However, it is quite important to note that, to obtain reasonable and accurate full-field strain estimation, the accuracy of displacement fields by DIC as well as a correct size of the local strain calculation window have to be assured. For homogeneous deformation, a large strain calculation window is preferred.

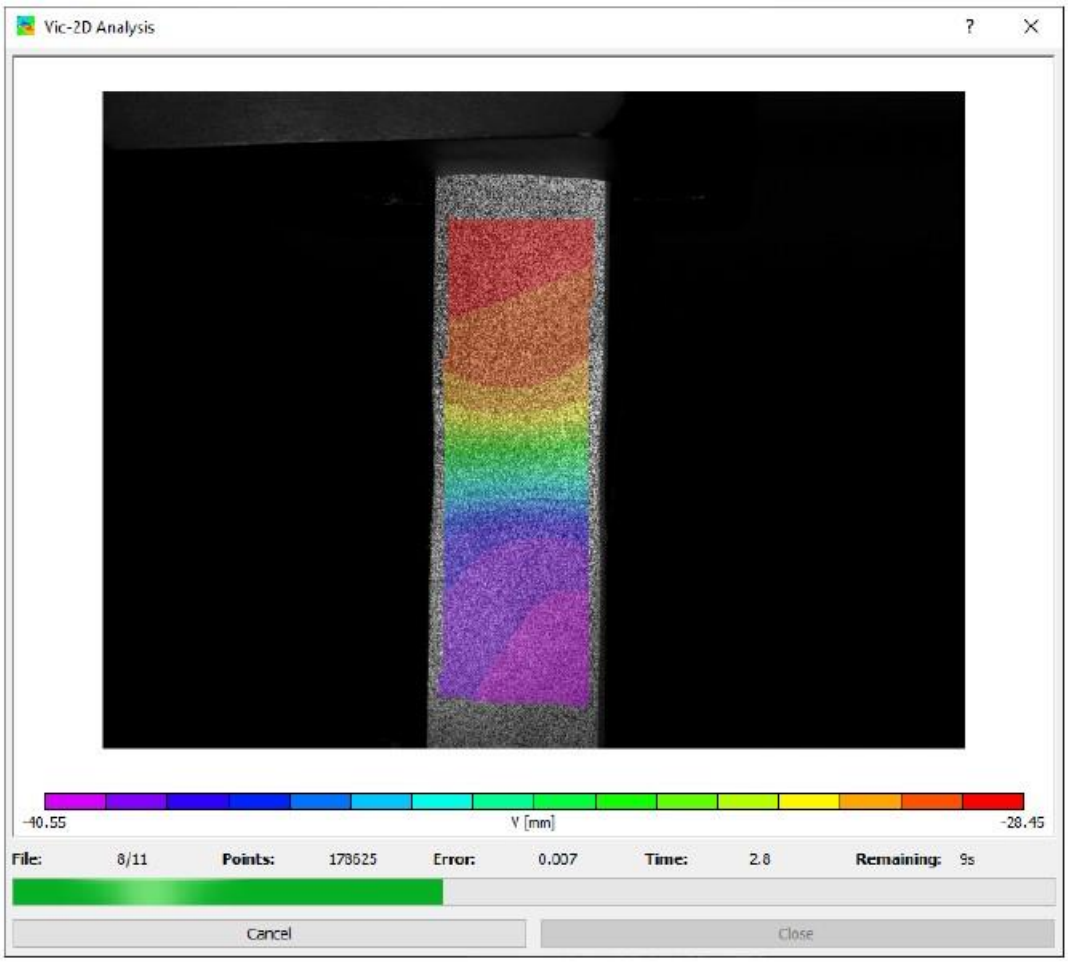

Figure 29: Analysis progress window during correlation running – [39]

The output of VIC-2D can be exported in multiple formats, i.e. *Matlab .m* file, for easy analysis and further post-processing. Every frame will have a related *.mat* workspace file containing the exported variables, for each subset into which it has been divided: each file is an array where

each entry corresponds to a subset. The output variables are initial positions in pixels and in *mm* of the subsets, their displacements in both units as well as stress and strain results computed.

Last but not least, the σ correlation parameter is obtained. It is exploited to track the crack growth, in case of DCB and ENF tests under study, and asses to the reliability of the correlation between subsequent images: an extension of the crack between two frames will lead to a lack of correlation between them and so an increase in σ parameter. According to this, it is also important to set an adequate sigma threshold value as did by Murray et al. [15] with the consequence in crack monitoring shown in the following figure. The subsets outside the speckled area are lost after the first frame: to assure this output, the σ parameter is set to -1 by default, in this case.

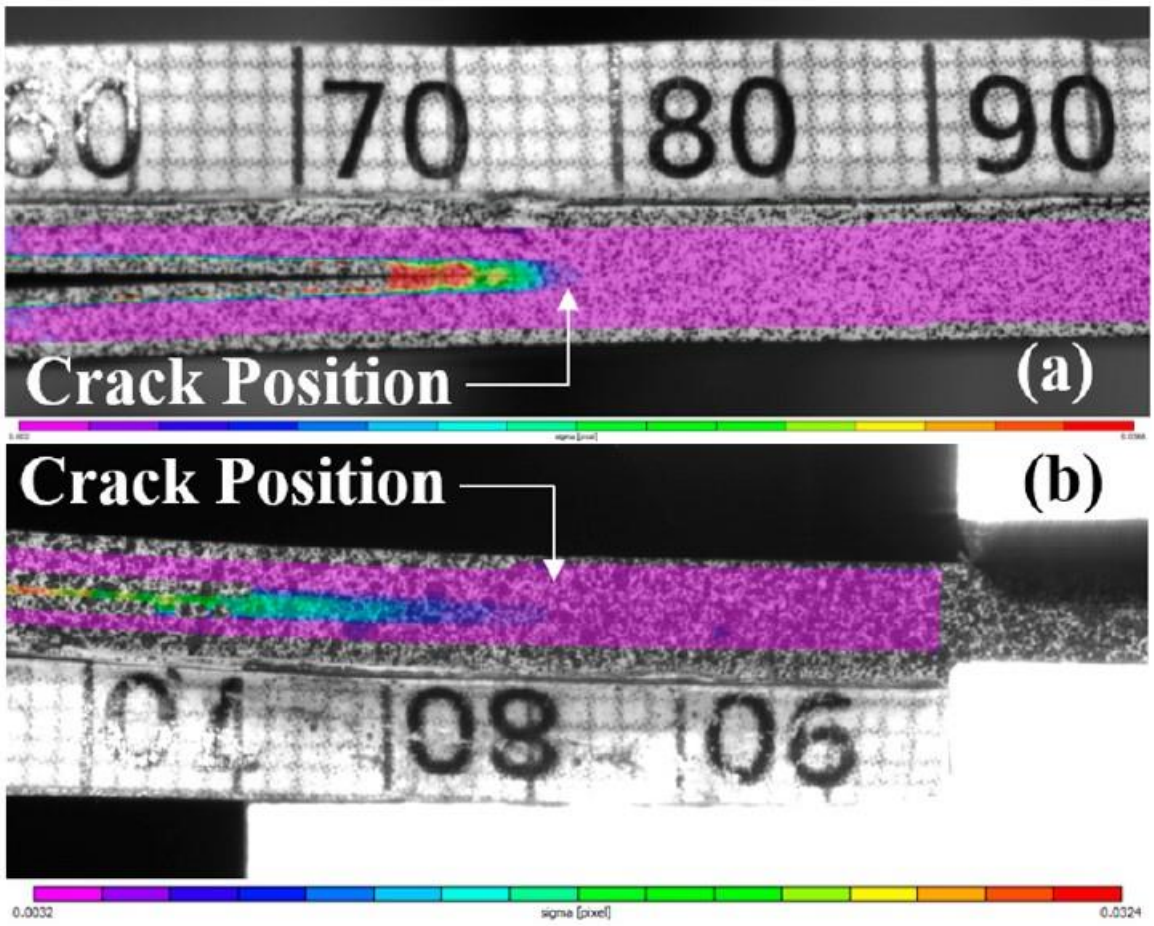

Figure 30: Crack front monitoring in (a) mode I and (b) mode II loading configuration: sigma coloured map is used to define the crack front position – [15]

1.6.2. 3D-DIC Stereo correlation

3D coordinate measurements of the surface require a minimum of two cameras that keep a defined angle in between them, called *stereo-angle*, to perform 3D photogrammetry in addition to image correlation. This takes the name of stereo-DIC or 3D-DIC, not to be confused with volumetric-DIC.

The stereoscopic system involve two cameras at defined distance from the specimen to be tested and with a certain angle between them, capturing the same region of interest. The DIC algorithms are employed to obtain the matching among subset in all over the captured images, both for reference-deformed images and for first camera and second camera.

For each deformed shape, the subset correlation between camera 1 and camera 2 allows to rebuild the three dimensional displacement of a certain point (represented by the subset), thanks to the triangulation mechanism. This works only if the relative distance cameras and specimen is set, necessary condition for the triangulation operation.

A pinhole camera performs a perspective projection thus transforming a 3D object point into a 2D image-point, thereby removing the third dimension in an irreversible manner, as shown in *Figure 31*. [38]

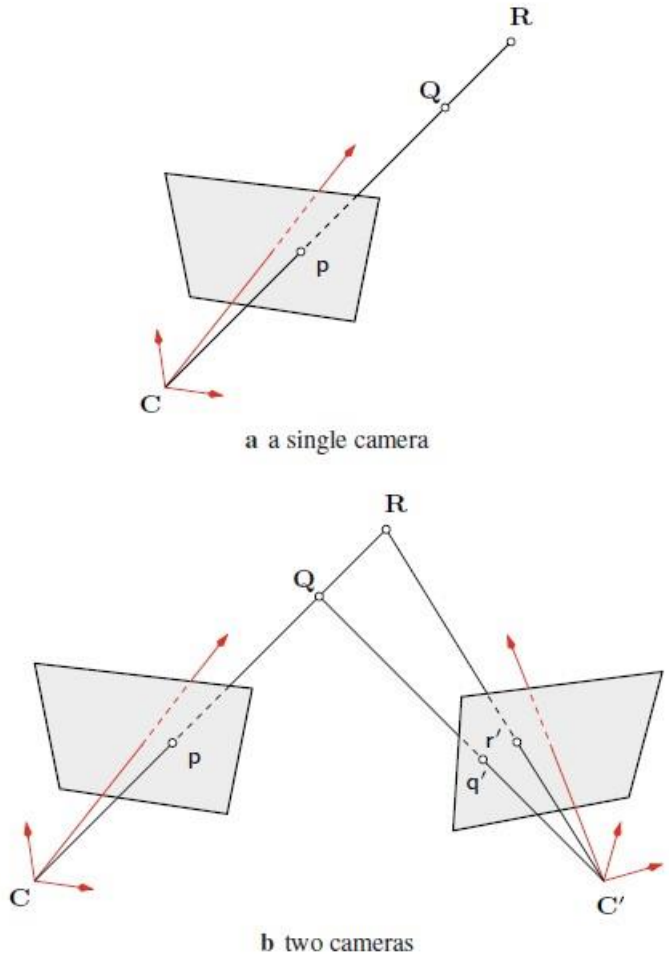

Figure 31: Single camera and two cameras image acquisition functioning – [38]

A Two 3D points, Q and R, are imaged onto the same image-point *p* as they are lying on the same projective ray (C, *p*), so that exists an infinity of 3D points belong to the image point *p*. Three-dimensional position of the object points is possible to be recovered by using the two cameras to record simultaneous image points of the same object (*stereo matching* function). If two image points are (*p*, *q'*), then the unique 3D point is *Q* while if the corresponding image points are (*p*, *r'*), then the unique 3D points is *R*.

The configuration of the two cameras is achieved by means of a calibration procedure that still works through images acquisition with both cameras but by using a target, a *calibrated target*. Target choice is driven by the specimen and relative speckle dimensions: each target differs for total number of spots and their relative distance.

Geometry and dimension of the target not only permit to compensate any optical distortion but also to obtain relative distance between the two cameras, their orientation in space with respect to each other and to the test sample, and assure a suitable conversion from pixel to millimetre.

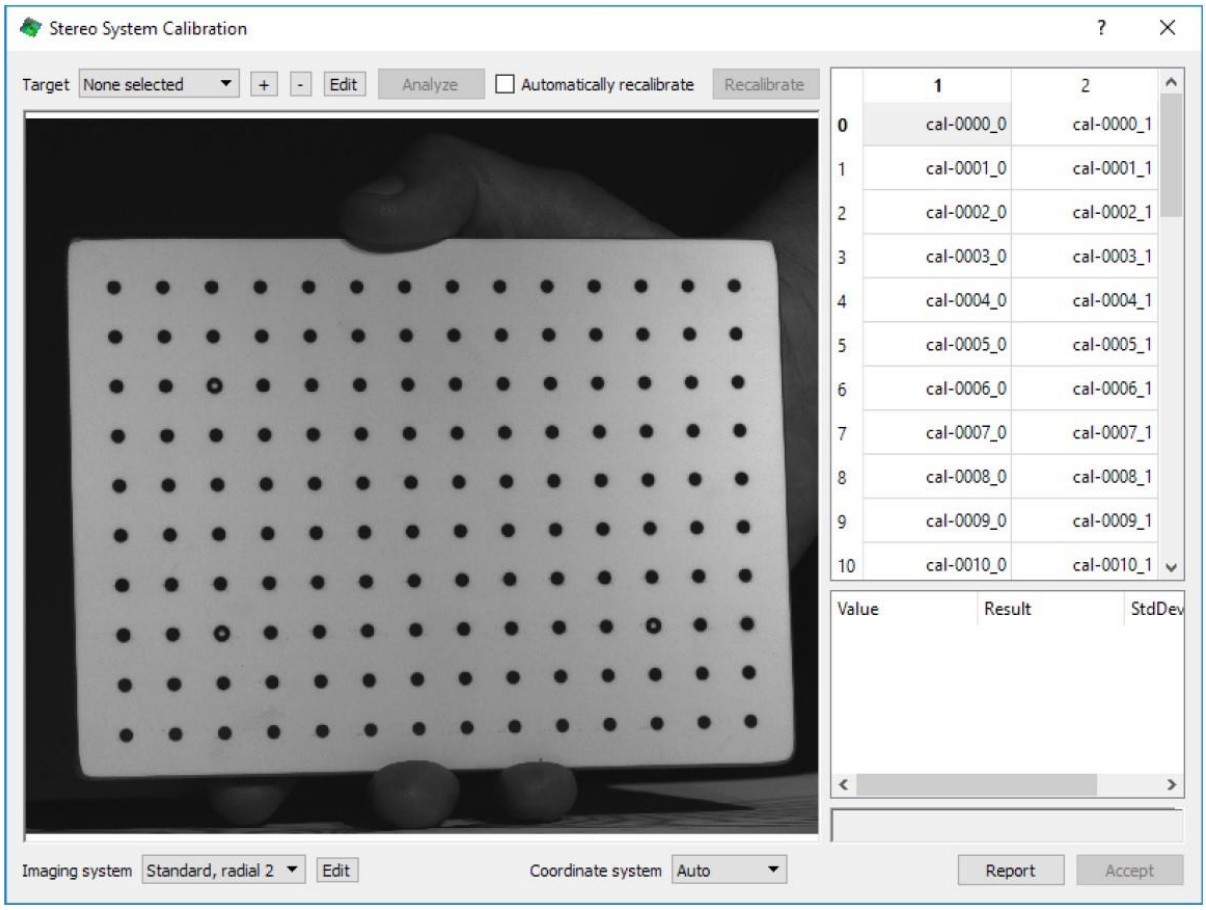

Figure 32: Calibration target for stereo calibration – [39]

Once the calculation is complete, a report of calibration results and error scores will be presented. The errors are related to each image acquired and the average error has to be kept less than 0.05. The average error (in pixel) is the error between the position where a target point was found in the image, and the theoretical position where the mathematical calibration model places the point.

2. Testing

The purpose of this study is to investigate the effects of plasma treatments on the adhesion between carbon fiber fabrics and epoxy resin as well as the mechanical behaviour of the resultant components. In particular it is useful to asses the effectiveness of different gas used for the plasma treatment in terms of composite damage resistance, with respect the untreated ones. The correlation between the delamination resistance of CFRP and surface modification provided by the plasma was assessed through DCB test and ENF test analysis with a proper chemical surface analysis made on the carbon fiber fabrics treated before the infusion process.

It is also used as novel investigation, the usage of DIC analysis for the onset of crack propagation during the mechanical test.

2.1. Materials and methods

The carbon fiber fabrics used in this study are provided by *Easy Composites* © with the commercial name *210g ProFinish 3k Carbon Fibre Cloth (1000mm)*. [45] These fabrics are used to create the CFRP with epoxy resin and and an epoxy resin with 31% of bio content IB2 (EasyComposite, UK). The bio-content of the bio-based resin is due to the glycerol, plant derived, in place of petroleum-based propylene. The bio resins present mechanical properties that are reported in *Table 1*.

	IB2
Tensile strength [MPa]	65,0
Flexural strength [MPa]	107,0
Flexural modulus [GPa]	2,8
Elongation at Break [%]	5,3

Table 1: IB2 resin properties

These fabrics are developed specifically to address the practical problems of trying to create cosmetically and aesthetically perfect carbon fibre parts when working with a delicate dry fabric

like 2/2 twill. It has been partially impregnated with a resin binder on the reverse side to assure the alignment of the weave during handling and positioning in the mould in the fabrication process as well as to facilitate the cutting and joining with perfect, sharp cut-lines typical experienced in prepreg parts. To assure the presence of this binder on one side, specific surface characterization method will be carried out. Typical sizing and release agents residual are usually detected by several characterization methods to distinguish the effect of the plasma treatment in terms of grafted functional groups from the particles already present in the materials due to fabrication process.

Plasma ablation is used as an alternative to pre-cleaning with chemicals even if to increase bonding properties especially in composites joining with resins, chemical pre-polishing is usually adopted before introducing plasma action. Kim et al.[30] washed CFRP samples with isopropyl alcohol (*IPA*) for 5 min with an ultrasonic cleaner to remove dusts and chemical contamination on the surface, then dried using compressed air and subsequently plasma treated.

ProFinish ™ is also a suitable choice for resin infusion projects where the ability to make neat cut lines in the material means that is possible to obtain a finish similar to the prepreg parts used for the same fabrication process, that is the one adopted in this thesis work. Adjustment and repositioning of the fabric in the mould is also easier to achieve and much less likely to distort the material. The specification and main properties of the fiber fabric are listed in the *Table 2*.

Weave	2 x 2 Twill	[-]
Areal Weight	210	g/m^2
Thickness	0.33	mm
Filament Diameter	7	µm
Tensile Strength	4120	MPa
Elongation at Break	1.8	%
Tensile Modulus	240	GPa
Density	1.79	g/cm^2

Table 2: Specification of carbon fiber fabric adopted

The carbon fiber fabrics are initially cut in panels 25x25 cm, slightly higher with respect to the final dimension of the panels that has to be put inside the vacuum bag to assure the fabrication of 2-4 specimens for each plasma process gas chosen, both for DCB and for ENF test.

Panels of this encumbrance assure the success of the treatment, with the plasma equipment adopted in the lab, described in the chapter 2.1.1., compatibly with the maximum dimensions of the 3-axis robot that manoeuvres the torch itself.

The equipment adopted as well as the fabrication methods are explained in details in the following chapters, from the plasma apparatus used for the activation of carbon fiber fabrics before the vacuum infusion to the DCB and ENF test machines.

2.1.1. Plasma treatment apparatus and plasma process

For plasma treatment, atmospheric pressure plasma treatment equipment through the adoption of a plasma jet system from *Plasmatreat GmbH* (Steinhagen, Germany) was used as shown in *Figure 33*.

The plasma comes out of the jet torch and it get in contact with the surrounding air along the distance between the source and the specimen to be treated. Several attempts to figure out the best distance jet-sample were carried out according to the plasma focus interception of the specimen and the influence of the surrounding working space.

Figure 33: AP Plasma treatment equipment: (left) Openair ® plasma generator, (middle) generator and Power Control Unit with cables, (right) Plasma Jet Source – [28]

Figure 34: Test bench for plasma treatment

Plasma treatment test bench used for the carbon fiber fabrics treatment was structured on two different levels of 75 x 200 cm with a height of the lower desk 25 cm and the upper desk 87 cm.

It is composed of nine parts: one generator, two transformers or Power Control Unit (*PCU*), two plasma jet sources, one plasma polymerization unit *PDA 1*, one PC that manages the process parameters with a proper user graphic interface, one 3-axis movement system and one extractor hood.

The generator is the *FG5001* and it is integrated compactly under the desk. It generates constant tension with supply voltage of 100-240 V and it is equipped with modern *IGBT* semiconductor final stages and combines very high performance with precise plasma power regulation and control functions. During the surface activation and ablation process, 100% of reference voltage is used with resultant minimum electrical pulsation that assure a stable discharge as well as 25 kHz – 15 A to obtain a workable plasma compatible with the substrate that has to be treated. Up to two plasma nozzles can be operated with the *FG5001* plasma generator but for the purpose of this study, just one plasma jet nozzle is used.

PCU is used for the various monitoring modules: Plasma Power Module (*PPM*) that registers power and tension levels directly on the jet head, Light Control Module (*LCM*), Flux Control Module (*FCM*) that adapts continuously the gas flow rate at the various exercise conditions, Pressure Control Module (*PCM*) and Rotation Control Module (*RCM*). *PCU* is powered by a gas flux of 20-60 l/sec.

Plasma Jet adopted is the *PFW1004* system and the rotative nozzle is the *RD1004* series is used to generate the cold plasma. The rotative nozzle is used to achieve an uniform distribution of plasma effect upon the sample surface and this choice is justified by previous studies made on similar treated components which proved to be chemically effective. Pressure of gas ejected is around 4 bar and the temperature depends on the nozzle chosen but they vary between 40-190 °C.

The 3-axis movement system is the *Janome JR3000* Series and it counts for a *PAD* controller, Start and Emergency Stop system and the movement structure. The PAD is used to adjust and insert the coordinates of the robot with respect to the sample to be treated which is placed on a mobile base (along x-y direction). The other coordinate, z axis, is crucial because its setting determines the right sample exposure to the plasma jet. The x axis is set in such a way as to obtain a non-excessive overlapping area for consecutive passes (compatibly with the opening of the plasma conical beam), so as not to overtreat the surface exposed to the plasma, risking the deterioration of the fabric and excessive overheating.

It was performed a preliminary surface chemical characterization of the treated and untreated samples in order to define the most suitable process gas and process parameters (jet-sample distance, torch jet speed and exposure time) and the prototype sample is shown in *Figure 35*.

From these characterization, both nitrogen and N_2H_2 resulted to be equally effective process gas in order to increase the amount of oxygen and functional groups useful to enhance the epoxy resin adhesion with the carbon fiber fabrics.

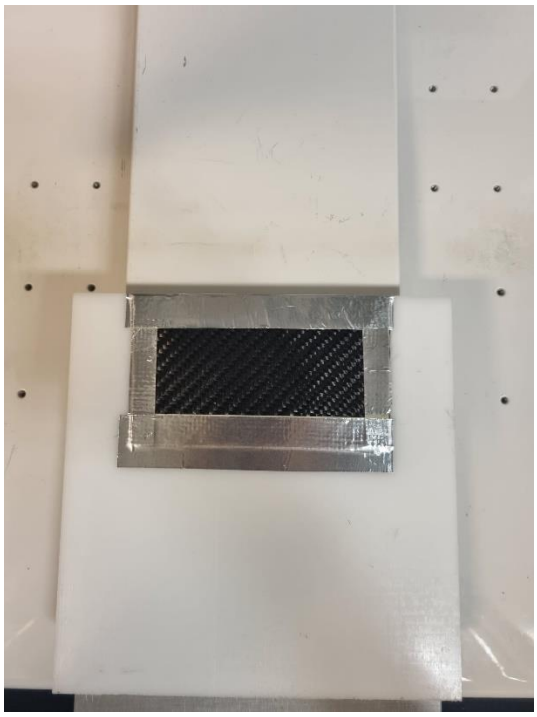

Figure 35: Sample plasma treated for surface characterization

Once the characterization has been ended, the process parameters were chosen listed in the *Table 3*.

Process Gas	Power [W]	Distance jet-sample [mm]	Jet speed [mm/s]	Gas flow rate [l/min]	Reference voltage [%]	Plasma voltage [V]	Plasma intensity/frequency [kHz]
N2	660	12	25	31	100	334	25
N_2H_2	810	16	25	31	100	334	25

Table 3: process parameters for plasma treatments

The treated part of the surface acquires some brightness as the main evidence that helps to distinguish it from the untreated part as shown in *Figure 36*.

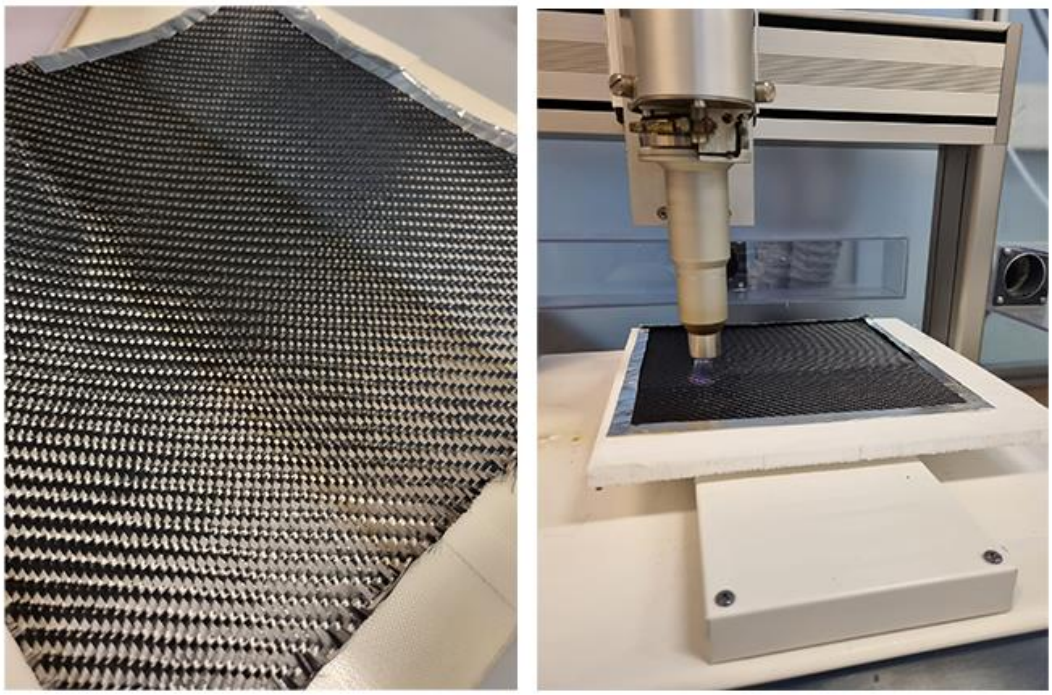

Figure 36: (left) Evidence of treatment on the trial sample, (right) carbon fiber fabric treatment using N2H2 gas

Once the treatment was completed, all the specimens were transferred to the composite materials laboratory at the *Politecnico di Torino* after preliminary organization of the vacuum infusion bench in order to carry out the manufacturing process as soon as possible while maintaining the positive effects of the surface treatment. The waiting times between treatments and the manufacture of CFRP composites are not so restrictive since the effect of a plasma treatment of similar magnitude ensures a chemical-physical surface modification from 14 to 20 days after treatment. Nonetheless, it was preferred not to wait more than a day for the vacuum infusion process.

2.1.2. Surface characterization results

Once the surface treatment process was completed, it was necessary to carry out a chemical analysis of the treated components to be sure of the effectiveness of the gas chosen and the subsequent chemical mixing and grafting of surface functional groups useful for the purpose. For this reason, both the characterization by Raman spectroscopy and ATR was carried out using instrumentation offered by the Università del Piemonte Orientale in Alessandria (TO).

Raman spectroscopy was performed using a *Micro Raman – LabRAM HR* Evolution machine (*Horiba Jobin Yvon GmbH*) with a green laser source (532 nm) and micro-optical zoom 80x. Its high throughput allows measurements to be obtained in just few seconds or minutes but the right acquisition is assured by the absence of relative motion between the sample and the optical lens with laser source incorporated hence long exposure assure the complete and reliable result, if the component is fixed properly.

Stokes and anti-Stokes spectral features can be simultaneously measured, providing additional information to the user. They represent anelastic diffusion of the incident light with slightly energy acquisition or gave up, from the interaction with molecule: the band shifted to higher wavenumbers are called anti-Stokes Raman bands and those shifted to lower wavenumbers are called Stokes Raman bands, whose intensity are more intense and therefore used for qualitative and quantitative analysis. The spectral range is between 4000-100 cm^{-1} even if this machine allows measurement in the sub-100 cm^{-1} with measurement below <10 cm^{-1} routine available. [46]

Figure 37: Micro Raman spectrometer machine – Horiba Jobin Yvon LabRAM HR Evolution

The machine used for the ATR spectroscopy is provided by Shimadzu GmbH and model is "*IR Spirit*", as shown in *Figure 38*.

The prism that enters in contact with the sample to be characterized, is made of diamond so the measurement wavenumber range is up to 400 cm-1 (wide-band). It is necessary to clamp the sample closely against the prism surface before the measurement on the sample surface. To be

sure about the difference between one side treated and the other side not directly treated, both sides were analysed paying attention to put the prism in contact with the fibers and not in proximity of the empty space inter-fibers.

Figure 38: ATR spectroscopy machine – Shimadzu IR Spirit

Before the last characterizations, preliminary analysis with Micro-Raman was carried out as anticipated in the previous chapter.

The preliminary process parameters were different from those adopted for the final treatments in terms of jet-fabric distance and plasma beam overlap area. The N_2H_2 specimen was placed at a distance of 15 mm from the nozzle with a torch pitch for both processes (N_2 and N_2H_2) set to 10 mm. This parameter allowed to obtain an overlap area of about 50%. These choices were aimed at intercepting the primary plasma beam, which was received by the fabric at the relative distance set as previously suggested.

Before proceeding with the deconvolutions of curves G and D1, the following peculiarities were noted:

- NT specimen returned peaks of the G order band not as high as expected, probably due to the shielding effect of the primer placed on the surface used to improve the handling conditions of the fabric and to avoid defibration;
- the specimen treated with N_2 showed peaks in the area between 300-500 cm^{-1} typical of the -COOH functional groups of polyamides and could be a good suggestion for the

presence of nitrogen traces; the obtained G peak was lower, showing a lower order band level, and shifted to a lower wavenumber as expected;

- the N_2H_2 specimen showed intermediate results between those returned by the NT and N_2 specimen.

Once this first analysis was done, it was decided to modify some process parameters: distance jet – sample for N_2H_2 process was changed from 15 mm to 16 mm to have a better chance to intercept the primary plasma focus, and the overlapping area was reduced increasing the jet path width from 10 to 12 mm. The other parameters remained the ones showed in the table before.

The ATR characterization has been performed on three different samples: untreated, N_2 plasma treated and N_2H_2 plasma treated sample. Slight differences between the three were observed but enough to assure the possible benefits to the aim of the work, as shown below. In particular several different points of observation were analysed in order to differentiate the results locally on both sides.

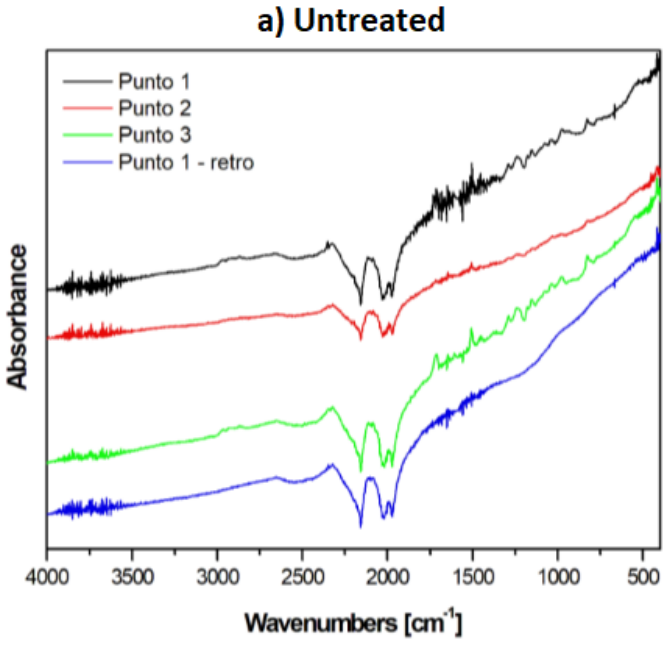

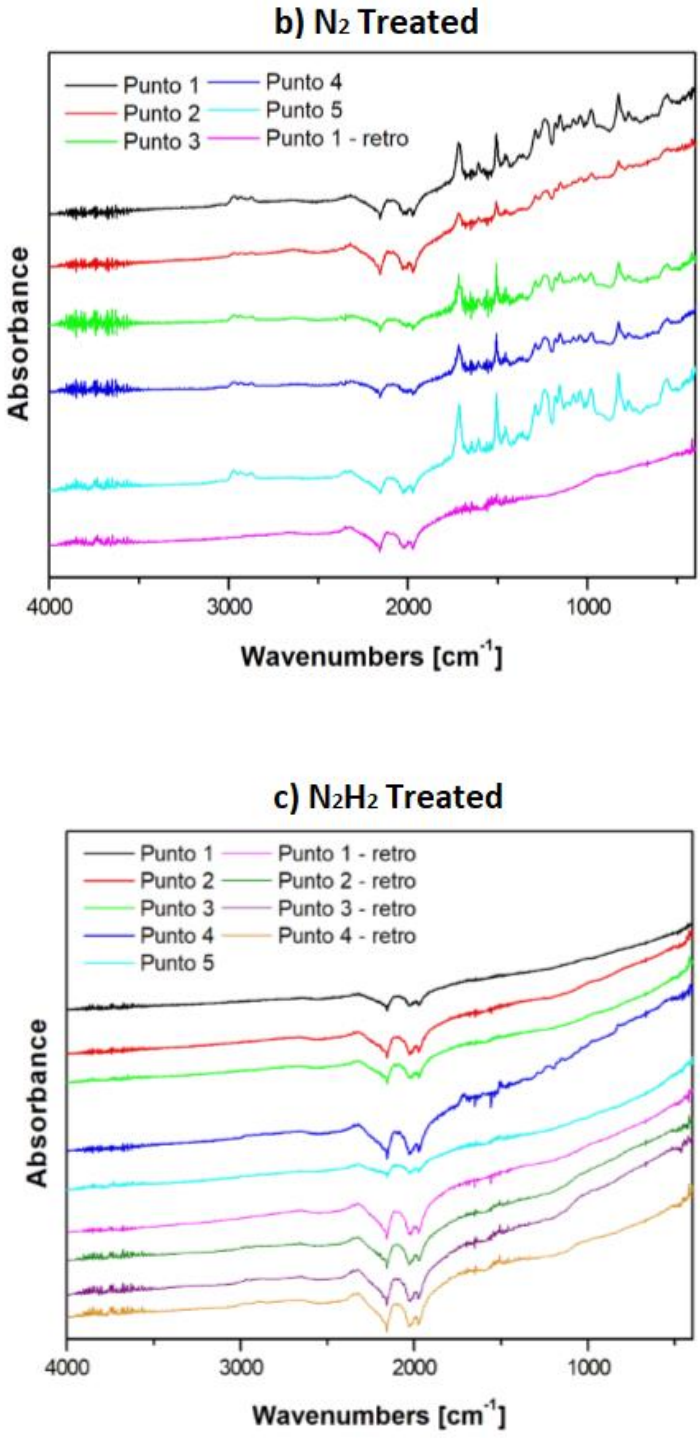

Figure 39: ATR spectra: (a) untreated fabric, (b) N2 plasma treated fabric, and (c) N_2H_2 plasma treated fabric

Around 2000-2300 cm^{-1} of the spectrum, a trace of a substance was detected whose peak decreased after both plasma treatments: through a research of the instrument database it was possible to trace the chemical nature of the component whose spectral trace is shown in *Figure*

40. It highlighted the presence of an unsaturated polyester, *poly (4 4-dipropoxy-2 2-diphenylpropane fumarate)*, more evident in the spectrum of the component treated with N_2 gas. This polyester, obtained from fumaric acid, is used as resin binder bisphenol A-based thermoplastic polyester. It is common adopted in glass fiber composite to increase the interlaminar fracture toughness but with a very precise amount, vice versa it is detrimental from the point of view of mechanical resistance of the final composite. [47]

On the other hand, it could also be a trace of a primer, whose properties are significantly less beneficial unlike the latter case presented above.

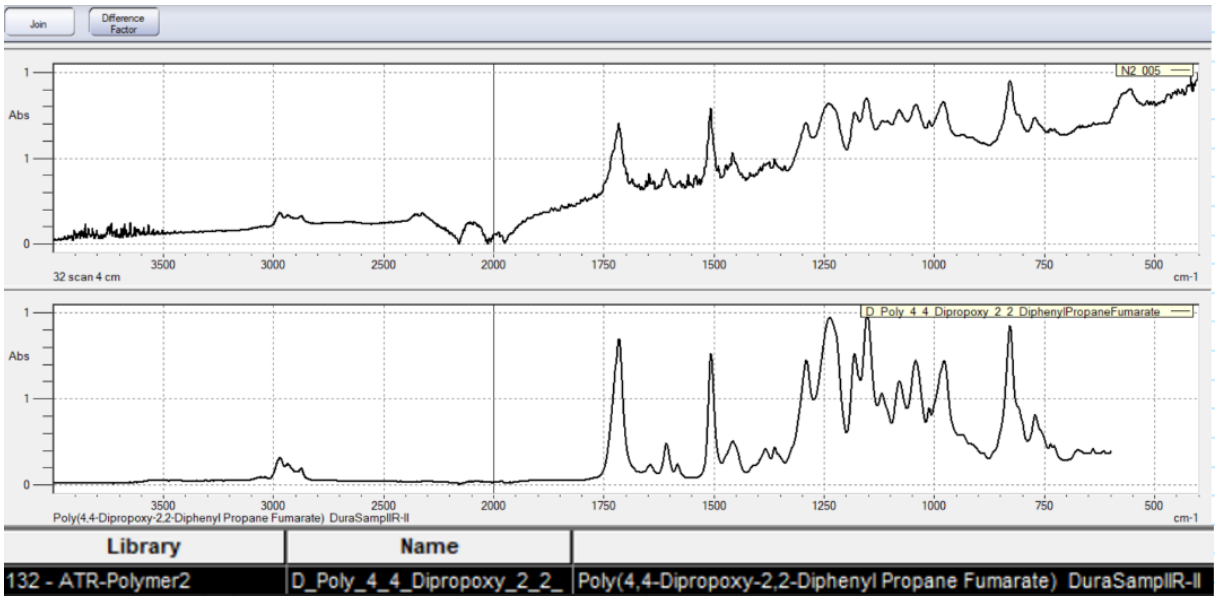

Figure 40: ATR spectra of possible substance found on the surface – unsaturated polyester

Further differences are also observed in the vicinity of 3000 cm^{-1}, especially in the case of N_2. This wavenumber value and its surroundings are characteristic of -OH hydroxyl chemical bonds and NH groups, which is a further confirmation of the success of the treatment. In the vicinity of 1700 cm^{-1}, an area identified by the presence of the carboxyl group is particularly influential in the case of chemical interaction with the nitrogenous groups of the epoxy resin adopted; furthermore the double bonds C=C whose typical wavenumber is around 1650 cm^{-1} seems to have undergone different variations for the two treatments, potentially having received an ablative effect in one case while in the other, the treatment would seem to have acted directly on the heart of the structure, "damaging" the polymer. This evidence was subsequently investigated by analysing carbon order and disorder bands, using Raman spectroscopy.

As main reference for the carbonaceous spectra that fits better with this characterization results, the following band has been considered, according to what declared Croce et al. [48].

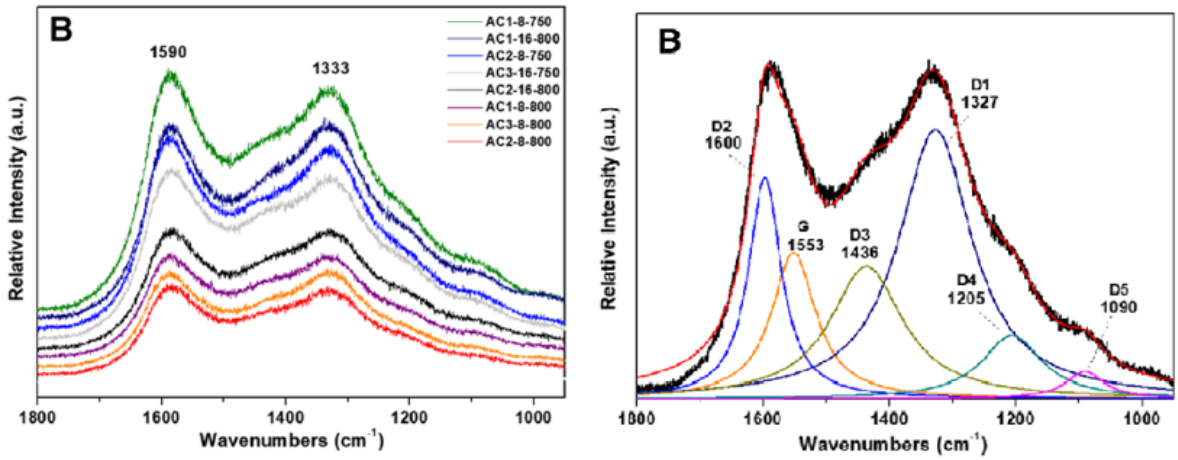

Figure 41: (left) Raman spectra obtained on Activated Carbon sample by 532 nm laser source, and (right) spectrum fitting of one sample AC through deconvolution process – [48]

As it possible to see in *Figure 41*, the D1 band is placed at about 1330 cm^{-1} and it is due to defective sp^3 carbon and the intensity and position of this band depend on the presence of amorphous regions in the carbon materials. Conversely, the intensity of bands at 1550-1590 cm^{-1}, called G band, is related to the extension of ordered regions, as explained in 1.3.3. chapter.

To asses the result of the surface treatment, $R_1 = \frac{I_D}{I_G}$ ratio is studied for the three different samples: small value of R_1 indicate that the material has not been massively affected by the surface treatment maintaining a certain degree of order or that a cleaning of the possible primer has been recorded, allowing the fibers to appear more easily on the surface layer, ready to bind mechanically and chemically to the resin used for the manufacture of the final composite.

D1 intensity, G intensity and R_1 ratio are shown in *Table 4* and deconvolution of peaks was carried out to show the precise location D1 and G peaks as well as D2, D3 and D5.

	D1 Intensity	G Intensity	R_1 ratio
Untreated point 1	733.97	595.32	1.24
Untreated point 2	563.77	384.32	1.47
Untreated point 3	490.59	341.92	**1.43**
Untreated point 4	1104.17	868.05	1.27
Untreated point 5	1307.71	1023.08	1.28
N2 treated point 1	205.33	113.64	1.81
N2 treated point 2	58.40	42.25	1.29
N2 treated point 3	68.63	41.42	1.66
N2 treated point 4	124.46	101.21	1.23
N2 treated point 5	136.05	99.25	**1.37**
N_2H_2 treated point 1	119.99	73.12	1.64
N_2H_2 treated point 2	85.10	53.33	1.60
N_2H_2 treated point 3	91.82	59.10	**1.55**
N_2H_2 treated point 4	82.31	53.44	1.54
N_2H_2 treated point 5	89.27	83.98	1.06
N_2H_2 treated point 6	121.13	78.02	1.55

Table 4: Raman deconvolution values of D1 and G peaks, and R1 ratios for untreated, N_2 plasma treated and N_2H_2 plasma treated samples

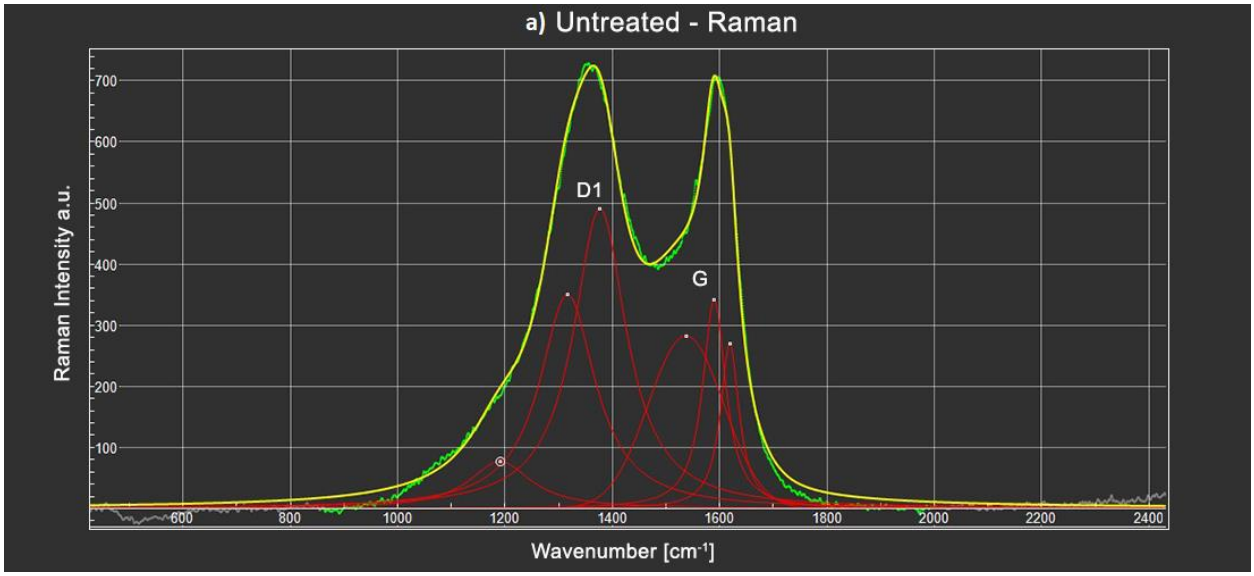
a) Untreated - Raman
Raman Intensity a.u.
Wavenumber [cm-1]
D1
G

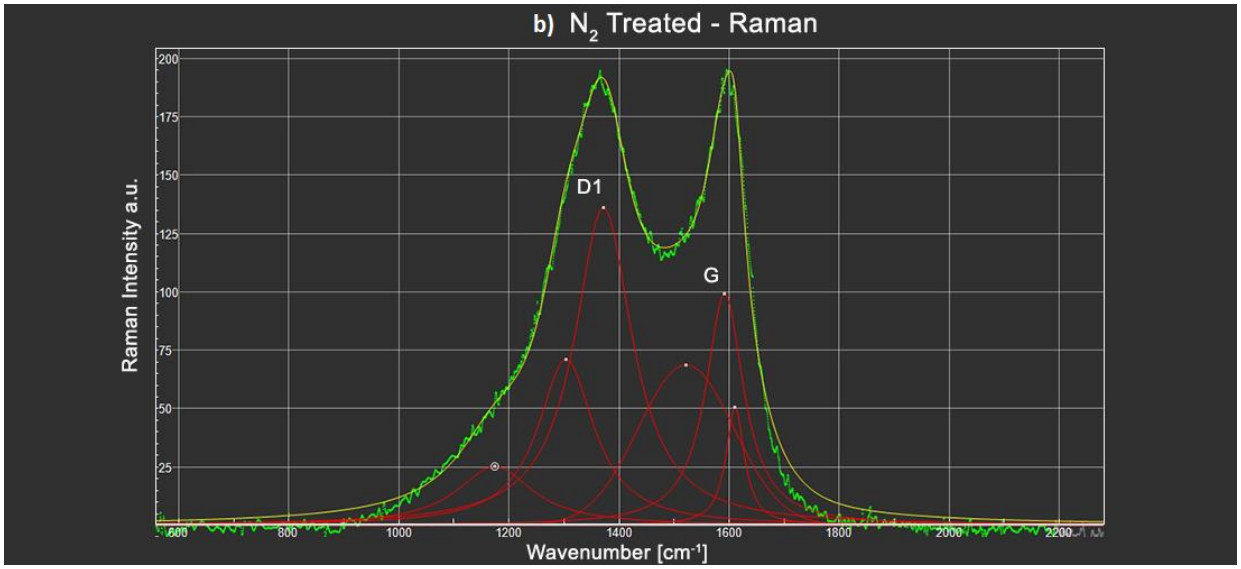
b) N2 Treated - Raman
Raman Intensity a.u.
Wavenumber [cm-1]
D1
G

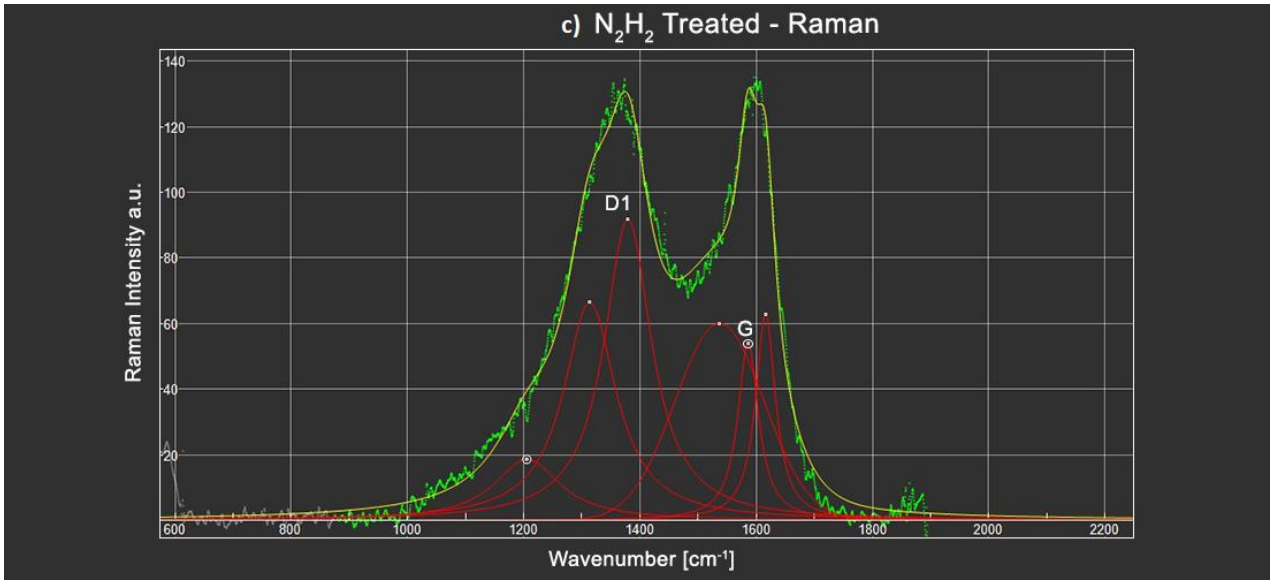

Figure 42: Raman spectra deconvolution of G and D1 bands: (a) untreated, (b) N2 treated and (c) N2H2 sample

The results are highly sensitive to the calibration of the instrument, to the correct positioning of the sample next to the laser source as well as the high photon energy that may cause sample damage. Data that deviate significantly from the average value acquired may be the result of problems encountered of a similar nature to those just described above. Considering this aspect and the data collected, the R_1 ratios deemed identifying the component under examination have been highlighted in the table (R_{1_UN}=1.43, R_{1_N2}=1.37, R_{1_N2H2}=1.55), for the three different types. In particular, the peak values for D1 and G bands are pointed out in *Figure 42*, as red deconvolution curves' peaks. The R1 ratios obtained are in line with the results achieved for the preliminary analyses of the sacrificial tissue samples, treated with plasma according to the same methodology to obtain the correct process parameters.

The peak intensity gives information about the quantity of a specific compound and the peak shift can identify stress and strain states. Further information are collected from the change in peak width that reveals the degree of crystallinity. When a crystal is subjected to a collimated laser beam it reacts starting vibrating at an intensity depending on its bond strength and length. If a crystal is subjected to a tensile stress, we can envision the atoms being pulled apart, or chemical bonds lengthened, relative to their normal positions and lengths in a unstressed crystal. As the chemical bond length increases, and the force constant remains the same (in Raman, the laser source acts constantly with same intensity and wavelength), we should expect the vibrational frequency to decrease. A shift of the Raman peak position to lower frequencies is

exactly what is observed from materials that have been subjected to a tensile stress. Conversely, if a compressive stress is applied, we would expect to be shortened, relative to their normal positions and lengths in an unstressed crystal. The compressive strain in the crystal results in Raman peak positions shifted to higher frequencies. The same consequences are achieved in presence of strong chemical bond, with relative shorter molecules distance that appears closer to each other. [49]

As it possible to observe in the images above, change in peak positions and peak widths were registered after plasma treatment. For the formers, the variations recorded for the three different typologies of characterized specimens, relative to the average data obtained, are summarized in *Table 5*.

Peak Shift	D1 [cm^{-1}]	G [cm^{-1}]	D1 - Shift	G - Shift
NT	1376,9	1589,9		
N_2	1371,7	1592,0		
NT → N_2			-5,20	+2,07
NT	1376,9	1589,9		
N_2H_2	1379,3	1586,1		
NT → N_2H_2			+2,43	-3,80

Table 5: Peak shifts of band G and D1 after plasma treatment

Negative shifts were recorded for disorder band of N_2 plasma treated sample unlike the G band which suffered a upshifts; on the contrary, in the N_2H_2 case a downshift of the G band and a upshift of the D1 band was recorded, further confirming the response in terms of the R_1 ratio. Overall the level of disorder appears to be increased in the case of N_2H_2 treatment than in the case of surface treatment with nitrogen gas.

Possible conclusion or explanation of what both characterization gave are:

- N_2 acted on the chemical environment and less on the structure of the molecule which could be advantageous for increasing the adhesion characteristics and also for increasing or otherwise, maintaining the mechanical characteristics of the final composite. The ratio R_1 is the lowest which confers a higher degree of order, possibly due to the surface cleanliness of the substance (perhaps sizing) observed thanks to ATR spectroscopy.

- N_2H_2 instead seems to have acted directly on the core of the structure, breaking the polymer; from bibliographic researches, for similar components with the same plasma treatment, a higher percentage of Carbon was verified (*XPS* analysis) and the

appearance/increase of functional groups -*COOH*, π-π. The ratio R_1 is the greatest, confirming the down shift of the peak of G and also the edge effect, identified by the peak and wavelength of the secondary disorder band D5, is more pronounced than in the case of the sample treated with nitrogen . At the conclusion of these aspects it is expected either to have significantly damaged the structure or to have contributed to a clear improvement, to be verified with mechanical tests.

2.1.3. Material and specimen preparation

The laminated plates were produced 12 hours later the plasma treatment of the carbon fiber fabric samples (12 plies for each typology), at the Politecnico di Torino's mechanics laboratory (*DIMEAS* department). Fabrication process was done through vacuum bag infusion with manual hand lay-up of each carbon fiber plies. An example of the main elements used for this fabrication methods are shown in the *Figure 43*.

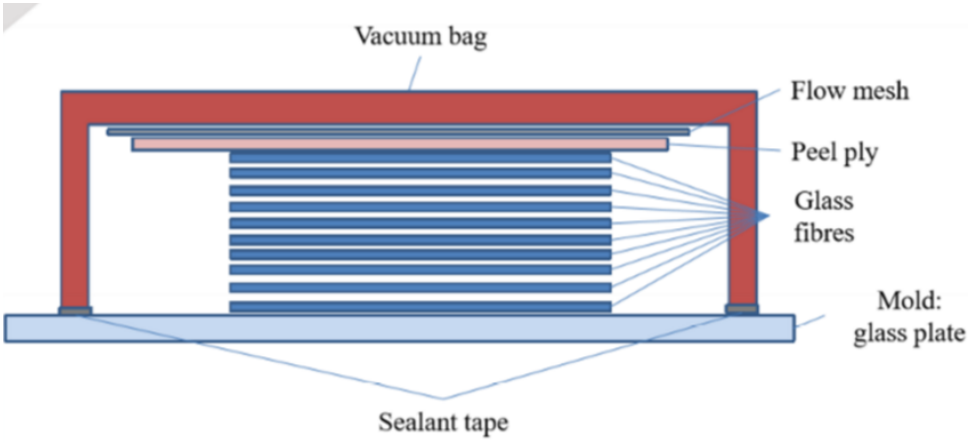

Figure 43: Example of vacuum bag infusion main elements – [18]

Glass plate is chosen as base for this process because it is difficult to bond hence we assure that the plies stuck on it and thanks to the application of a specific wax used as mold release, will not bond making difficult the debonding during the demoulding. At the extreme parts of the working area, sealant tapes were put in order to seal the plastic bag once the stuck sequence of fabrics were placed.

Carbon fiber fabrics are put one on the other with the same fiber orientation in our case (usually 90° is positioned as the same direction of the resin flow to minimize the flowing resistance while infusion is acting), with aluminized paper on the middle of the stuck sequence to perform

the precrack as explained in the 1.5.1. chapter. On the top of the last carbon fiber layer, a releasing woven fabric is positioned, the *peel ply*: made on nylon or polyester, it offers better surface finishing and good release without compromise the surface properties.

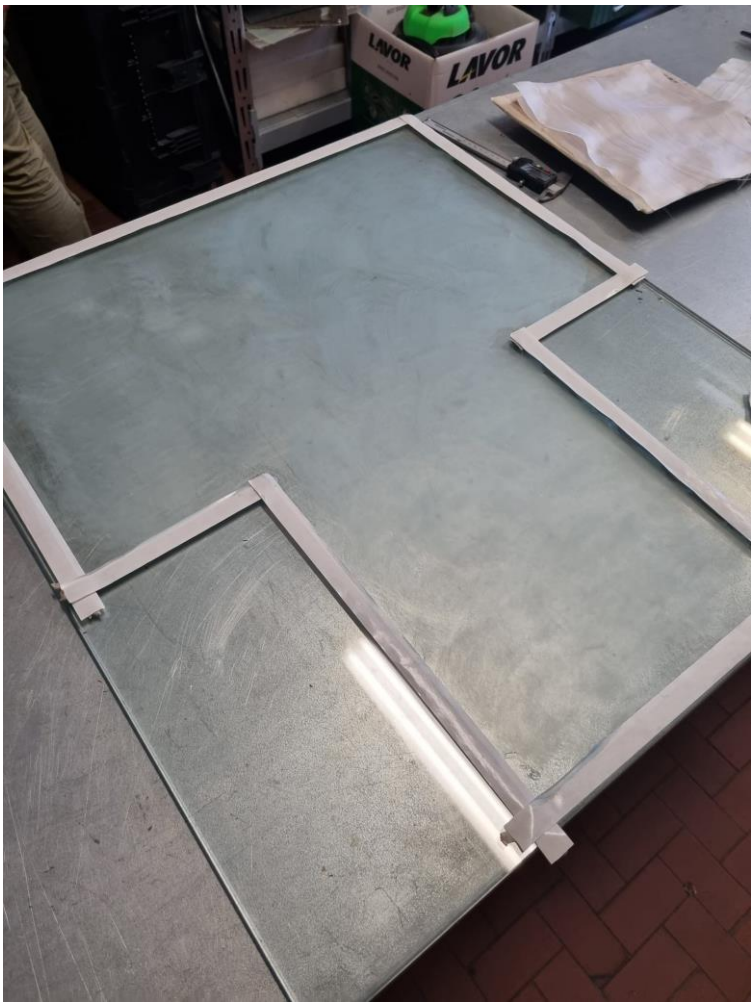

Figure 44: (up) mold release wax, (bottom) glass plate working area delimited by sealant tape

The next step involves the positioning of the flow mesh sheet, a warp knitted polypropylene net used to transport the resin at a certain speed as homogeneous and constant as possible, which must cover the entire work area. It allows to avoid any possible resin lock during the infusion. Once the flow mesh layer has been positioned, it is necessary to fix the corners with scotch tape, away from the points affected by the infusion path.

The homogeneity in covering the entire fusion area avoiding accumulation points is also guaranteed through the use of the spiral tube. Few segments are positioned at the inlet and outlet

of the infusion path, fixing them with special silicone connectors through which the channels for inserting the resin and for coupling with the vacuum pump will be placed.

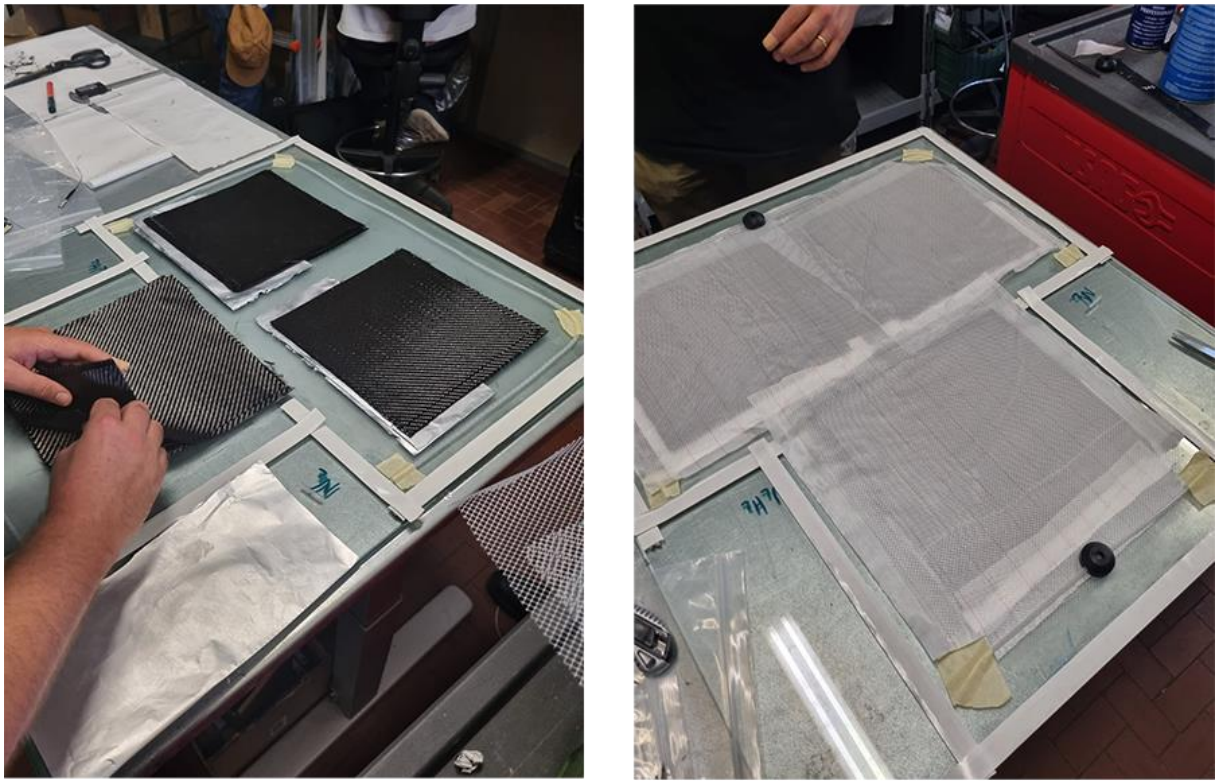

Figure 45: (left) Hand lay-up of carbon fiber fabrics plasma treated and untreated, and (right) positioning of peel ply, flow mesh sheet, spiral tube and silicon connectors

Plastic bag is put on the positioned stuck elements: it has to avoid all possible air leakage once it is successfully sealed with sealant tapes and vacuum is created inside the bag. The bag covers also the silicon connectors but with a cutter, a hole is made in order to insert the tubes for the resin and for the tube that connects the environment to the vacuum pump. High attention must be put on the sealing because every minimum presence of air will not allow to obtain a final composite with adequate characteristics (i.e .: uneven thickness, low resistance areas).

Clamps are used to fix the bag from its inlet and outlet connection once the vacuum is created but also used for check if that condition is achieved: it is enough to control the pump barometer after few minutes from the vacuum creation. If any leakages are found, it is possible to insert the resin.

In the main while, according to the pot life of the resin, mixing of the resin and hardener was made ready to further insert the mix inside the bag. Before this step, any air bubbles have to be

removed putting the resin container inside a vacuum chamber (a catch pot connected to the pump). The same catch pot is used to contain the resin the reaches the outlet silicon connector once the infusion approaches the ending. An empty container collects the outing resin inside the catch pot.

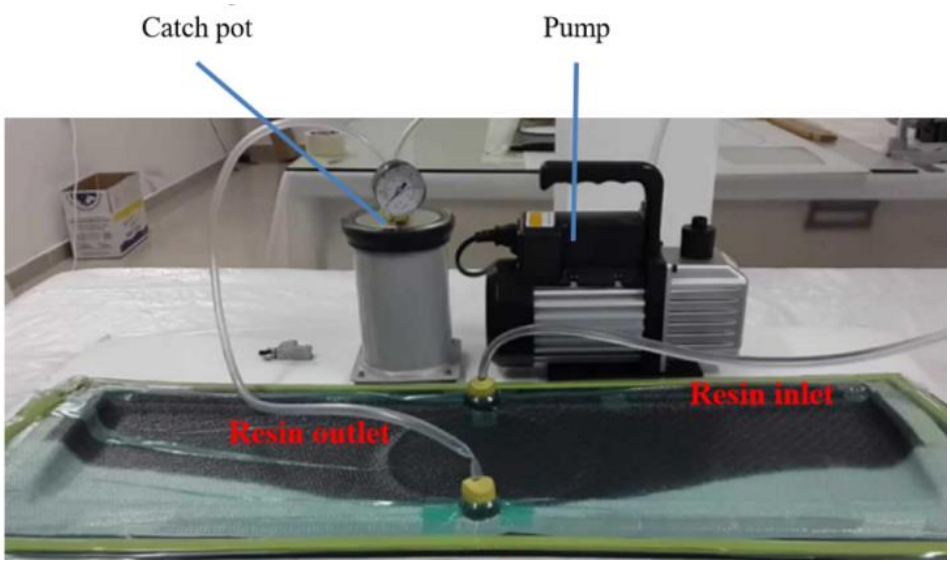

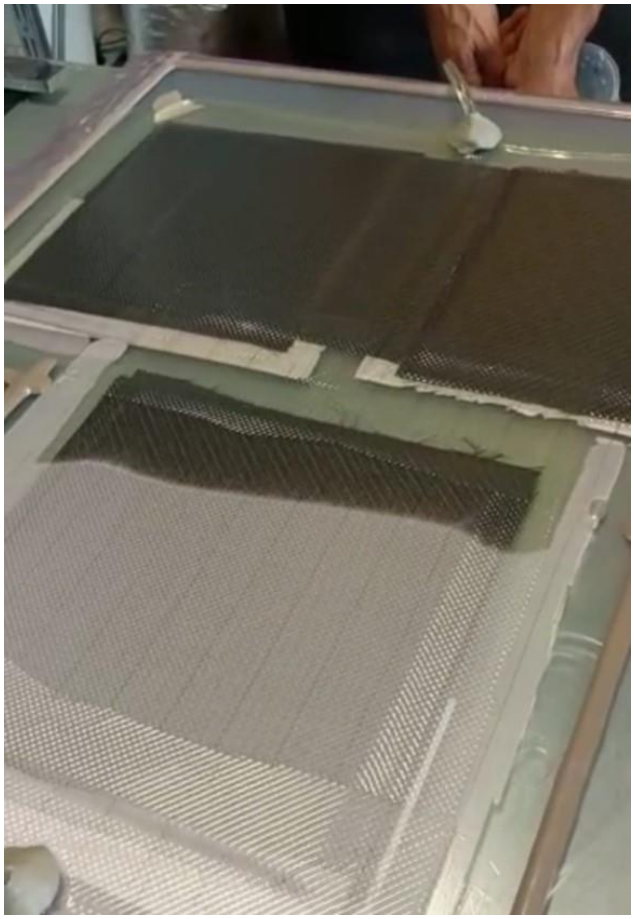

Figure 46: (up) vacuum and resin insertion equipment, (bottom) resin infusion path

When infusion is completed, the mould is left for 24 hours and then demoulding is conducted.

To obtain the final specimens to be used in DCB and ENF tests, a precise cut is required to asses the geometrical dimensions suggested by the standards. To achieve this result, a *110V/60Hz Wazer – Desktop* water cutting machine is adopted. Samples obtained from the water cut are shown in *Figure 47*. Slight delamination was experienced in demoulding the panel of N_2H_2 plasma treated fabrics so that it was possible to obtain just 4 specimens ready to be tested.

Figure 47: DCB and ENF CFRP samples : (left) untreated, (middle) N2 plasma treated, and (right) N2H2 plasma treated

The final thickness of these specimens were slightly lower than 3 mm but still enough for the tests that were necessary to carry out in order to find out the effectiveness of the surface treatment and resin – fibers adhesion.

2.1.4. DCB and ENF specimens testing

The components for DCB obtained from the plates via water cut met the geometric requirements described in ASTM D5528 for the DCB test. In particular, the following characteristics were recorded: 140 x 25 x 2.8 mm. In the bibliography, the dimensions reported for CFRP components to be tested at failure (mode I) both for resin-fiber adhesion and for bonding resistance between two CFRP components, are listed in *Table 6*.

Reference	Fabric type	Length [mm]	Width [mm]	Thickness [mm]
Murray et al. [15]	Unidirectional	125	25	4,2
Azadi et al. [50]	Unidirectional woven	125	25	5,3
Khudiakova et al. [51]	Unidirectional	145	20	3

Table 6: DCB specimens dimensions adopted in different researches

In order to perform the DCB test, it was used an MTS loading machine with a 500 load cell, installed on the mobile crossbar in order to indirectly obtain the mechanical deformation of the component under examination

At the same way, also the specimens cut away from the plates thanks to the water cut machine granted the geometric specifications in terms of samples dimensions, according to the *ASTM D7905*: 170 x 25 x 2.8 mm.

Dimensions that are similar to what were obtained by several authors for the same kind of test to be conducted: Y.Ma et al. [52] studied the toughening mechanism of PAN nanofiber film-modified CF/BMI composites by means of ENF test, using 160 x 25 x 3.5 mm specimens; T.K.O'Brien et al. [37] manufactured graphite epoxy composite zero-degree unidirectional test coupons made by twenty-four plies each, for static ENF and fatigue delamination tests, with nominal dimension of 180 x 25 x 4.5 mm (precisely 7 x 1 x 0.175 in).

To perform these tests, the same loading machine used for DCB test was used.

The precrack length changes between the two types of specimens: 50 mm for DCB sample and close to 65 mm for ENF sample, as shown in *Figure 48*.

Figure 48: ENF specimen lateral surface with insert

A speckle pattern had been applied on the lateral side of the DCB specimen to facilitate recognition of the deformation and displacement field while the test is running. The correlation value, as described in *Chapter 1.7.1.* , takes advantage of the variation of the speckle within the recorded deformations.

Before testing the specimens for both methodologies, the calibration and setup procedure described in *Chapter 1.7* is performed. The specimens are fixed to the loading blocks by means of a epoxy adhesive *Hy 4090 Loctite* and then they are bound to the crossbars (the upper mobile and the lower fixed) of the machine for the mechanical test.

MachVis Lens Configurator software offers the best set up in terms of choice of cameras for image acquisition. To obtain this information about the set up, it is necessary to indicate the length (or the diameter for analysis of cylindrical components) of the calibrated section and the

Free Working Distance camera - specimen for a correct focus. In the case of the DCB specimen, two chambers *Rodagon D* - 135mm and *Rodagon S* - 135mm (2056 x 1088 px) were adopted, placed on a fixed crosspiece, at a distance of 65 cm from the crosspieces of the machine, and an extension tube of 110 mm in conjunction with a *Smart Focus*. In addition, LED lights are fixed to the sides of the chambers for the correct illumination of the specimens.

Figure 49: DCB test – DIC setup

Two calibration target chosen for the calibration phase were of two types: 12x9 – 3mm and 12x9 – 2mm .

42 images were acquired using *Vic-Snap* software and after manual purging of out-of-scale data, a final score of 0.043 was reached, far enough from the limit considered acceptable for a correct calibration. Focal length in x direction and y direction for both cameras were close to 50000 pixel, adequate to a correct focus considering the specimen and its applied speckle dimensions but extremely sensitive to the accidental movements that the cameras could undergo.

All the VIC 3D parameters are listed in the following table.

Camera 1 Focal Length	50008.5 (y) 5008.5 (x)	pixel
Camera 2 Focal Length	49011.8 (y) 4909.4 (x)	pixel
Calibration Score	0.043	[-]
Subset Size	29	[-]
Subset Step	7	[-]
Sigma Threshold	0.02	[-]

Table 7: DIC VIC 3D setup calibration

Once the calibration is ended, the test has been initiated with a crosshead speed of 5 mm/min and acquisition frequency of images of 1 Hz.

ENF test was driven using an *Zwick-Roell Z005* test machine with 5 kN load cell. Loading and unloading phases were set on *TestXpertII* program with double ramps program. The unloading part input was evaluated based on the valued maximum load that can be reached during the calibration phases while the fracture phases was run until the reaching of the first load drop – crack propagation. Unloading and loading phases speed were set up to 0.5 mm/min according to the standard *ASTM D7905*.

Speckle pattern is not applied onto the surface specimen: simple white pattern is instead spread on it to facilitate the recognition of the crack while propagates during the test and to make the NPC and PC marks visible for the Compliance Calibration test. For this purpose, a *Nikon* was positioned in front of the specimen in order to record the NPC fracture test.

The position of the crack tip is difficult to asses because of the nature of the test: ENF specimen' arms are subjected to flexural stress and the fracture surfaces are close one to each other, opposite to what it is experienced in DCB test. The two fracture surfaces that are loaded in compression state, are forced to slide one on the other dissipating energy caused by friction. According to this issue, the crack tip could be unpaired between the extreme point on the upper arm and the same on the lower arm.

Figure 50: Zwick test machine for ENF test

2.2. Digital Image Correlation analysis

From 500 to 600 images for each test were acquired using *Vic-Snap* to limit the computational cost of the post process analysis that is related to the size of the number of images. The system was equipped with data acquisition hardware and two output channels, one for the load signal and the other one for the crossbar displacement. The Analog Data window appeared showing the voltage for each channel present in the device and to verify if the output is matched with the one of the machine. All this data was saved in a *CSV* log file associated with the project to post process load – displacement results.

Once the images were acquired, VIC-3D was running to run the correlation process. This methodology was carried out for the DCB tests since the surface remains almost flat for the entire duration of the test, not being subjected to shear stresses or high bending stresses as in the ENF test.

Both calibration images and speckle images had to be imported in the project with a proper calibration parameter setup: a region of interest was traced on the area subjected to deformation, divided into subsets of a defined dimension that is strictly influenced by the speckle pattern applied. An initial guess point was inserted in a region far away from the area under high deformation, assisting the first correlation made by the software.

Having defined these steps, the incremental correlation was run showing a plot of surface geometry (X, Y and Z coordinates for each analyzed point) as well as the displacement for each point U, V and W. 2D contour plot was checked while the analysis was running.

The projection error was checked assessing that it was maintained below the unity as a confirmation of the reliability of the calibration set up and the quality of the processed images. This kind of good result was obtained for one test in particular, named *NT_1* that is the specimen obtained from untreated carbon fiber fabrics as composite reinforcement. Alternately, if the error is high and the plot shows erroneous data in one region, there may be a problem with the analysis in that specific region.

The strain calculation was driven by means of a virtual extensometer positioned across the arms of the specimen, beyond the crack tip, evaluating their aperture while the crack propagates.

Engineering strain as $\frac{\Delta L}{L0}$ was computed and an example of the plot and of the contour *εyy* strain plot related to one of the processed image are shown in the *Figure 51*.

For the incremental correlation analysis, this latter was used to asses the crack tip position being *εyy* maximum at this location, by means of a *Matlab* code.

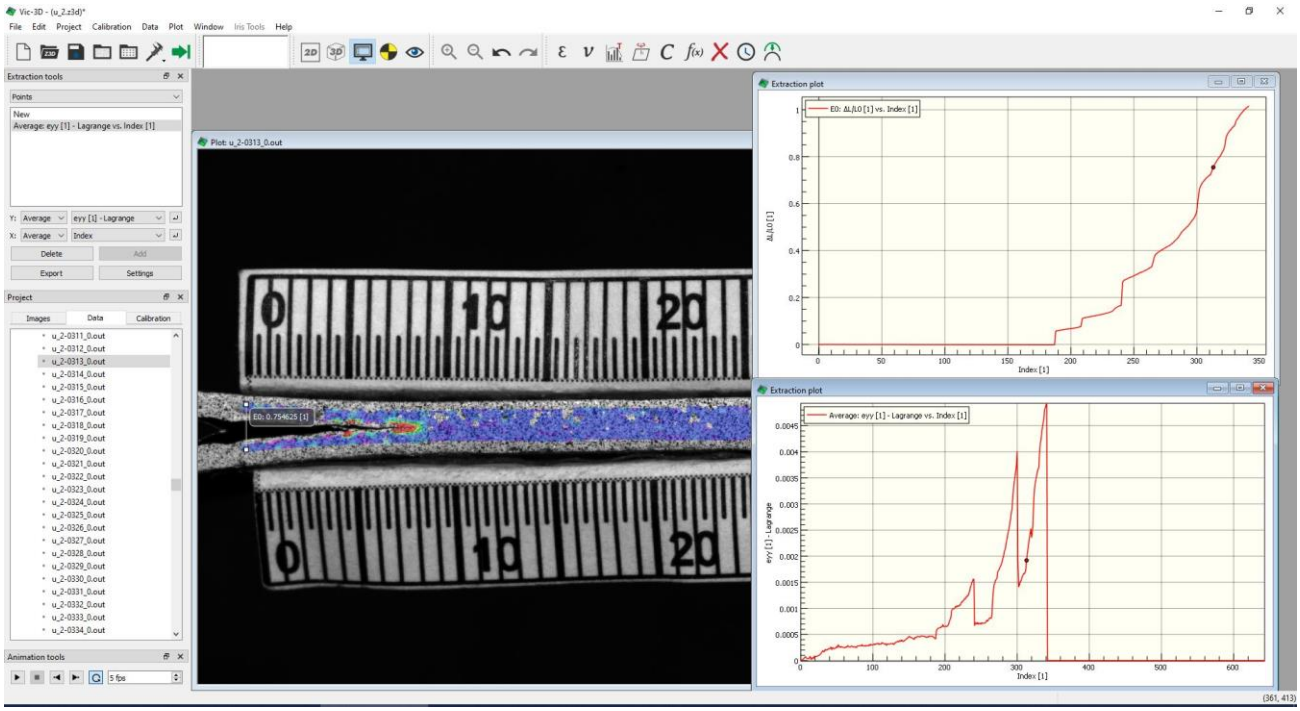

Figure 51: εyy contour plot, εyy cartesian diagram (bottom right) and extensometer E0 diagram (top right)

The code searches the X, Y coordinates of the subset center where the deformation is maximum excluding the *n* false positive that are behind the *n-1* new crack tip position. For this purpose, a proper selector delimits the area in the vicinity of the specimen mid plane and consequently allows to save the position coordinates in a vector. Lastly, the output were compared to the ones taken visually by means of the acquired images.

Untreated specimen N_{T1} was used as testing specimen to asses the reliability of the correlation. The percentage difference between the measurement of the crack length detected manually and automatically through the *Matlab* code is shown in *Figure 52*: the results obtained fall within the threshold of 5% of variability therefore it is considered acceptable. The ROI and the position of the crack tips from start to end of propagation are also shown below.

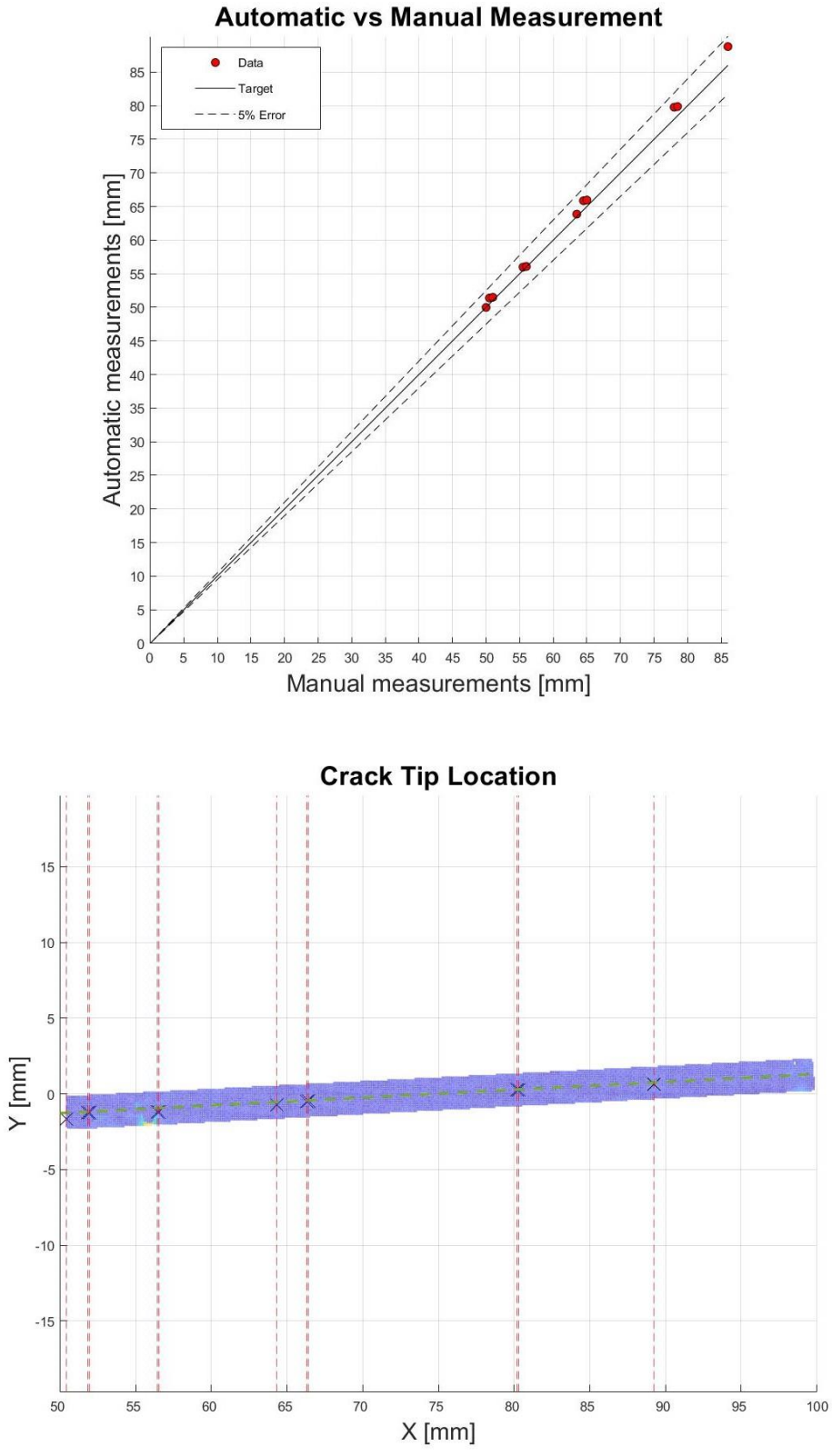

Figure 52: Automatic vs manual crack tip measurement (top) and crack tip location in ROI (bottom)

3. Result and Discussion

In this last chapter, DCB and ENF test results are presented.

DCB load plots are shown to have a first check about the mechanical behaviour related to the surface treatment effect and the stability of the crack at first propagation and subsequent ones. Consequently, the visual observation of the crack propagation is used to compute the final fracture toughness values, checking the images acquired by the DIC cameras.

ENF load plots for the CC NPC and PC as well as fracture NPC and PC tests are discussed. Lastly fracture toughness at first and second crack propagation are shown to asses the effectiveness of tests.

3.1. DCB results

The correlation analysis quality by DIC was sufficient for one of the specimens of the NT batch and for the N_2 specimens, a result closely related to the lower instability of the crack propagation. All the tests experienced a crack progression in the interlaminar region along the pre-crack line and the midplane of the specimens.

The load – displacement graphs of the three batches of NT, N_2 and N_2H_2 specimens are shown below. The details relating to the repeatability of the tests for each type of specimen, the average values and the percentage deviation from the mean are then listed in proper tables.

The acquisition frequency of the first untreated specimen was higher than in the subsequent ones, having obtained doubled amount of data. It was decided to reduce it by offering advantages from the point of view of computational time.

As it is possible to see from the aforementioned graphs, the delamination was not continuous but unstable and with more or less high degrees of instability depending on the type of specimen: the NT_1 presented a first phase of lower propagation instability as recorded for the totality of the test of the specimens N_2. The sample accumulated energy until the fracture started and the load registered an instant reduction. The crack subsequently suffered a temporary stop with a consequent resumption and increase of the load while the material starts again with the energy accumulation phase, up to the consecutive critical situation. The characteristics of this phenomenon correspond to those typical of *stick-slip*. [12]

A peculiarity of the event which was found during the test is the formation of secondary cracks. These types of composite materials reinforced with carbon fabrics have a complex fracture behaviour that can manifest itself with a non-unique crack front, as found for the NT_2 specimen shown in *Figure 54*. The crack appears branched close to the external areas of the specimen, due to the weft bundles while inside the specimen the warp bundles contain this phenomenon.

Having obtained this trend of the load, the new crack position was not recorded at a defined increase suggested by the standard, but increments of 0.5-1 mm were recorded for the low instability phase and subsequently at each peak of the experimental curve. The first sections show a constant slope for which the hypothesis of linear elastic behaviour for the chosen material is confirmed valid.

Both maximum peak load and load at first crack propagation were higher for N_2H_2 samples with respect to the N_2 and NT ones. Nevertheless, N_2 showed the lowest instability while crack progressed.

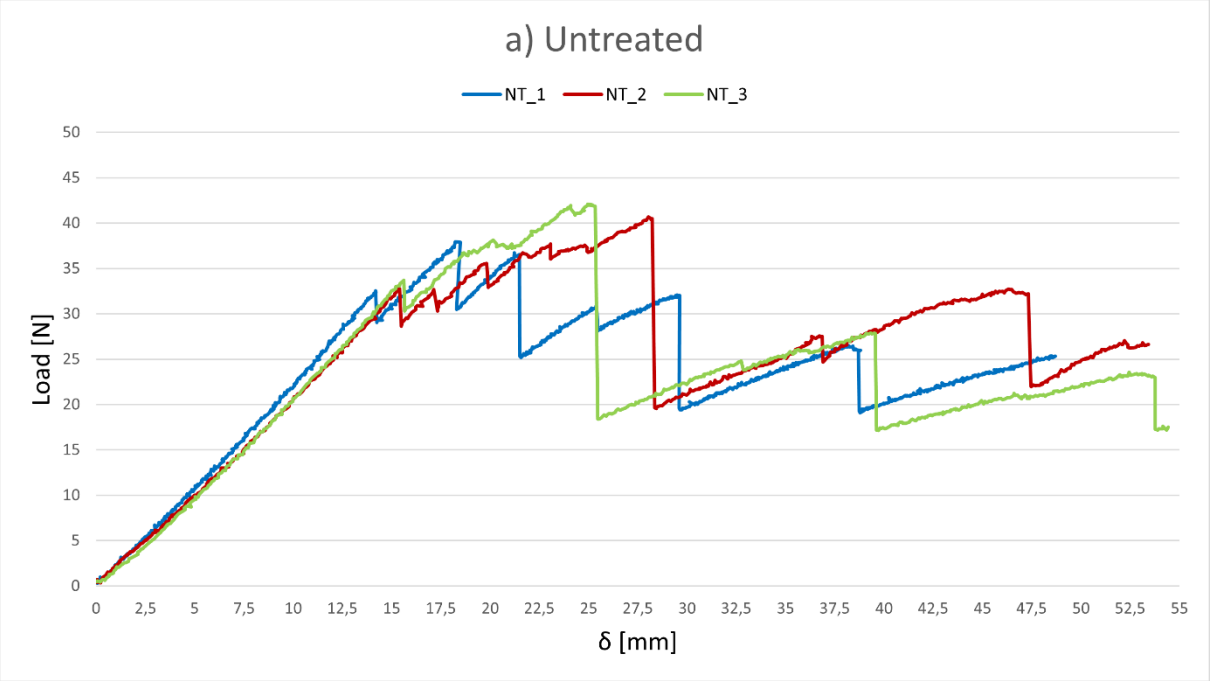

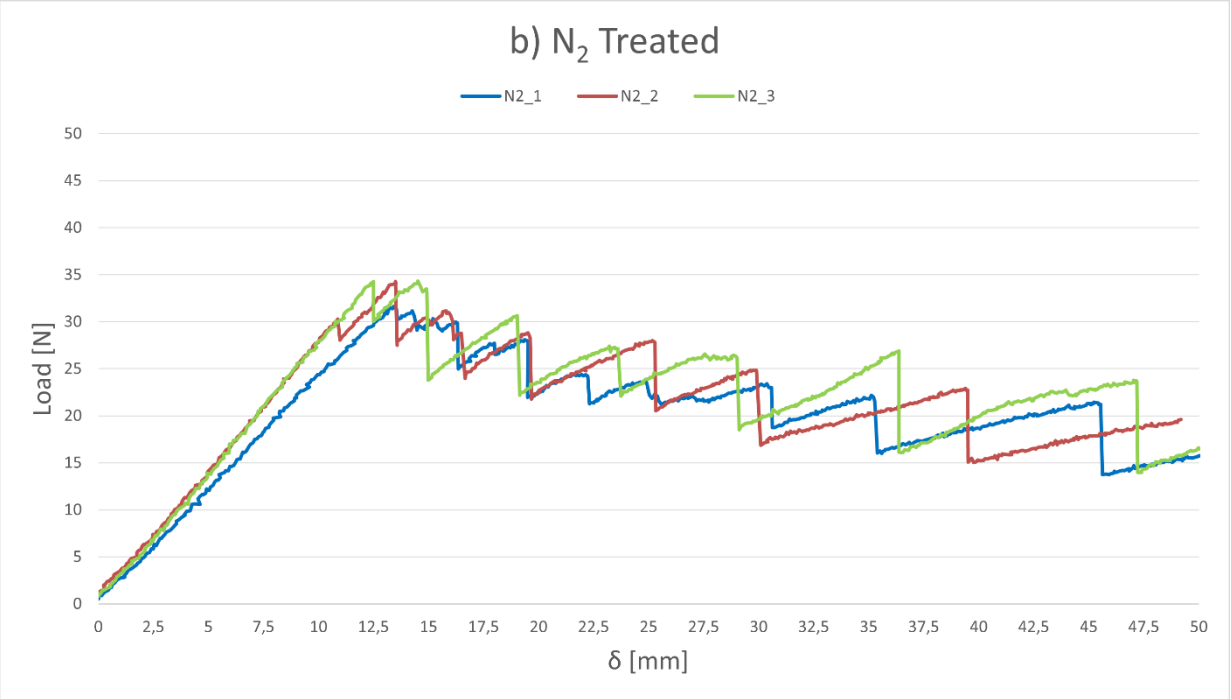

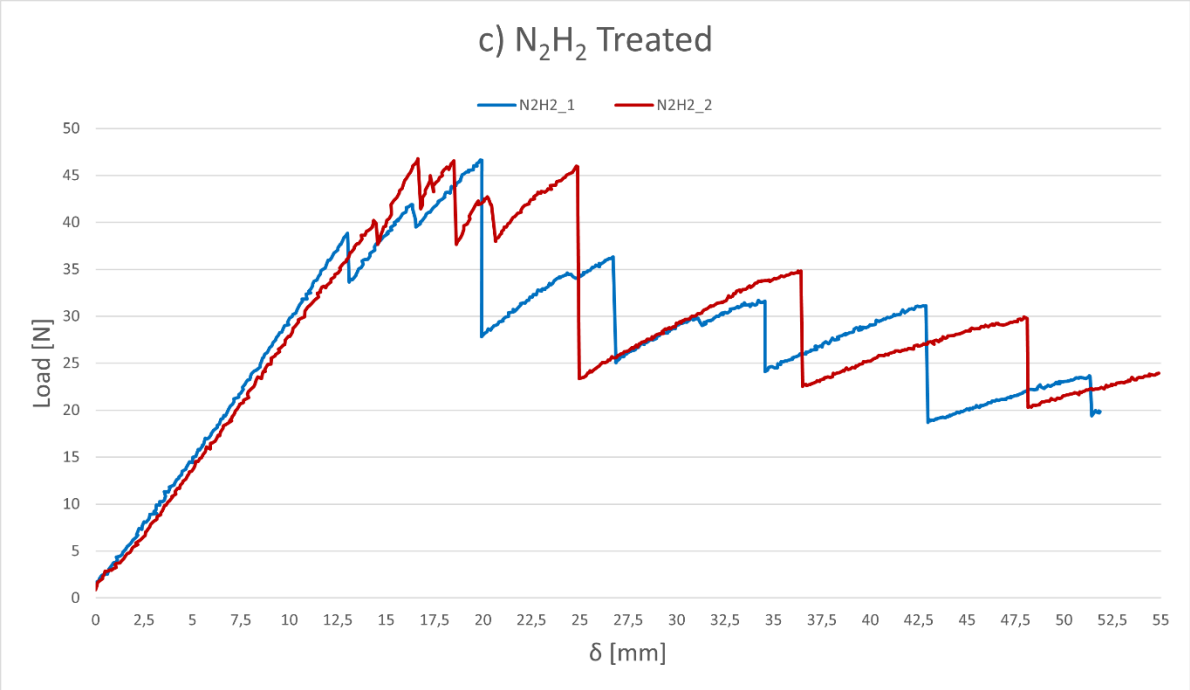

Figure 53: Plot Load vs δ for (a) untreated, (b) N_2 treated and (c) N_2H_2 treated samples

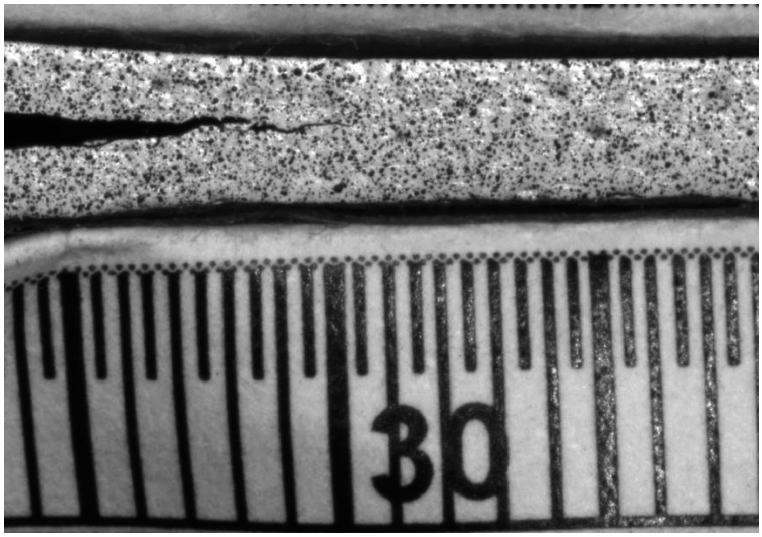

Figure 54: Formation of secondary crack near the main crack tip

Load – displacement data were used to define the CC parameters: *C* compliance, *F* and *N* correction factors, *m* angular coefficient of linear least squares regression line of the log of normalized specimen compliance *log(C/N)* versus *log(a)*. The values obtained for NT_1 are listed in *Table 8*.

a [mm]	P [N]	δ [mm]	C [mm/N]	log (C/N)	log a	F	N
50	30,3	11,5	0,38	-0,37	1,70	0,88	0,88
55	34,3	14,1	0,41	-0,33	1,74	0,87	0,89
56,5	30,3	16,0	0,53	-0,22	1,75	0,86	0,88
57,5	30,1	16,7	0,56	-0,20	1,76	0,86	0,88
63,5	24,0	17,3	0,72	-0,10	1,80	0,88	0,90
69	28,3	20,2	0,71	-0,10	1,84	0,87	0,90
78	27,8	26,0	0,93	0,02	1,90	0,87	0,90
88	24,9	30,5	1,23	0,14	1,94	0,87	0,90
103	22,7	40,1	1,77	0,30	2,01	0,87	0,90

Table 8: Computed parameters from from DCB test results on NT_1

The aforementioned results were used to derive the energy release rate and the critical value in mode I, G_{IC}. The crack propagation resistance curves, R curves, were obtained as a function of

the corresponding crack lengths, an example of which is shown in *Figure 55*. In particular, first sample of each batch of specimens results are plotted.

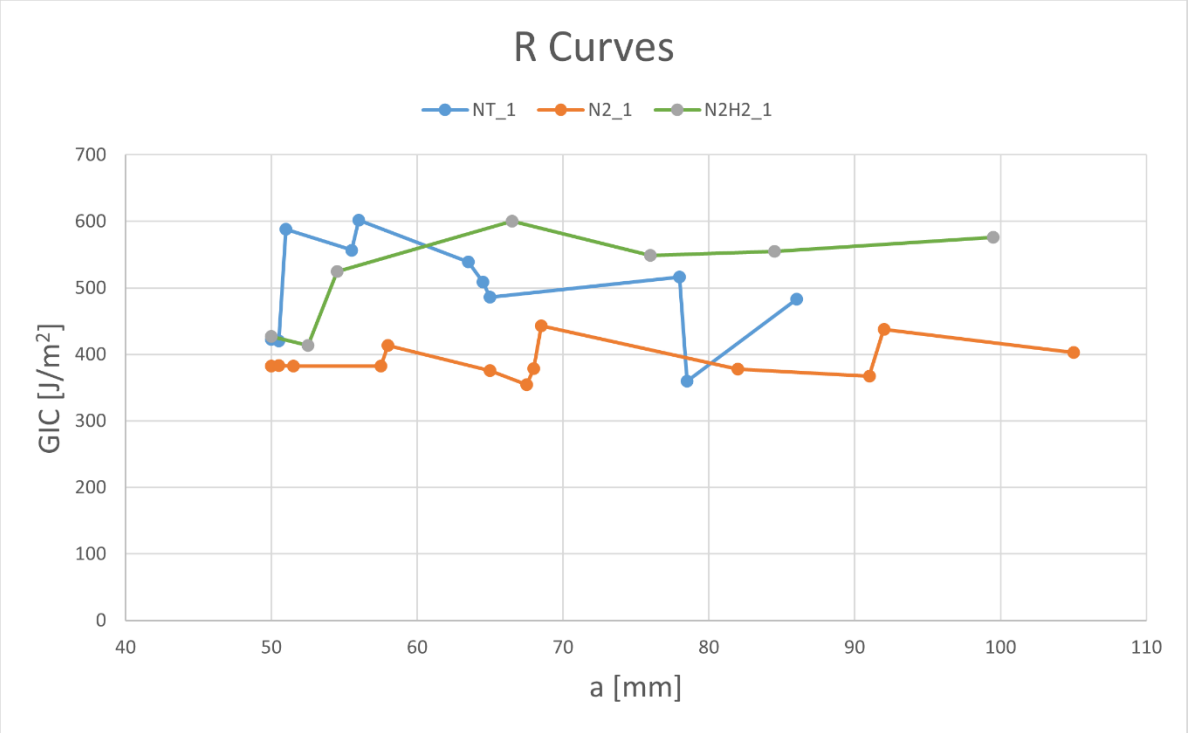

Figure 55: R curve for NT_1, N_2_1 and N_2H_2_1 samples

As expected and specified in standard ASTM D5528 [35], fracture toughness trend followed the Load – δ displacement one assuming an irregular and unstable shape, especially for NT and N_2H_2 while N_2 sample figured more stable. The first point plotted is the one related to the first propagation fracture toughness.

The same procedure for the other samples were adopted and the main results such as average values of P_{max} and G_{IC} as well as their standard deviation and CV% are presented in *Table 9*.

Average	P_{max} [N]	G_{IC} a_0 [J/m²]	G_{IC} a_i (STD) [J/m²]	CV%
NT	40,1	430,1	546,0 (41,6)	7,6
N_2	33,3	355,6	379,7 (42,9)	11,3
N_2H_2	45,8	444,1	539,7 (26,6)	4,9

Table 9: Principal parameter average values as output of DCB test

The deviation of each G_{IC} values computed at first propagation and subsequent lengths a_i compared to the average value was contained with fluctuations isolated from the range of variation. These can be attributed to the cutting of the specimens from a different area of the

manufactured plates with a different volumetric ratio value between fiber and matrix compared to the others. Nevertheless, CV% were quite acceptable even if for this kind of composite material, values that differ considerably from the average value are not uncommon.

The results obtained show that the N_2H_2 sample batches compared to the untreated ones, offered better or at least encouraging results since it recorded an increase of 14.3% in the maximum peak force as well as an increase of 3.3% of the first propagation G_{IC} value.

On the other hand, the N_2 specimens offered lower values both in terms of maximum load and energy release rate, although they returned a less unstable R curve trend and a less pronounced stick slip phenomenon.

3.2. ENF results

Loading and unloading phases were driven according to the methodology presented in *Chapter 2.1.4.*, at constant displacement rate of 0.5 mm/min.

The first part of the test allowed the calibration for subsequent NPC and PC fracture tests. The parameters adopted for the correct evaluation of the test were chosen on the basis of the specific indications of the ASTM standard, and based on the load and G_{IIC} values found in the bibliography for this type of component.

Load – δ displacement absolute value graphs obtained for the NPC calibration phase, useful for calculating compliance, and the Load - δ graph for the first fracture phase of NPC are presented below. The diagram C - a^3 is therefore shown having been useful for the evaluation of the parameters m and A of the curve $C = ma^3 + A$, necessary for the calculation of the fracture toughness of mode II.

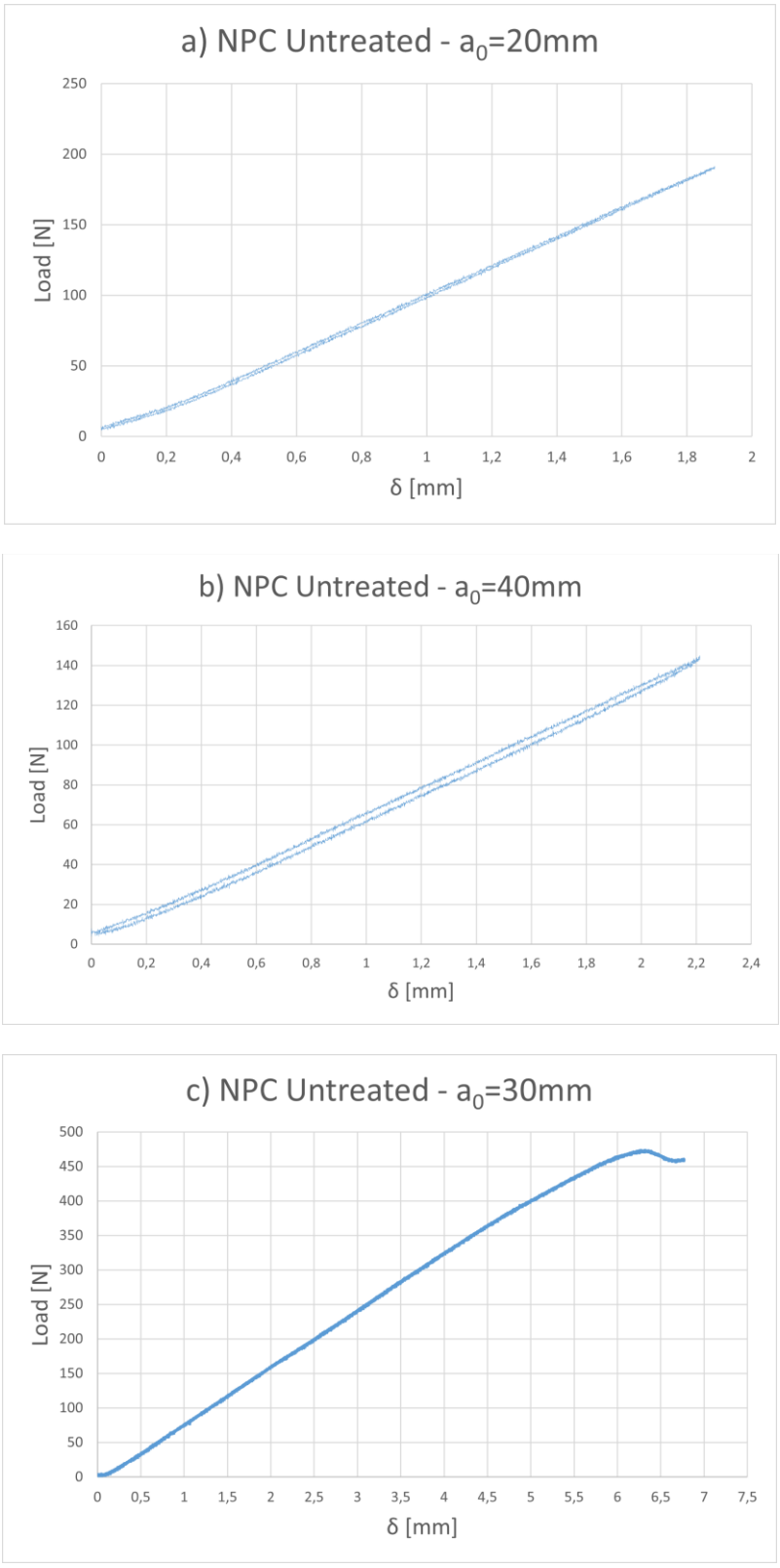

Figure 56: Load – δ diagrams for NPC tests on NT_1: (a) CC a_0=20mm, (b) CC a_0=40mm and (c) FT a_0=30mm tests

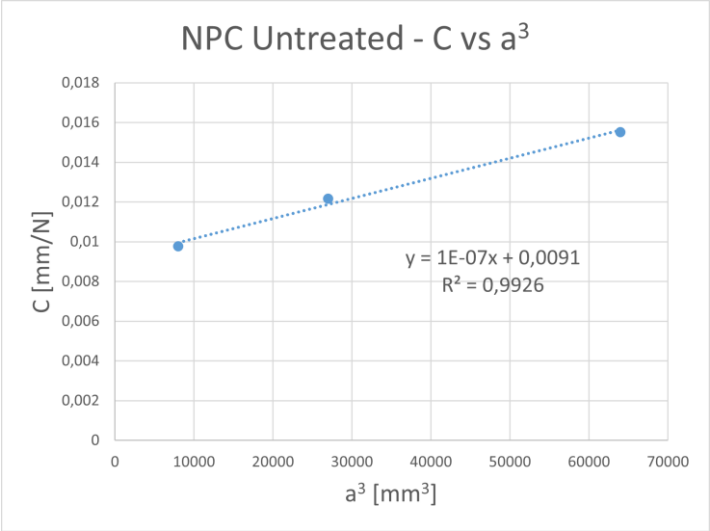

Figure 57: NPC C vs a^3 linear least squares linear regression analysis plot

As explained in the previous chapter, NPC tests at crack length of a_0=20 mm and a_0=40 mm experienced maximum loading condition equal to a reduced percentage of the maximum load at first crack propagation, and of the G_{IIC}. For example, as is possible to see in *Figure 56*, the max load experienced in NPC a_0=20 mm test was 190 N while in a_0=40 mm and a_0=30 mm it was respectively 145 N and 473,5 N. This first analysis was driven according to the fact that it was necessary to calibrate the test itself based on prediction of max load and G_Q, candidate toughness hence some deviation from the real P_{max} found out at the Fracture Test for NPC and PC was found discovered.

Thanks to the high resolution camera, it was possible to asses visually the crack tip position at first propagation hence a_{vis} was used to define the new positions for the last three steps of the test. To be consistent with this measurement, a_{calc} was calculated and double checked paying attention to asses $a_{vis} > a_{calc}$, as justified in the following table.

m	1,012E-07
A	9,0E-02
Cu	0,014
a_{calc} [mm]	36,9
a_{vis} [mm]	37

Table 10: Compliance calibration parameters and $a_{calc} - a_{vis}$ comparison for NPC NT_1

Once NPC part was ended, the same procedure was involved for PC part until both G_{IIC} for NPC and PC were computed. The two values are considerable acceptable once the candidate toughness G_Q of NPC and PC calibration parts falls inside the 15-35% range. As shown in the table below, all the computed values were acceptable hence any discard of G_{IIC} was not necessary.

Similarly, all the batches were tested and the average results for P_{max} at fracture test (a_0=30 mm both for NPC and PC) and G_{IIC} are listed in *Table 12*.

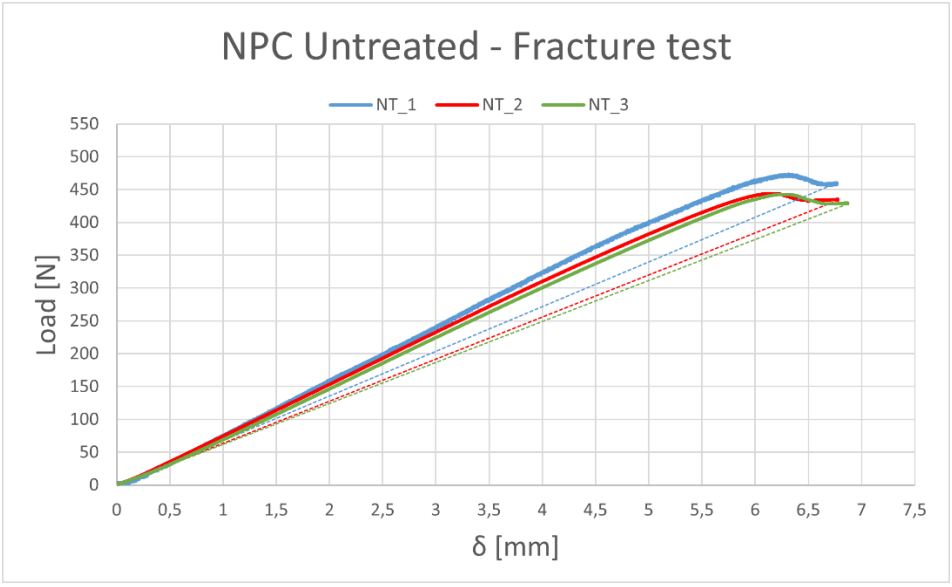

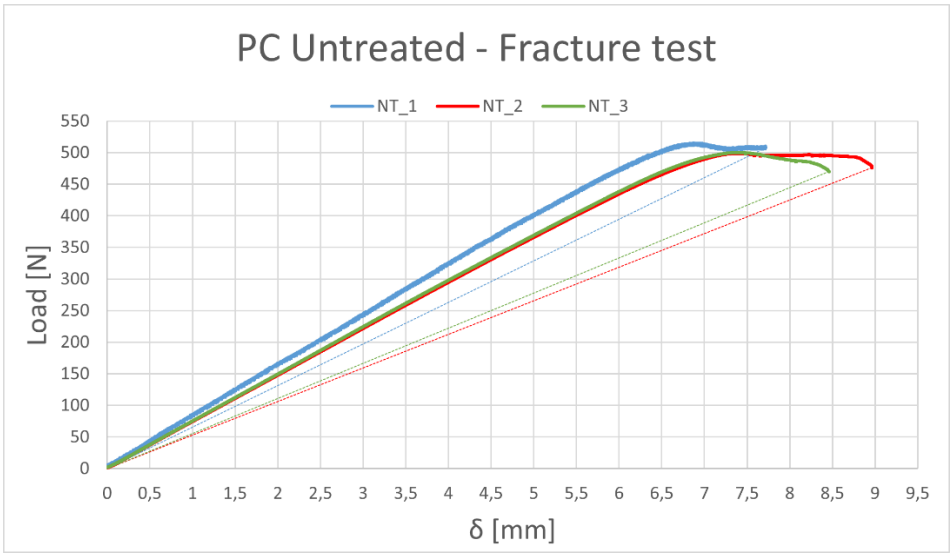

Figure 58: NPC and PC Fracture test (a_0 = 30 mm) Load – δ graphs for untreated specimens

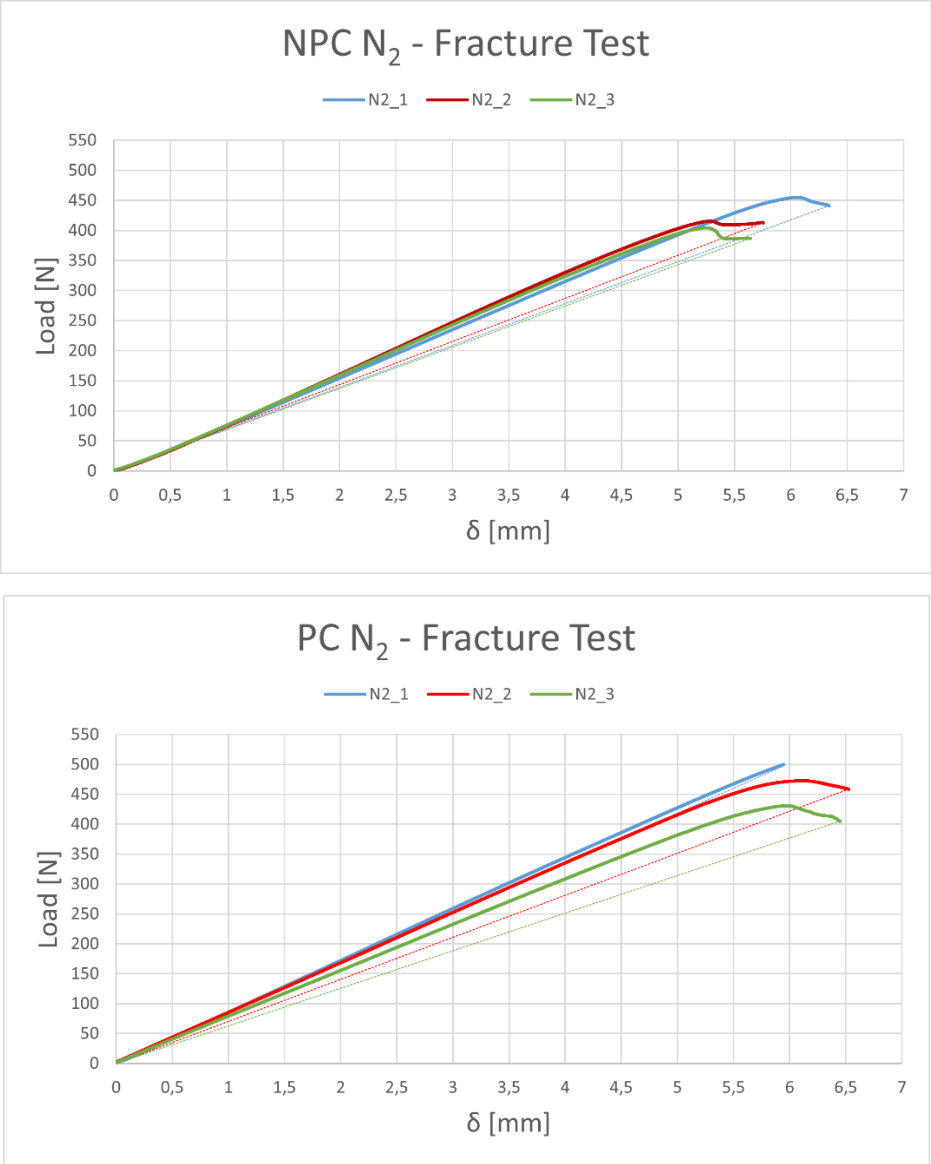

Figure 59: NPC and PC Fracture test (a_0 = 30 mm) Load – δ graphs for N_2 specimens

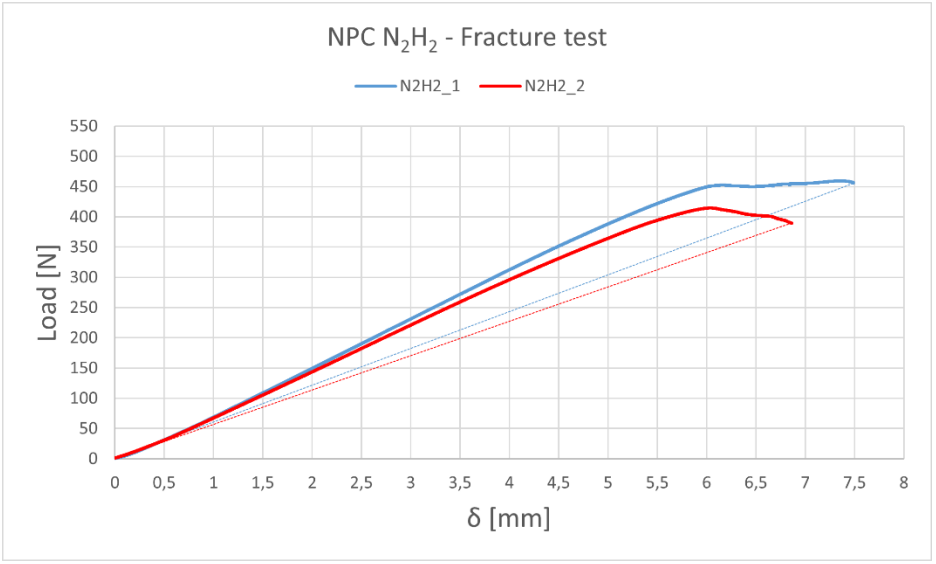

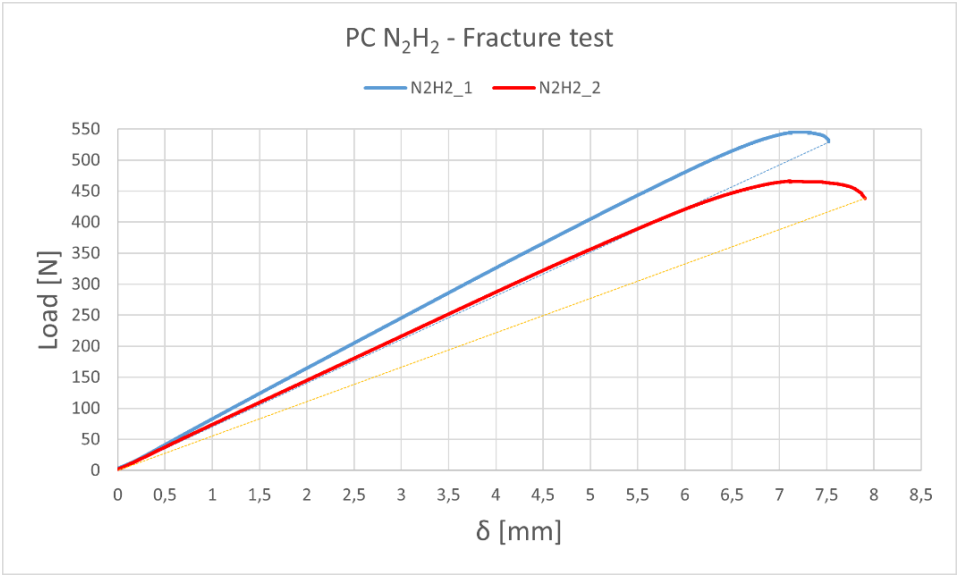

Figure 60: NPC and PC Fracture test (a_0 = 30 mm) Load – δ graphs for N_2H_2 specimens

	G_Q [J/m²]	G_{IIC} [J/m²]	%G_Q
NPC a_0=20 mm	199,0	-	15,5%
NPC a_0=40 mm	204,0	-	27,2%
NPC a_0=30 mm	-	**1224,7**	-
PC a_0=20 mm	229,0	-	16,0%
PC a_0=40 mm	230,5	-	16,1%
PC a_0=30 mm	-	**1432,3**	-

Table 11: G_Q and G_{IIC} for NT_1

Sample	Test	P_{max} [N]	G_{IIC} a_0 (STD) [J/m²]	CV%
NT	NPC	453,5	1154,2 (63,4)	5,5
	PC	504,5	1420,5 (36,0)	2,5
N_2	NPC	425,0	988,4 (95,5)	9,6
	PC	467,8	1309,7 (75,3)	5,7
N_2H_2	NPC	437,1	1192,2 (133,3)	11,2
	PC	505,8	1649,4 (133,6)	8,0

Table 12: P_{max}, fracture toughness in mode II and STD – CV% results for the tested specimens

The NT and N_2 specimens gave good results in terms of repeatability as opposed to those treated with N_2H_2. Nevertheless, the results in terms of energy release rate of the latter were more than satisfactory, better than both the NT and the N_2.

In particular, the N_2H_2 specimens compared with the NT ones, returned an increase of 3.3% and 16.1% for the NPC G_{IIC} and NPC PC respectively, even if the two samples returned slightly differences.

On the contrary, the N_2 specimens did not offer improvements compared to the NT specimens, confirming the results obtained for the mode I delamination test by DCB test. The decrease in G_{IIC} values compared to NT was 14.3% for NPC G_{IIC} and 7.8% for PC G_{IIC}.

Conclusions

The purpose of this thesis is to present the use of the innovative plasma surface treatment technology through the use of APPJ atmospheric plasma, for the treatment of carbon fiber fabrics intended for the plastic components manufacturing for industrial use.

This technology has been committed to obtaining improvements in terms of increasing the adhesion between fibers and matrix having used an epoxy-based resin as matrix. Following an in-depth bibliographic search, it became clear that it was necessary to adopt to adopt specific process parameters (choice of gas, gas flow rate values and plasma exposure times of the fabric) aimed at increasing functional groups on the fabric's surface. In particular hydroxyl, carboxylic and amino-based groups are capable of change the non-polar chemical nature of carbon. The choice fell on the use of nitrogen and hydrogen mixture as the process gas.

In the first part of the thesis, the chemical-physical peculiarities of carbon and technologies for surface treatment were highlighted with a focus on plasma treatments and surface characterization methods to attest an initial evidence of the experiment conducted.

The mechanics of the fracture and the delamination behavior of this type of components was subsequently discussed.

At the end of the introductory part, the Digital Image Correlation (*DIC*) technique was presented, which lent itself well to the automatic search for the position of the crack during its propagation through *Matlab* processing of the correlation analysis outputs. This is innovative compared to the manual measurement technique.

The second part of the thesis focuses on the testing phase starting from the plasma treatments on the fabrics conducted in the company *Environment Park S.P.A*. at the *Plasma Nano-Tech* laboratory, and the manufacture of the final components by vacuum infusion.

The results of the Attenuated Total Reflection (*ATR*) spectroscopy and Micro-Raman spectroscopy surface characterizations carried out at the l'Università del Piemonte Orientale (Alessandria) are shown highlighting the possible chemical-physical improvements made and to be verified by mechanical delamination tests of mode I and mode II.

In support of the thesis, it was necessary to adopt the ASTM D5528 and ASTM D7905 standards to verify the improvement of the aforementioned treatment.

For this reason, the setup and equipment chosen for the Double Cantilever Beam (*DCB*) and End Notched Flexure (*ENF*) delamination tests of mode I and mode II with attached DIC instrumentation are shown. This chapter ended with the first results about the feasibility and functioning of the *Matlab* code used to search for the crack tip while testing is in progress.

The last part of the thesis focuses on the results of mechanical tests. In particular, graphs and tables summarizing the main parameters and results necessary for their understanding and critical evaluation are shown. Tests on specimens obtained from fabrics treated with nitrogen gas offered not encouraging outputs regarding the increase in maximum force achieved at first crack propagation for both the mode I and mode II delamination tests although less process instability was obtained. The cause of the lack of improvement following this treatment is attributable to the non perfect calibration of the plasma treatment process, which is limited to an ablative action of the fabric surface without effectively affecting its chemical structure.

On the other hand, the N_2H_2 specimens showed increases in G_{IC} and G_{IIC} of 3.3% compared to the untreated specimens and increases in P_{max} at first crack propagation of 14.3% and 16.1% for DCB and ENF respectively.

Possible improvements can be achieved by further modifying the process parameters of the surface treatment especially for what concern the N_2 plasma treatment: having observed that the chosen process parameters did not lead to the desired enhancements, it is considered necessary for future studies, the analysis of the exploration curves obtainable by varying certain primary or secondary parameters and setting others as fixed, so as to manage the window of acceptability and eliminate parameters outside the exploratory limit range. Considering this, the results obtained here will then be used as new starting points in the exploratory phase.

References

[1] – Roger B (1960), "Filamentary graphite and method for producing the same", *Google Patents US Patent* No 2,957,756

[2] – P.Morgan, "Carbon fibers and their composites", *Taylor & Francis Group*, 1st Edition, 2005

[3] – M.Sharma, S.Gao, E. Mäder, H.Sharma, L.Yew Wei, J.Bijwe, "Carbon fiber surfaces and composite interphases", *Composites Science and Technology*, 102:35-50, 2014

[4] – S.Tiwari, J.Bijwe, "Surface treatment of carbon fibers – A review", *Procedia Technology*, 14:505-512, 2014

[5] – Z.Wu, C.Pittman, S.Gardner, "Nitric acid oxidation of carbon fibers and the effects of subsequent treatment in refluxing aqueous NaOH", *Carbon*, 33(5):597-605, 1995

[6] – B.Barbier, J.Pinson, G.Desarmot, M.Sanchez, "Electrochemical bonding of amines to carbon fiber surfaces toward improved carbon-epoxy composites", *Journal of The Electrochemical Society*, 137(6), 1990

[7] – S.Ebnesajjad, A.H.Landrock, "Chapter 3 – Material surface preparation techniques", *Adhesive Technology Handbook (Third Edition)*, 35-66, 2015

[8] – M.K.Almutairi, R.A.Felemban, S.E.Pasha, N.T.Abo khashaba et al., "The effect of different surface treatment of carbon fibers and their impact on composites", *The Egyptian Journal of Hospital Medicine*, 70(8):1275-1281, 2018

[9] – S.Tiwari, M.Sharma, S.Panier, J.Bijwe, "Influence of cold remote nitrogen oxygen plasma treatment on carbon fabric and its composites with specialty polymers", *Journal of Materials Science*, 46(4):964-974, 2011

[10] – T.Ceregatti, L.Kunicki, S.R.Biaggio, L.C.Fontana, C.Dalmolin, "N2–H2 plasma functionalization of carbon fiber fabric for polyaniline grafting", *Plasma Process Polym.*, 2020, e1900166

[11] – X.L.Deng, A.Yu.Nikiforov, P.Vanraes, Ch.Leys, "Direct current plasma jet at atmospheric pressure operating in nitrogen and air", *Journal of Applied Physics*, 113, 023305, 2013

[12] – S.Sridharan, "Delamination behaviour of composites", *Woodhead Publishing Limited*, 2005

[13] – A.J.Smiley, R.B.Pipes, "Rate Effects on Mode I Interlaminar Fracture Toughness in Composite Materials", *Journal of Composite Materials*, 21(7):670-687, 1987

[14] – H.Zabala, L.Aretxabaleta, G.Castillo, J.Aurrekoetxea, "Loading rate dependency on mode I interlaminar fracture toughness of unidirectional and woven carbon fibre epoxy composites", *Composite Structures*, 121:75-82, 2015

[15] – B.Murray, S.Fonteyn, D.Carrella-Payan, L.Pyl et al., "Crack Tip Monitoring of Mode I and Mode II Delamination in CF/Epoxies under Static and Dynamic Loading Conditions Using Digital Image Correlation", *The 18th International Conference on Experimental Mechanics*, 2018

[16] – I.Sarikaya, M.M.Tahiyat, R.F.Harik, T.I.Farouk, J.M.Connell, P.Gilday, "Plasma Surface Functionalization of AFP Manufactured Composites for Improved Adhesive Bond Performance", *SAMPE 2019* - Charlotte, NC., 2019

[17] – T.K.Das, P.Ghosh, N.Ch Das, "Preparation, development, outcomes, and application versatility of carbon fiber-based polymer composites: a review", *Advanced Composites and Hybrid Materials*, 2:214-233, 2019

[18] – G.Belingardi, Slides of the Design of Lightweight and Composite Structures, *Polytechnic of Turin*, A.A. 2020-2021

[19] – R.F.Gibson, "Principles of composite material mechanics", *CRC Press – Taylor & Francis Group*, IVth Edition, 2016

[20] – C.Soutis, "Fibre reinforced composites in aircraft construction", *Progress in Aerospace Sciences*, 41(2):143-151, 2005

[21] – A.Buhu, L.Buhu, "Chapter 2 Woven Fabrics for Technical and Industrial Products", *IntechOpen*, 2018

[22] – Z.Xu, Li Chen, Y. Huang, J.Li, X.Wu, X.Li, Y.Jiao, "Wettability of carbon fibers modified by acrylic acid and interface properties of carbon fiber/epoxy", *Science Direct – European Polymer Journal*, 44:494-503, 2007

[23] – KB. Hung, J.Li, Q. Fan, ZH. Chen, "The enhancement of carbon fiber modified with electropolymer coating to the mechanical properties of epoxy resin composites", *Composites Part A: Applied Science and Manufacturing*, 39(7):1133-1140, 2008

[24] – X.Lu, S.Reuter, M.Laroussi, D.Liu, "Nonequilibrium Atmospheric Pressure Plasma Jets, Foundamentals, Diagnostics and Medical Applications", *Routledge – Taylor & Francis Group*, 1st Edition, 2019

[25] – P.Sundriyal, M.Pandey, S.Bhattacharya, "Plasma-assisted surface alteration of industrial polymers for improved adhesive bonding", *International Journal of Adhesion and Adhesives*, 101, 102626, 2020

[26] – C. Dalla Pria, "Ottimizzazione del trattamento su materiali industriali tramite jet al plasma freddo a pressione atmosferica" [tesi di laurea magistrale], *Padova: Università degli Studi di Padova*, 2019

[27] – X. L. Deng, A. Yu. Nikiforov, P. Vanraes, Ch. Leys, "Direct current plasma jet at atmospheric pressure operating in nitrogen and air", *J. Appl. Phys*., 113, 023305, 2013

[28] – n.p., https://www.plasmatreat.co.uk/plasma-treatment/plasma-pretreatment.html

[29] – S.Wang, J.Min, J.Lin, C.Sun, S.Yang, "Effect of atmospheric pressure plasma treatment on the lap-shear strength of adhesive-bonded sheet molding compound joints", *Automotive Innovation*, 1:237-246, 2018

[30] – L.Kim, R.Mauchauffé, D.Kim, J.Kim, SY.Moon, "Mechanism study of atmospheric-pressure plasma treatment of carbon fiber reinforced polymers for adhesion improvement", *Surface & Coating Technology*, 393, 125841, 2020

[31] – LB.Nohara, GP.Filho, EL.Nohara, MU.Kleinke, MC.Rezende, "Evaluation of carbon fiber surface treated by chemical and cold plasma processes", *Material Research*, 8(3):281-286, 2005

[32] – S.Ebnesajjad, C.Ebnesajjad, “Surface Treatment of Materials for Adhesive Bonding”, *Elsevier*, 2nd Edition, 2013

[33] – S.Sridharan, “Delamination behaviour of composites”, *Woodhead Publishing Limited*, 2008

[34] – D.Gross, T.Seelig, “Fracture mechanics”, *Mechanical engineering series*, Springer, 01, 2006

[35] – ASTM D5528/D5528M – 21, “Standard test method for mode I interlaminar fracture toughness of unidirectional fiber-reinforced polymer matrix composites”, *Standards, ASTM International, West Conshohocken, PA, USA,* 2021

[36] – ASTM D7905/D7905M – 19, “Standard test method for determination of the mode II interlaminar fracture toughness of unidirectional fiber-reinforced polymer matrix composites”, *Standards, ASTM International, West Conshohocken, PA, USA,* 2019

[37] – T.K.O’Brien, W.K.Johnston, G.J.Toland, “Mode II interlaminar fracture toughness and fatigue characterization of a graphite epoxy composite material”, *National Aeronautics and Space Administration*, 2010, TM-2010-216838

[38] – M.A.Sutton, J.J.Orteu, H.Schreier, “Image correlation for shape, motion and deformation measurements: basic concepts, theory and applications”, *Springer Science & Business Media,* 2009

[39] – n.p., https://www.correlatedsolutions.com/vic-2d/

[40] – J.Babler., http://www.ncorr.com/download/ncorrmanual_v1_2_2.pdf

[41] – n.p., https://www.gom.com/en/products/gom-suite/gom-correlate-pro

[42] – H.Schreier, J.R.Braasch, M.Sutton, “Systematic errors in digital image correlation caused by intensity interpolation”, *Optical Engineering,* 39: 2915-2921, 2000

[43] – B.Pan, K.Qian, H.Xie, A.Asundi, “Two-dimensional digital image correlation for in-plane displacement and strain measurement: a review”, *Measurement Science and Techonlogy*, 20, 062001, 2009

[44] – B.Pan, A.Asundi, H.Xie, J.Gao, “Digital Image Correlation using Iterative Least Squares and Pointwise Least Squares for Displacement Field and Strain Field Measurements”, *Optics and Lasers in Engineering*, 47(7), 2009

[45] – n.p., https://www.easycomposites.co.uk/200g-profinish-coated-22-twill-3k-carbon-fibre-cloth

[46] – n.p., https://www.horiba.com/esp/scientific/products/detail/action/show/Product/ultra-low-frequency-raman-module-1642/

[47] – I.V.Terekhov, E.M.Chistyakov, “Binders used for the manufacturing of composite materials by liquid composite molding”, *Polymers*, 14, 87, 2021

[48] – A.Croce, G.Re, C.Bisio, G.Gatti, S.Coluccia, L.Marchese, “On the correlation between Raman spectra and structural properties of activated carbons derived by hyper-crosslinked polymers”, *Research on Chemical Intermediates*, 47:419-431, 2021

[49] – D.Tuschel, “Stress, strain, and Raman spectroscopy”, *Spectroscopy*, 34(9):10-21, 2019

[50] – M.Azadi, M.Saeedi, M.Mokhtarishirazabad, P.Lopez-Crespo, “Effects of loading rate on crack growth behaviour in carbon fiber reinforced polymer composites using digital image correlation technique”, *Composites Part B*, 175, 107161, 2019

[51] – A.Khudiakova, V.Grasser, C.Blumenthal, M.Wolfhrt, G.Pinter, “Automated monitoring of the crack propagation in mode I testing of thermoplastic composites by means of digital image correlation”, *Polymer Testing*, 82, 106304, 2020

[52] – Y.Ma, Y.Zhuang, C.Li, C.Shen, X.Shen, “Interlaminar mechanical properties and toughnening mechanism of highly thermally stable composite modified by Polyacrylonitrile Nanofiber Films”, *Polymers*, 14, 1348, 2022

Acknowledgements

È doveroso dedicare questa pagina alle persone che mi hanno supportato in questo percorso, chi c'è stato fin dall'inizio e chi si è unito in corso d'opera.

Innanzitutto, ringrazio i miei relatori e supervisori Prof. Davide Salvatore Paolino e Ing. Raffaele Ciardiello per la fiducia, la pazienza e la professionalità che mi hanno mostrato fin dall'inizio. Grazie a voi ho avuto modo di formarmi e accrescere le mie conoscenze oltre ad avere conferma che con dedizione e interesse, nulla risulta irraggiungibile.

Un ringraziamento speciale va al mio Tutor Dott. Domenico D'Angelo per avermi fatto da mentore nel migliore modo possibile, sempre pronto ad incoraggiarmi nel mio primo contatto con il mondo del lavoro, trattandomi come suo pari.

Alla mia famiglia che con sacrificio mi è stata accanto anche quando non era materialmente possibile, assecondandomi nelle mie decisioni e confortandomi nei momenti di scoraggiamento.

Ai miei amici e mia seconda famiglia, che con i loro preziosi consigli e il loro amore incondizionato mi hanno sostenuto e accompagnato in questo lungo percorso accademico.

Ad Alessandro, amico e fratello, da sempre e per sempre.